Size-selective investigations of spectral and emission properties of small particles and nanotubes

Dissertation zur Erlangung des Grades
„Doktor der Naturwissenschaften“
am Fachbereich für Physik der Johannes Gutenberg-Universität in Mainz

Diplom-Physiker Andriy Hloskovskyy (Andrei Gloskovskii)
geb. in Lwow (Ukraine)

Mainz, Juni 2006

Part of this work has been published in:

Electrical and emission properties of current-carrying silver cluster films detected by an emission electron microscope
A. Gloskovskii, D. Valdaitsev, S.A. Nepijko, N.N. Sedov, G. Schönhense
Appl. Phys. A **79** (2004) 707–712

Electrical and emission properties of current-carrying silver nanocluster films investigated by emission electron microscopy
A. Gloskovskii, D.A. Valdaitsev, S.A. Nepijko, G. Schönhense
Microsc. Microanal. **9**, Suppl.3 (2003) 176–177

Time-of-Flight Photoelectron Spectromicroscopy of Single MoS_2 nanotubes
A. Gloskovskii, S. A. Nepijko, M. Cinchetti, G. Schönhense, G. H. Fecher, H. C. Kandpal, C. Felser, H. A. Therese, N. Zink, W. Tremel, A. Oelsner
J. Appl. Phys. (2006) accepted

Measurement of the electric field distribution and potentials on the object surface in an emission electron microscope without restriction of the electron beams
S.A. Nepijko, A.Gloskovskii, N.N. Sedov, G. Schönhense
Journal of Microscopy **211** (2003) 89–94

Lateral resolving power of a time-of-flight photoemission electron microscope
S.A. Nepijko, A. Oelsner, A. Krasyuk, A. Gloskovskii, N.N. Sedov, C.M. Schneider, G. Schönhense
Appl. Phys. A **78** (2004) 47–51

Emission electron microscopy of nanoparticles in strong fs laser fields
M. Cinchetti, A. Gloskovskii, D.A. Valdaitsev, A. Oelsner, G.H. Fecher, S.A. Nepijko, H.J. Elmers, G. Schönhense
Microsc. Microanal. **9**, Suppl.3 (2003) 168–169.

Photoemission time-of-flight spectromicroscopy of Ag nanoparticle films on Si(111)
M. Cinchetti, D.A. Valdaitsev, A. Gloskovskii, A. Oelsner, S.A. Nepijko, G. Schönhense
J. Electron. Spectr. Rel. Phenom. **137-140** (2004) 249–257

Articles in preparation:

Electron emission from nanoparticle Ag film excited by fs-laser radiation
A. Gloskovskii, D. A. Valdaitsev, S. A. Nepijko, J. Lange, M. Bauer, M. Aeschlimann, G. Schönhense
In preparation

TEM and X-ray absorption study of Vanadium oxide nanotubes
A.Gloskovskii, S.A. Nepijko, G. Schönhense, H.A. Therese, A.Reiber, H.C. Kandpal, G. H. Fecher, W. Tremel, M. Klimiankou
In preparation

Further related publications:

Element specific magnetic moments from core-absorption magnetic circular dichroism of the doped Heusler alloy $Co_2Cr_{0.6}Fe_{0.4}Al$
H.J. Elmers, G.H. Fecher, D. Valdaitsev, S.A. Nepijko, A. Gloskovskii, G. Jakob, G. Schönhense, S. Wurmehl, T. Block, C. Felser, P.-C. Hsu, W.-L. Tsai, S. Cramm
Phys. Rev. B **67** (2003) 104412 / 1–7

Investigation of a novel material for magnetoelectronics: $Co_2Cr_{0.6}Fe_{0.4}Al$

C. Felser, B. Heitkamp, F. Kronast, D. Schmitz, S. Cramm, H.A. Dürr, H.J. Elmers, G.H. Fecher, S. Wurmehl, T. Block, D. Valdaitsev, S.A. Nepijko, A.Gloskovskii, G. Jakob, G. Schönhense, W. Eberhardt

J. Phys.: Condens. Matter **15** (2003) 7019–7027

Photoemission Electron Microscopy as a tool for the investigation of optical near fields

M. Cinchetti, A. Gloskovskii, S.A. Nepijko, G. Schönhense, H. Rochholz, M. Kreiter

Phys. Rev. Lett. **95** (2005) 047601 / 1–4

Contents

Introduction **3**

Chapter 1. Theory **7**

1.1 Thermal equations 7

1.2 Mechanisms of electron emission from current-carrying thin metal cluster films 11

1.2.1 Field emission mechanism 12
1.2.2 Emission of hot electrons 13

1.3 Mechanisms of electron emission under femtosecond laser excitation 15

1.3.1 Multiphoton photoemission (*n*PPE) 16
1.3.2 Thermionic emission 20
1.3.3 Thermally-assisted *n*PPE 21
1.3.4 Optical field emission 24

1.4 Statistical approach to the light absorption by small metal particles 27

Chapter 2. Experimental details **32**

2.1 UHV components 32

2.2 General layout of the photoemission electron microscope (PEEM) 33

2.2.1 PEEM in time-of-flight mode 33
2.2.2 PEEM with imaging energy filter 35

2.3 Set-up for the observation of current-induced emission 37

2.4 Laser systems 37

Chapter 3. Results and discussion **40**

3.1. Electrical and emission properties of current-carrying silver cluster films 40

3.1.1 Sample preparation 40
3.1.2 Measurements of electron and photon emission versus applied voltage 41
3.1.3 Determination of the potential distribution in the film 44
3.1.4 Formation of the field contrast in an emission electron microscope 47
3.1.5 Investigation of the local electron emission 49
3.1.6 Investigation of electron emission at low voltages 52
3.1.7 Discussion and conclusions 56

3.2 Emission properties of metal cluster films under femtosecond laser excitation 58

3.2.1 Electron yield spectroscopy of Ag and Au nanoparticle films excited by ultrashort fs-laser pulses....58
3.2.1.1 Sample preparation and characterization....58
3.2.1.2 Results....63
3.2.1.3 Discussion and conclusions....71
3.2.2 Spectromicroscopy of Ag nanoparticle films....78
3.2.2.1 Sample preparation and characterization....78
3.2.2.2 Wavelength dependence of the images....80
3.2.2.3 Dependence on laser power....85
3.2.2.4 Microspectroscopy of the emitted electrons....87
3.3. Size-selective time-of-flight spectromicroscopy of MoS_2 nanotubes....91
3.3.1 Sample preparation and characterization....92
3.3.2 Results....93
3.3.3 DOS calculations....94
3.3.4 Discussion and conclusions....95

Conclusions and outlook....98

List of used abbreviations....104

Bibliography....105

Introduction

Metallic thin films structured by various techniques in the field of nanotechnology play a crucial role in high-tech research and development. E.g., the microelectronics industry strongly needs the understanding of the electrophysical properties of thin films and small structures in order to fabricate integrated circuits with critical dimensions of 100 nm or even smaller. Electron emission studies from such nanostructures are a valuable tool for the study of their properties. The comparison of the electron emission from the same sample under different kinds of excitation is important for a good understanding of the electronic properties of solids. In particular, the properties of granular films were of interest for the present work. We excited the system by passing a tunneling current through the film and, alternatively, by illumination with femtosecond laser pulses. The invention of lasers producing ultrashort pulses has opened new fields for experimental studies. Processes which take place on the femtosecond timescale, like electron relaxation, magnetization dynamics, desorption etc. are now observable directly in the time domain. The laser fluence is so high (up to 200 $\mu J \cdot cm^{-2}$) that the threshold behavior of single-photon photoemission is no longer valid and nonlinear multiphoton processes come into play. Electrons can absorb the energy from several photons in one transition event. Based on this phenomenon, energy- and time-resolved two-photon photoemission spectroscopy is an ideal technique to examine the electronic properties of solids and nanoparticles.

A number of bulk materials have been already studied by this technique. It was the purpose of the present work to extend this study to metal nanoparticles and semiconducting nanotubes which have sizes in the range from 2 to 150 nm. We find that the electron emission properties in metal nanoparticles are markedly different to those of bulk metals. The difference is already visible when the surface looses its smoothness, i.e. with appearing of gaps in a continuous film. To understand the peculiarities of the electron emission we used light quanta having energies both higher and lower than the work function of the samples under study. Not only the photon energy of the laser pulses was varied but also their power, pulsewidth and the distance between the pulses. These experiments turned out to be important to gain a good understanding of the mechanisms responsible for the electron

emission. One central question was, whether multiphoton photoemission is the only possible emission mechanism that takes place in the low-dimensional structures.

As the investigated samples were non-homogeneous, it appeared promising to study the objects emitting electrons by means of full-field emission electron microscopy. This allows to visualize the local character of the electron emission from the metal cluster films and nanotubes. Moreover, electron spectroscopy methods (spectromicroscopy and microspectroscopy) can be successfully implemented in the emission electron microscope.

The thesis is organized as follows:

Chapter 1 deals with a description of the behavior of the electron gas excited with a laser pulse that is shorter than the electron-phonon relaxation time. We also discuss the peculiarities, necessary conditions and fingerprints of different electron emission mechanisms. An attempt to find the dependence of the dominant emission mechanism on the size of the emitting particles and the laser flux density using a statistical model of light absorption concludes the theoretical part.

Chapter 2 explains the background of the measurements focusing attention to the excitation sources and detection device, namely, the two femtosecond laser sources used and the photoemission electron microscope.

In **Chapter 3** the obtained experimental results will be presented and discussed. We begin with a laterally resolved investigation of the electrical and emission properties of current-carrying silver cluster films. It will be shown that electron emission starts in the non-linear region of the conductivity curve and shows up in terms of distinct emission centers. The potential distribution and energy spread of the electrons emitted from a single emission center were calculated.

In the second part we describe the peculiarities of electron emission from small metal particles being excited by the femtosecond laser sources. Obtained results are in good agreement with a theoretical description of the electron emission from small metal particles.

In the third part of the experimental chapter we present the application of the novel time-of-flight based spectro-microscopic method to the study of the electronic properties of one-dimensional semiconducting nanotubes.

The drawn conclusions and an outlook for future are completing this thesis.

Einleitung

Metallische Filme, welche durch unterschiedliche nanotechnologische Verfahren strukturiert wurden, spielen eine zentrale Rolle in der high-tech Forschung und Entwicklung. So benötigt die Mikroelektronik-Industrie das Verständnis elektrophysikalischer Eigenschaften dünner Filme und kleiner Strukturen, um Integrated Circuits (ICs) von einer kritischen Größe von 100 nm oder weniger herzustellen.

Elektronenemissions-Studien von solchen Filmen sind ein wertvolles Werkzeug für die Untersuchung solcher Eigenschaften. Der Vergleich der Elektronenemission einer Probe bei verschiedenartiger Anregung ist für ein gutes Verständnis von elektronischen Festkörpereigenschaften wichtig. Insbesondere waren die Eigenschaften granularer Filme für diese Arbeit von Interesse. Das System wurde über einen Tunnelstrom durch den Film angeregt, bzw. alternativ über Femtosekunden-Laserpulse. Die Erfindung von Ultrakurzpuls-Lasern eröffnet neue Felder für experimentelle Studien. Prozesse auf einer Femtosekundenskala, wie Elektronen-Relaxation, Magnetisierungsdynamik, Desorption etc. sind nun direkt und in Echtzeit beobachtbar.

Die Laserfluenz ist dabei so hoch (bis zu 200 $\mu J/cm^2$), dass das Schwellenverhalten von Einzelphotonen-Prozessen seine Gültigkeit verliert, und nichtlineare Multiphotonen-Prozesse dominieren. Elektronen können dabei die Energie von mehreren Photonen in einem Übergang absorbieren. Auf dieser Grundlage basierend ist energie- und zeitaufgelöste Zweiphotonen-Photoemissionsspektroskopie eine ideale Technik, um elektronische Eigenschaften von Festkörpern und Nanopartikeln zu untersuchen.

Eine Reihe von Bulk-Materialien wurden bereits mit dieser Technik studiert. Zweck der vorliegenden Untersuchung war es, die Studie auf Metall-Nanopartikel und halbleitende Nanoröhren auszudehnen, welche im Größenbereich von 2 bis 150 nm liegen. Wir beobachten, dass die Elektronenemissions-Eigenschaften in Metall-Nanopartikeln deutlich unterschiedlich zu denen im Bulk-Metall sind. Der Unterschied ist bereits sichtbar, wenn die Oberfläche Ihre Glätte verliert, z.B. mit dem Auftreten von Lücken in einem homogenen Film. Um die Besonderheiten der Elektronenemission zu verstehen, haben wir Lichtquanten verwendet, deren Energie oberhalb und unterhalb der Austrittsarbeit untersuchter Proben lagen. Nicht nur die Photonen-Energie der Laserpulse wurde variiert, sondern auch ihre Leistung, Pulsbreite und der zeitliche Abstand zwischen den Pulsen. Diese Experimente stellten sich als wichtig heraus, um Einsichten über den Mechanismus der

Elektronenemission zu gewinnen. Eine zentrale Frage war dabei, ob Multiphotonen-Photoemission der einzig mögliche Mechanismus in niederdimensionalen Strukturen ist.

Da die untersuchten Proben inhomogen waren, schien es vielversprechend, Objekte mittels Emissionselektronenmikroskopie im gesamten Gesichtsfeld zu untersuchen. Dies ermöglicht eine Visualisierung des lokalen Charakters der Elektronenemission, von Metallclustern bis hin zu Nanoröhren. Weiterhin können elektronenspektroskopische Methoden (Spektromikroskopie und Mikrospektroskopie) erfolgreich in ein Emissions-Elektronenmikroskop implementiert werden.

Diese Arbeit ist wie folgt gegliedert:

Kapitel 1 beschäftigt sich mit der Beschreibung der Elektronengas-Response auf einen Laserpuls, welcher kürzer ist als die Elektron-Phonon-Relaxationszeit. Dabei werden auch Besonderheiten, notwendige Bedingungen und Kennzeichen verschiedener Elektronenemissions-Mechanismen diskutiert. Der theoretische Teil wird durch eine Untersuchung zur Abhängigkeit des dominanten Emissionsmechanismus von der Größe der emittierenden Teilchen und der Laser-Flußdichte unter Verwendung eines statistischen Modells unter Berücksichtigung von Lichtabsorption abgeschlossen.

In **Kapitel 2** wird der Hintergrund der Messungen erklärt, wobei der Fokus auf den Anregungsquellen und dem Nachweisgerät liegt, d.h., auf den Femtosekunden-Laserquellen und dem Photoemissions-Mikroskop.

In **Kapitel 3** werden die erhaltenen experimentellen Resultate präsentiert und diskutiert, startend mit einer lateral auflösenden Untersuchung der elektrischen und der Emissionseigenschaften stromtragender Silbercluster-Filme. Er wird gezeigt, dass Elektronenemission in dem nichtlinearen Bereich der Leitfähigkeitscharakteristik startet und sich durch ausgezeichnete Emissionszentren offenbart. Die Potentialverteilung und die Energieverschmierung emittierter Elektronen von einem einzigen Emissionszentrum wurden berechnet.

Im zweiten Teil werden die Besonderheiten der Elektronenemission von kleinen Metallpartikeln beschrieben, welche durch Femtosekunden-Laserquellen angeregt wurden. Die erzielten Resultate sind in guter Übereinstimmung mit der theoretischen Beschreibung der Elektronenemission kleiner Metallpartikel.

Im dritten Teil des experimentellen Kapitels werden Anwendungen der neuen Flugzeit-basierten Spektromikroskopie zur Studie elektronischer Eigenschaften eindimensionaler Nanoröhren aufgezeigt.

Die Arbeit endet mit einer zusammenfassenden Schlußfolgerung und einer weiterführenden Perspektive.

Chapter 1. Theory

1.1 Thermal equations

If a tunneling current is passed through a metal island film or a short laser pulse is absorbed, the main part of the energy is dissipated into the electron system. The injected energy is

(i) subsequently distributed among the electrons due to electron-electron scattering eventually leading to the establishment of a transient ″hot electron″ distribution that evolves into a Fermi-Dirac distribution connected with a certain electron temperature, and

(ii) transferred to the lattice by electron-phonon interaction (collisions) leading to the thermalization of the metal electron gas and the lattice.

The time scale of the energy exchange between electron (*e*) and phonon (*ph*) subsystems is called the *relaxation time*. The *e-ph* mean free path is ≈ 30 nm [Sze64]. Considering an electron at the Fermi level with a velocity of 10^8 cm/s, the average collision time is 30 fs. Thus within 1 ps the electron has experienced approximately 30 phonon collisions. The Debye temperature of silver is 226 K [Nei58], so on average an electron will loose energy equivalent to 113 K at each phonon collision. Thus a substantial amount of energy is transferred into the lattice during the typical relaxation time of 1 ps. The time scale of the electron-electron scattering in the perturbed electron gas is much shorter than the relaxation time that allows us to use the two-temperature model to describe the energy exchange process (ii). The validity range of this model is obviously limited to times longer than the *e-e* scattering time scale, lying in the femtosecond range.

We briefly recall the essential results of the two-temperature model [Kag57].

The energy exchange between the electron and phonon subsystems can be written as:

$$-c_{\mathrm{e}}\frac{\partial T_{\mathrm{e}}}{\partial t}=c_{\mathrm{ph}}\frac{\partial T_{\mathrm{ph}}}{\partial t}=\alpha_{\text{e-ph}}(T_{\mathrm{e}}-T_{\mathrm{ph}}) \tag{1.1}$$

where c_{e} and c_{ph} are specific heat capacities of the electron and phonon subsystems and T_{e} and T_{ph} are their temperatures. The parameter $\alpha_{\text{e-ph}}$ is the coupling constant between the two subsystems (electron-phonon coupling constant) and is material specific.

The general case of time- and location-dependent energy balance includes the term of the electron heating source, as well as the temperature gradient that can be calculated by Fourier's law. In the one-dimensional case (where *z* is the direction perpendicular to the metal surface) the following equations can be written:

$$\begin{aligned} c_{\mathrm{e}}\frac{\partial T_{\mathrm{e}}}{\partial t}&=\frac{\partial}{\partial z}\kappa_{\mathrm{e}}\frac{\partial T_{\mathrm{e}}}{\partial z}-\alpha_{\text{e-ph}}(T_{\mathrm{e}}-T_{\mathrm{ph}})+Q(t,z)\\ c_{\mathrm{ph}}\frac{\partial T_{\mathrm{ph}}}{\partial t}&=\frac{\partial}{\partial z}\kappa_{\mathrm{ph}}\frac{\partial T_{\mathrm{ph}}}{\partial z}+\alpha_{\text{e-ph}}(T_{\mathrm{e}}-T_{\mathrm{ph}}). \end{aligned} \tag{1.2}$$

Here, $Q(t,z)=q_{\mathrm{a}}(t)\mu\exp(-\mu z)$ is the absorbed laser energy per unit time, μ^{-1} is the laser beam penetration depth in the metal and $q_{\mathrm{a}}(t)=q(t)(1-R)$ is the radiation intensity existing in the metal which results from the falling intensity $q(t)$ and the reflectivity *R*. The

coefficients κ_e and κ_{ph} describe the heat conductivity of electrons and phonons, respectively. The heat conductivity of the electron subsystem is much higher than that of the phonon subsystem, so in most cases one can neglect the diffusive term in Eq. (1.2).

Since we are dealing with thin films and very short (<1 ps) laser pulses, one can assume that the target volume is heated homogeneously after the laser pulse and the heat conductivity does not play a role in the energy exchange process. If the electrons are Fermi-Dirac-distributed then the heat capacity of the electrons is $c_e = \gamma T_e$. When the energy input is large, then $T_e >> T_{ph}$ and the equation for the electrons is reduced to:

$$c_e \frac{\partial T_e}{\partial t} = \gamma T_e \frac{\partial T_e}{\partial t} = -\alpha_{e\text{-}ph} T_e + \alpha_{e\text{-}ph} T_{ph} \cong -\alpha_{e\text{-}ph} T_e. \quad (1.3)$$

This equation has a simple solution:

$$T_e(t) = T_{e,t=0} - \frac{\alpha_{e\text{-}ph}}{\gamma} t. \quad (1.4)$$

Therefore, cooling of the transient hot electron gas starts as a linear process if $\alpha_{e\text{-}ph}$ and γ are constants (Fig. 1.1). It starts to deviate from the linear behaviour when the electron gas is significantly cooled, so one can not neglect the term that includes T_{ph} (Fig. 1.1).

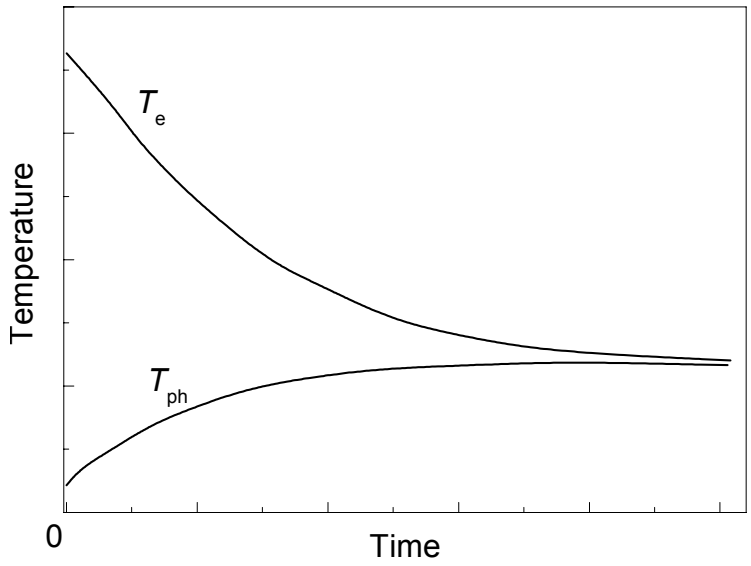

Figure 1.1: The time dependence of the temperatures of the electron and phonon subsystems in the framework of the two-temperature model. Time t=0 denotes the moment of instantaneous heating.

The energy from the laser pulses is absorbed by electrons that become "hot", i.e. in the non-equilibrium with other Fermi-Dirac distributed electrons. Their relaxation time is energy-dependent $\tau_{e\text{-}e} \propto (\varepsilon - \varepsilon_F)^{-2}$ [Lan62] and is between 20 and about 3 fs for bulk Ag and energies ranging from 1.0 to 2.7 eV above ε_F [Bau02]. "Hot" electrons are relaxing due to inelastic scattering with non-excited electrons creating in this way secondaries thus keeping the perturbation (deviation of the distribution function of electrons from Fermi-Dirac) of the electron gas for much longer times. Note, that as long as "hot" electrons exist it is not possible to speak about the "temperature of the electron subsystem". This means that the two-temperature model (Eq. (1.1) and Fig. 1.1) is not valid during a certain time after the

laser pulse. Obviously, after very many *e-e* collisions a Fermi-Dirac distribution is reestablished. This takes about several hundreds of femtoseconds that was found experimentally [Fan92a] and theoretically [Bej97].

The behavior of the electron gas can be described applying Boltzmann collision integrals. In order to consider photon absorption by inverse bremsstrahlung, *e-e* interaction, and *e-ph* interaction, one collision integral should be used for each process. This yields a system of Boltzmann's equations for the distribution function of the electron gas, *f(k),* and of the phonon gas, *g(q),* which read:

$$\begin{aligned} \frac{\partial f(\vec{k})}{\partial t} &= \frac{\partial f(\vec{k})}{\partial t}\Big|Laser + \frac{\partial f(\vec{k})}{\partial t}\Big|e-e + \frac{\partial f(\vec{k})}{\partial t}\Big|e-ph \\ \frac{\partial g(\vec{q})}{\partial t} &= \frac{\partial g(\vec{q})}{\partial t}\Big|ph-e \end{aligned} \qquad (1.5)$$

Before laser irradiation, *f(k)* is a Fermi-Dirac distribution and *g(q)* is a Bose-Einstein distribution, both at T=300 K. This system was numerically solved for aluminium by Rethfeld [Ret02]. The following parameters were used: pulse width 100 fs, J=7×10^9 W/cm^2, λ=630 nm ($h\nu = 0.245\,\varepsilon_F$).

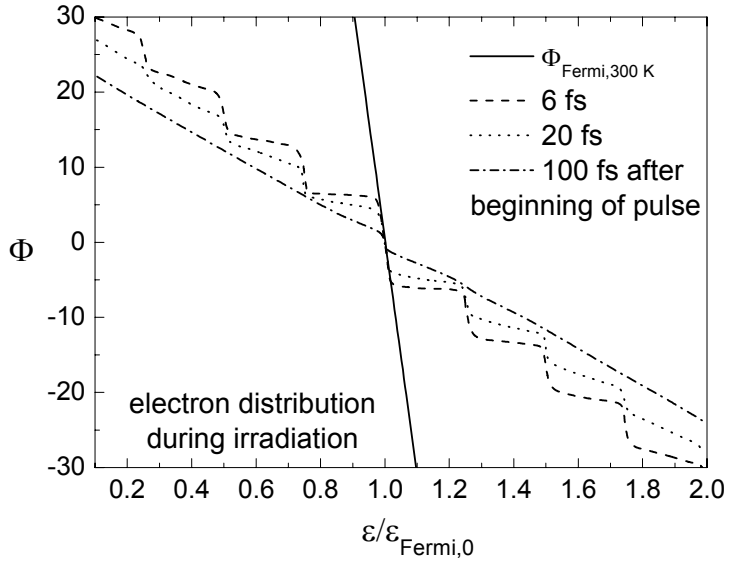

Figure 1.2: Distribution function of free electrons in aluminium during femtosecond-laser irradiation (″Rethfeld plot″). The quantity Φ defined by Eq. (1.6) is shown as a function of electron energy. A laser pulse of 100 fs duration with constant intensity was assumed with a photon energy of $h\nu_L$=1.97 eV=0.245 ε_F and an electric-field amplitude E=1.4×10^8 V/m (from [Ret02]).

Fig. 1.2 shows the calculated transient behavior of the occupation number of free electrons described by the logarithm function $\Phi(\varepsilon)$ as a function of electron energy $\varepsilon / \varepsilon_{Fermi,0}$, which is defined as

$$\Phi\left(f(\varepsilon)\right) = -\ln\left(\frac{1}{f(\varepsilon)} - 1\right) \tag{1.6}$$

In the case of free electrons $f(\varepsilon) = \left(1 + \exp\left\langle \frac{\varepsilon - \varepsilon_F}{k_B T_e} \right\rangle\right)^{-1}$.

The function $\Phi\left(f(\varepsilon)\right)$ can be applied to every distribution function and visualizes the perturbation of $f(\varepsilon)$ from the equilibrium. This function shows the monotonous increase with increase of the density of occupied states $f(\varepsilon)$ and varies from + to - ∞ when $f(\varepsilon)$ increases from 0 to 1. In thermal equilibrium, $\Phi(f(\varepsilon))$ is a linear function with a slope $-1/T_e$ that equals to zero at $\varepsilon / \varepsilon_{\text{Fermi}} = 1$, i.e. at the Fermi energy.

Fig. 1.2 shows the perturbation of the electron gas distribution function during the irradiation with 100 fs laser pulse. The deviation from the ″linear″ Fermi-Dirac distribution is clearly visible through a *steplike* shape of $\Phi(f(\varepsilon))$. The steps have a width equal to $h\nu_L$ and situated symmetrically relative to the zero value. These steps have a simple nature: the absorption of the photons by electrons with the energies $\varepsilon_F \div \varepsilon_F - h\nu_L$ brings them to the energy positions within the interval $\varepsilon_F \div \varepsilon_F + h\nu_L$. In this way two steps are formed below and above the Fermi level. The step above the Fermi energy can be populated by absorption of other photons. At the same time electrons in the energy interval $\varepsilon_F - h\nu_L \div \varepsilon_F - 2h\nu_L$ can also absorb photons because the final states below the Fermi energy became free. Such a steplike distribution function was also predicted theoretically in the region above $\varepsilon_F - h\nu_L$ by Lugovskoy in [Lug94, Lug98] and observed experimentally above ε_F in [Fan92a, Fan92b]. Note, that the ″Rethfeld plot″ visualizes not only the ″hot″ electrons above ε_F but also the electron vacancies created below ε_F.

Fig. 1.2 shows also the time development of the electron distribution function during irradiation. The steps smooth out quickly (see 20 and 100 fs curves) due to *e-e* collisions that decreases the perturbation of the electron gas. At the same time, more electrons are excited from the area below ε_F to higher energies that lead to the decrease of the apparent slope of $\Phi(f(\varepsilon))$. Fig. 1.3 describes the electron thermalization after irradiation. The steps wash out completely after 200 fs what allows again to operate with ″electron temperature″ that is still much higher (3000 K) than the lattice temperature. The energy outflow to the phonon subsystem is visible through the increase of the slope of $\Phi(f(\varepsilon))$. Recall that the slope is proportional to the inverse electron temperature (here 2000 K at 700 fs after irradiation)

It was also shown [Ret02] that the nonequilibrium electron gas does not affect the *e-ph* interaction and the energy exchange can be described by the two-temperature model in the case of excitations near the damage threshold. In contrast, for lower excitations, the energy transfer from electron gas to lattice is influenced by the nonequilibrium of the laser-excited electron gas. In this case, the cooling of the electron gas is delayed compared to a thermalized electron gas of the same internal energy, which is in agreement with earlier experimental results. The reason is that the distribution function of a weakly excited electron gas shows only a very slight deviation from an electron gas at room temperature in the region around the Fermi edge $\varepsilon_{\text{Fermi}} \pm h\nu_L$ where the concentration of electrons, and, therefore, the number of *e-ph* collisions, is largest.

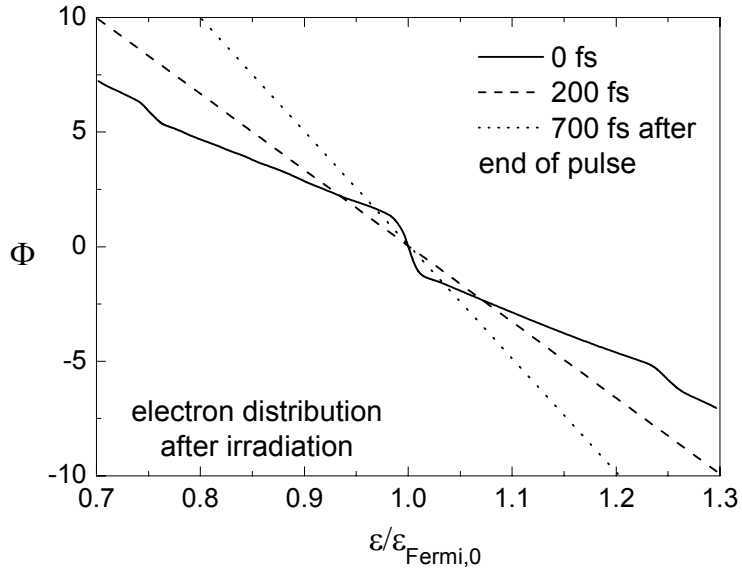

Figure 1.3: Distribution function of free electrons in a section of about $\varepsilon_{\mathrm{Fermi}} \pm h\nu_{\mathrm{L}}$ of the energy scale after irradiation. Like Fig. 1.2 but time scale refers to end of pulse (from [Ret02])

1.2 Mechanisms of electron emission from current-carrying thin metal cluster films

In this section we describe the possible electron emission mechanisms occurring when the power is fed to the nanoparticle by a current passage through a metal cluster film (island film) deposited on an insulator substrate. Three initial conditions should be fulfilled in order to feed energy into the ensemble of metal clusters in this way:

1. The metal cluster film should possess a certain conductivity to provide a current passing through it.

2. To provide a high energy input in the clusters, the thermal coupling between the substrate and the metal cluster film should be as low as possible.

3. The granular film should be close to the percolation threshold, where a tunneling conductance contributes to the total conductance.

Therefore, the objects discussed in this chapter are discontinuous (island) films grown on dielectric substrates that fulfill the second condition. The clusters are formed in the intermediate stage of growth effected by the Volmer-Weber (3D) mechanism [Bau72]. In thick (>100 nm) films one measures essentially bulk electrical properties. In thinner films, in the thickness range up to a few nanometers, one measures a strongly reduced (down by many orders of magnitude) conductivity. In these films both the size of most of the islands and the gaps between them are of the order of several nanometers. Then, due to considerable electron tunnelling transparency of the nanometre potential barriers [Neu62], the island film has a highly reduced but some conductivity with a non-linear current-voltage characteristic.

Two models were suggested to explain the electron emission from such island films. The first of them, the field emission model [Dit72], assumes that the local electric field at one of the adjacent islands is high enough to cause field emission. It is also implied that a part of the field emission current is branched off to the anode (extractor electrode of the electron microscope lens, see section 2.2) placed over the film. The phenomenon of field emission is

well investigated and will be briefly described in section 1.2.1. The second model is referred to the model of emission of hot electrons generated in small metal particles [Tom66; Bel90]. It is described in section 1.2.2.

1.2.1 Field emission mechanism

The term field emission indicates the extraction of electrons from a solid by tunnelling through the surface potential barrier as sketched in Fig. 1.4. ϕ and ε denote the work function and the potential energy of the electrons in the conduction band. This is normally achieved by applying a very high negative potential to the metal. If the local electric field E is sufficiently high *(E* has to reach approximately 10^7 V·cm^{-1}), electrons may tunnel directly from the valence band through the reduced potential barrier into vacuum. For a given applied potential, the electron emission is enhanced at sharp protruding objects, where the resulting electric field strength is locally amplified. The field amplification increases with decreasing radius of curvature of the surface.

In a one-stage process it is assumed that field-emitted electrons reach the anode immediately (or maybe after a reflection from the adjacent island) (Fig. 1.5). This model suggests the emission from nanoscale (<100 nm) island ″cathodes″ (C) to large islands serving as ″anodes″ (A) being located at a distance of the order of 1 μm from the ″cathodes″.

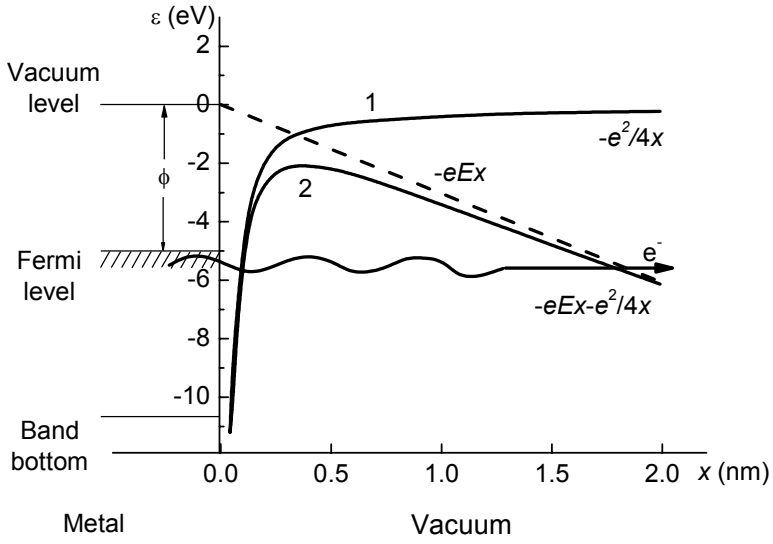

Figure 1.4: The potential barrier of a metal-vacuum interface. Curve 1, mirror charge potential; curve 2, potential barrier in a strong field (approx 10^7 V·cm^{-1}); *-eEx* is the contribution of the electric field *E*.

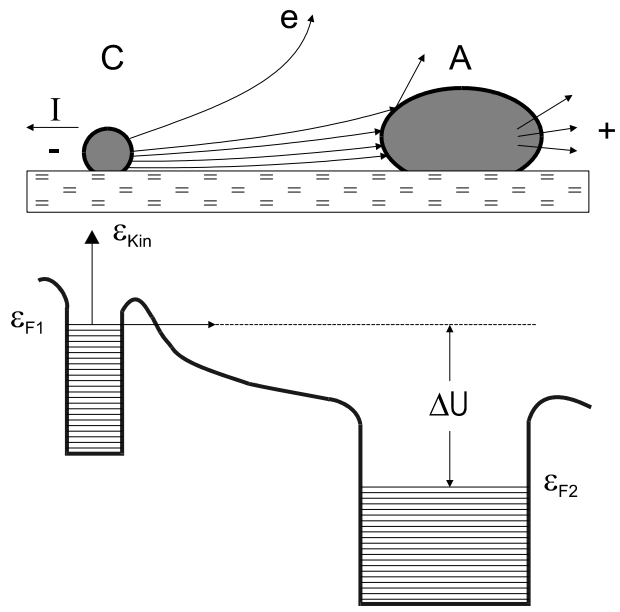

Figure 1.5: Illustration of the field emission model suggested to explain the electron emission from metal cluster films during the passage of a current *I*. The kinetic energy scale of the emitted electrons refers to the Fermi energy of the emitter particle ε_{F1}.

1.2.2 Emission of hot electrons

The model used to describe emission of hot electrons is a three-stage process which involves

(i) tunnelling of electrons to the adjacent island,
(ii) transfer of their excess energy to the electrons of the island (heating of the electron gas) and
(iii) emission of the hot electrons into vacuum (Fig. 1.6)

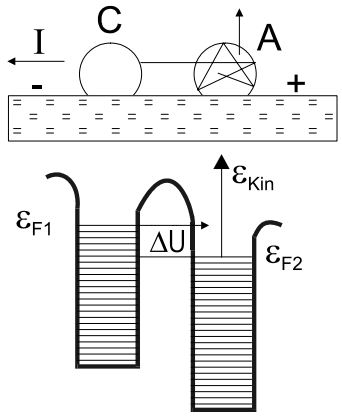

Figure 1.6: Illustration of the model of hot electron emission from a nanoparticle. Beyond Fig. 1.5, the heating of the electron gas in particle A is the origin of electron emission. Here the kinetic energy scale of the emitted electrons refers to ε_{F2}.

How can hot electrons be generated in cluster metal films (stage (ii))?
To answer this question, we recall the balance equation

$$Q = \alpha_{\text{e-ph}}(T_{\text{e}} - T_{\text{ph}}) \qquad (1.7)$$

which links the power Q absorbed by the electron subsystem of metal cluster A with the electron and lattice temperatures, T_{e} and T_{ph}. The coefficient $\alpha_{\text{e-ph}}$ determines the strength of electron-lattice energy transfer.

The heating process can be qualitatively illustrated by a model, see Fig. 1.7. Suppose there are two vessels, different in cross-section, the narrow vessel being inserted into the wider one. Assume the cross-sections of the narrow and wide vessels to be proportional to c_{e} and c_{ph}, where c_{e} and c_{ph} are the electron and lattice heat capacities, respectively. The electron subsystem is known to have a much smaller heat capacity than the phonon subsystem. Let a fluid flow Q be poured into the narrow vessel; the fluid can flow out from it through an outlet H_1 into the wide vessel. The cross-section of this outlet is assumed to be proportional to $\alpha_{\text{e-ph}}$. The flux of the fluid through a larger outlet H_2 in the wide vessel simulates heat transfer from the nanoparticle lattice to the substrate. Then the levels of the fluid in the narrow and wide vessels accumulated at some instant mimic T_{e} and T_{ph}, respectively.

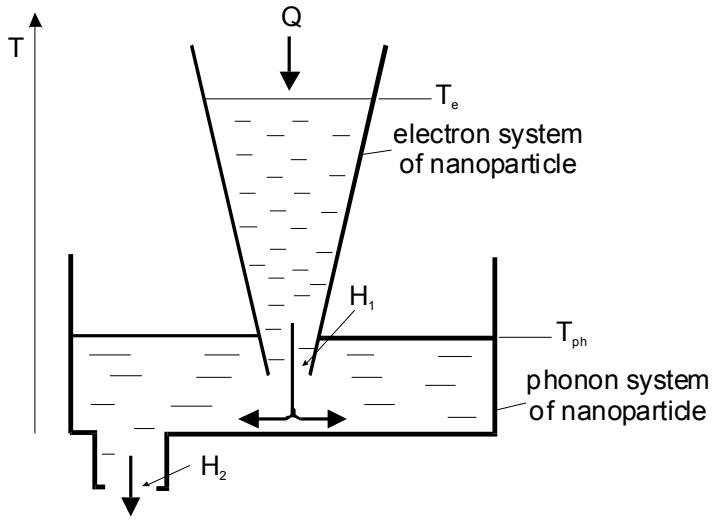

Figure 1.7: Model of communicating vessels illustrating the electron-lattice energy transfer and nonequilibrium heating of the electron gas in a small particle on a substrate. T_{e} and T_{ph} denote the temperatures of the electron and phonon subsystem, Q denotes the power impact and H_1 and H_2 the energy dissipation from the electron to the phonon system and from the particle phonon system to the substrate, respectively. See text for explanations.

Thus, if the fluid is let in at a constant rate starting at $t = 0$, then in the time interval $\tau_{\text{e}} \sim c_{\text{e}} / \alpha_{\text{e-ph}}$ a quasi-equilibrium (dynamic equilibrium) state is established in the narrow vessel at which the whole incoming flux will flow out through the outlet H_1 into the wide vessel. It means that the balance condition (1.7) is satisfied. The stabilization of the liquid level in the wide vessel is attained due to outflow through the rather wide slit which mimics the heat contact between the island and the substrate. The height of this level corresponds to the lattice temperature, which obviously must be low enough to avoid the melting and

evaporation of the island. As can be seen from this model and Eq. (1.7), the gap between the temperatures of electrons and phonons is wider the larger is the energy flux Q and the smaller is the *e-ph* coupling coefficient $\alpha_{\text{e-ph}}$, because $Q/\alpha_{\text{e-ph}} = T_{\text{e}} - T_{\text{ph}}$. The cross-section of the narrow vessel widens with increasing liquid level, because $c_{\text{e}} \propto \gamma T_{\text{e}}$.

To attain a high steady-state value of T_{e}, the flux Q should be sufficiently large (depending on $\alpha_{\text{e-ph}}$). On the other hand, the magnitude of T_{ph} should not exceed the destruction limit determined by melting and/or evaporation of the particle.

In bulk metals, owing to high electron concentration, Q should be rather large. Electrons are rapidly heated in a time interval of about $\tau_{\text{e}} \sim 500$ fs, but within a time of $\tau_{\text{ph}} \sim$ 1-10 ps the phonon temperature becomes equal to T_{e}, and the metal will be molten and evaporated. This is the reason why experimental observations of hot electrons in bulk metals have been reported only for time intervals $\tau_{\text{e}} < t < \tau_{\text{ph}}$, e.g. when samples are irradiated by short and intense laser pulses [Ani77, Agr80].

In cluster metal films, there are three important differences from this situation [Bel90, Bel92, Fed00, Fed93, Tom97]:

(i) for a metal particle whose dimensions are smaller than the electron mean free path, the coefficient $\alpha_{\text{e-ph}}$ can be reduced by orders of magnitude in comparison with the bulk metal allowing for a steady-state value of T_{e} that is much higher than T_{ph} if the cluster has a good heat contact with the dielectric substrate;

(ii) considerable power densities can be pumped into small metal particles; and

(iii) an island having a good heat contact with the dielectric substrate is able to pass intense energy fluxes without being destructed, and its thermal stability increases as the size is reduced. Of course, the metal islands can be thermally destroyed, but only at power fluxes that are orders of magnitude higher than those sustained by bulk metals.

1.3 Mechanisms of electron emission under femtosecond laser excitation

In section 1.1 it was shown using the Rethfeld formalism [Ret02] that the absorption of a high photon flux leads to a steplike distribution function of the electrons on time scales up to several hundreds of femtoseconds. To escape out of the metal the electron should have an excess energy higher than the energy difference between the vacuum and Fermi levels (work function). In general, this can be realized in two ways: either simultaneous absorption of a number of photons gaining a necessary amount of energy to overcome the potential barrier or to find itself in the high-energy part of the Fermi-Dirac distribution possessing an energy higher than the work function.

In this section we will define and describe the main peculiarities of the different emission mechanisms. Models 1–3 imply the quantum nature of light, model 4 considers a wave mechanism, i.e. electrons tunneling through the surface barrier due to the strong optical electromagnetic field.

1. Simultaneous absorption of energy from several photons by **one** electron or photon absorption by an electron from the high-energy wing of a non-thermalized step-like ″hot″ electron distribution (multiphoton photoemission *n*PPE).
2. Direct thermionic emission from the transient hot electron gas.

3. Photon absorption by an electron from the thermalized ″hot″ electron distribution (thermally-assisted photoemission).
4. Optical field emission.

1.3.1 Multiphoton photoemission (*n*PPE)

Threshold (classical, or 1-photon) photoemission (Fig. 1.8a) stands for the emission of an electron after absorption of a single photon. A. Einstein could explain on the basis of experimental results, the outer photoelectric effect, by postulating the particle character of light, following M. Planck's earlier concept of energy quanta. By illuminating a surface with photons of a certain energy ($\varepsilon = h\nu$), there is a non-vanishing probability of the photons to get absorbed. Einstein's photoeffect law in its *classical* form must be fulfilled to initiate the photoemission: $h\nu > \phi$.

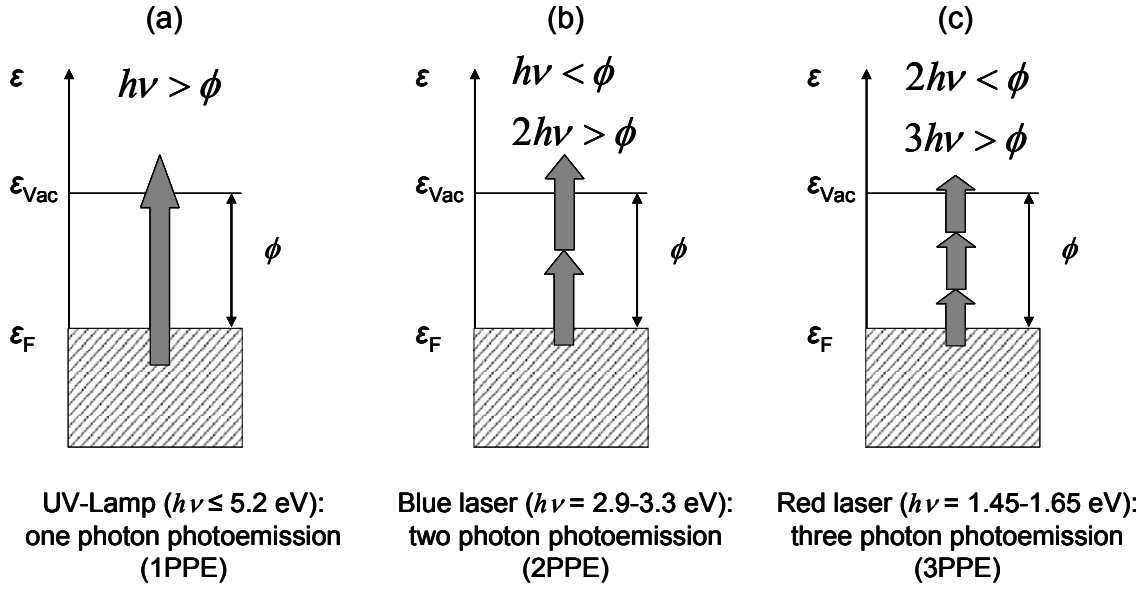

Figure 1.8: Schematic representation of the different *n*PPE mechanisms occurring if the sample is illuminated with the ultra-violet (UV) lamp (a), the blue fs-laser (b) or the red fs-laser (c), respectively. The arrows indicate the transition of an electron into a state above the vacuum level $\varepsilon_{\mathrm{Vac}}$, following the absorption of 1, 2 or 3 photons. The 2PPE and 3PPE transition probabilities are enhanced if real intermediate states are present.

The probability of the threshold photoemission (like each quantum transition) is described by Fermi`s golden rule:

$$w^{(1)} = 2\pi \left| V_{\varepsilon k}^{(1)} \right|^2 \rho_\varepsilon . \qquad (1.8)$$

Where $V_{\varepsilon k}^{(1)}$ is the 1-photon ($V^{(1)}$) matrix element, corresponding to the electron transition from the bound state *k* to the continuum state with kinetic energy ε, ρ_ε is the density of the final states. The 1-photon transition operator in the dipole approximation is written as:

$$V^{(1)} = \left[\boldsymbol{d} \times \boldsymbol{E} \right] = e\left[\boldsymbol{r} \times \boldsymbol{E} \right] \qquad (1.9)$$

where ***d***=*e**r*** is the dipole moment, ***E*** is the strength of the external electric field, which is assumed to be only time-dependent. Therefore, it follows that $w^{(1)} \sim E^2 \sim I_L$, where I_L is the light intensity. The linear dependence $w^{(1)}(I_L)$ grounds the term ″linear photoemission″ that is often used for 1-photon photoemission. Eq. (1.8) can be written in the form $w^{(1)} = \alpha_{\varepsilon k}^{(1)} I_L$, where $\alpha_{\varepsilon k}^{(1)}$ is the 1-photon photoemission cross-section that has a dimension cm^2. It is a characteristic of the sample and geometry and does not depend on the light intensity.

In the phototransition electrons are excited from a band below the Fermi level to an unoccupied band above Fermi level. If this excitation level lies above the vacuum level, the electron may escape into the vacuum. The kinetic energy of the emitted electrons can be measured, and thus this phenomenon led quite fast to the discipline of photoemission spectroscopy (PES), with its main advantage to depict the density of states of the occupied energy bands[1] or core level positions. Today, it is a versatile technique to study electronic bands in solids and at surfaces and adsorbates. An illustration of an ultraviolet photoemission spectroscopy (UPS) spectrum is given in Fig. 1.9, for the case of silver. The binding energy is referred to the Fermi energy. Below ε_F the 5s conduction band is visible, the maximum below 3 eV corresponds to the 4d valence electrons.

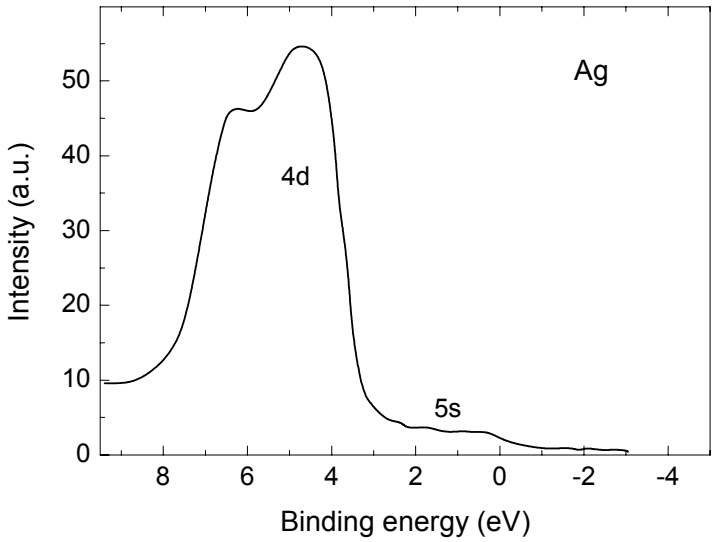

Figure 1.9: UPS (He I, $h\nu$ = 21.2eV) spectrum of the valence bands of silver, from [Kit05].

Now we will consider the case, when the linear photoemission is energetically impossible from the classical point of view ($h\nu < \phi$). When the light intensity is high enough (what is realized for fs-lasers) the electron can be emitted by absorbing 2 or more photons (Fig. 1.8b,c)[2]. Einstein's rule in its generalized formulation $nh\nu > \phi$ should be applied here.

[1] To be more precise, one measures the "joint density of states", i.e. the combination of the density of states of all energy levels involved.

[2] For metallic nanoparticles, the light is also effectively absorbed by plasmon excitation. An electron can get the necessary amount of energy absorbing several light quanta or quanta from several decayed plasmons. In both cases it will absorb an energy multiple of $h\nu$.

The main characteristic of multiphoton photoemission is the number of photons *n* which should be absorbed to emit an electron into vacuum. *n* is called the *order of nonlinearity* or the *order of photoemission*. The minimum number is given by $n = \left[(\phi / h\nu) + 1\right]$ with square brackets denoting the integer value.

The probability of multiphoton photoemission of order *n* is described again by Fermi`s golden rule:

$$w^{(n)} = 2\pi \left| V_{\varepsilon k}^{(n)} \right|^2 \rho_\varepsilon = \alpha_{\varepsilon k}^{(n)} E^{2n} = \alpha_{\varepsilon k}^{(n)} I_{\mathrm{L}}^n. \tag{1.10}$$

It differs from the case of linear photoemission by the form of the matrix element that is now the multiphoton matrix element. In the framework of non-stationary perturbation theory it can be written as [Lan77]:

$$V_{\varepsilon k}^n \sim \sum_{l,m,\ldots,p} \frac{V_{\varepsilon p}^{(1)} \ldots V_{ml}^{(1)} V_{lk}^{(1)}}{\left(\omega_{\varepsilon p} - n\omega\right) \ldots \left(\omega_{lk} - \omega\right)}. \tag{1.11}$$

$V^{(1)}$ are the 1-photon matrix elements corresponding to the 1-photon transitions between involved initial (*k*), *real* intermediate (*l, m, ..., p*) and final (ε) states with energy $\hbar\omega_k, \hbar\omega_l, \hbar\omega_m \ldots \hbar\omega_p, \hbar\omega_\varepsilon$, respectively. The unoccupied states are considered as real if the lifetime of the electron is $>10^{-8}$ s and is determined by a spontaneous decay to lower-lying states. The electron lifetime in a virtual state is determined by the energy-time uncertainty principle $\Delta\varepsilon \cdot \Delta t \geq \hbar$, where $\Delta\varepsilon$ is the energy difference between the virtual and the closest real state. For $\Delta\varepsilon$ =1eV we end up with a lifetime of 10^{-16} s. The denominators in Eq. (1.11) reflect the property of a multiphoton transition to proceed from a real initial to real final state through virtual intermediate states.

In analogy to $\alpha_{\varepsilon k}^{(1)}$ the multiphoton cross-section $\alpha_{\varepsilon k}^{(n)}$ is introduced. It is clear from Eq. (1.9) that the probability of a true (i.e. isolated) multiphoton transition (without heating effects of the electron gas) depends on the intensity I_{L} of the light by a power law. Its exponent is equal to the order of nonlinearity *n*. Hence, the dimension of the multiphoton cross-section also depends on *n*, i.e $\left[\alpha^n\right] = \mathrm{cm}^{2n} \cdot \mathrm{s}^{n-1}$.

2PPE is a powerful tool for studying the electronic properties of solids [Aes95; Bau02; Fan92b; Kno98; Pet97; Pfe04]. The typical 2PPE process and the resulting spectrum for bulk silver are shown in Fig. 1.10. The curve in Fig. 1.10a denotes a density-of-states calculation for Ag [Sha85]. In the following chapters, the measured 2PPE spectra will be shown to be functions of different energy scales, with respect to initial, intermediate and final states. In Fig. 1.10a we summarize the relevant quantities that determine the final electron energy $\varepsilon_{\mathrm{exp}}$, as measured by an electron analyzer. Fig. 1.10b shows a 2PPE spectrum measured for a clean Ag (100) single crystal surface. $\varepsilon_{\mathrm{exp}}^{\mathrm{min}}, \varepsilon_{\mathrm{exp}}^{\mathrm{max}}$ are the low and high energy cut-offs of the spectra. The energy of the final state is plotted with respect to the Fermi level of the sample. This is an unambiguous definition in contrast to ″kinetic energy″, the zero of which is problematic in heterogeneous systems.

The energy of the final state with respect to the local vacuum energy (in other words the kinetic energy $\varepsilon_{\mathrm{kin}}$ of the electron in front of the sample) is determined by the energy distance from the low energy cut-off $\varepsilon_{\mathrm{exp}}^{\mathrm{min}}$ of the spectrum and is given by [Cah03]

$$\varepsilon_{\mathrm{kin}} = \varepsilon_{\mathrm{exp}} - \varepsilon_{\mathrm{exp}}^{\mathrm{min}} \tag{1.12}$$

provided a sufficiently high negative bias is applied to the sample so that no escaping electrons are repelled by the analyzer entrance slit.

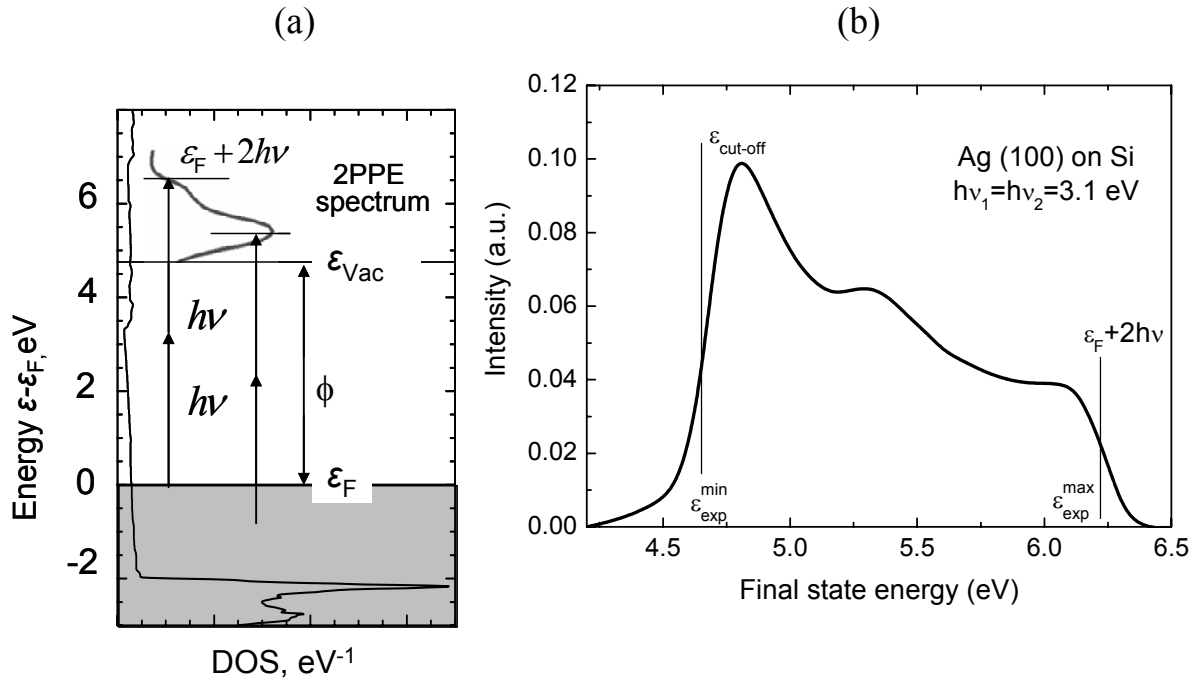

Figure 1.10: (a) Simultaneous absorption of 2 photons by an electron from the 6sp-band and (b) resulting 2PPE spectrum of bulk Ag (100) on Si (own measurement).

The energy of the involved intermediate level with respect to ε_F depends on the excitation energy within the first 2PPE-step $h\nu$ and is given by

$$\varepsilon - \varepsilon_F = h\nu - (\varepsilon_{exp}^{max} - \varepsilon_{exp}). \quad (1.13)$$

In the case of a metal, the binding energy of the initial state ε_b with respect to the Fermi edge ε_F can be calculated from the measured electron energy ε_{exp} and the high energy cut-off ε_{exp}^{max} of the 2PPE spectrum:

$$\varepsilon_b = \varepsilon_{exp}^{max} - \varepsilon_{exp}. \quad (1.14)$$

A peak in a 2PPE spectrum can be easily related to an initial or (real) intermediate state by the peak shifts with a change of the incident photon energy. When varying the photon energy by $\Delta h\nu$, the peak positions corresponding to initial occupied states shift by $\Delta\varepsilon_{kin} = 2\Delta h\nu$, whereas the peak positions corresponding to intermediate states shift only linearly[3] by $\Delta\varepsilon_{kin} = \Delta h\nu$. Taking the restrictions for the calculation of ε_{kin} into account the

[3] There is one exception from this rule. For example, in silver the free-electron like sp-band near the Fermi level gives rise to direct interband transitions. Due to the bending of the bands the peak with final state energy at ~5.4 eV in Fig. 1.10b disperses with varying photon energy with approximately $1 \cdot \Delta h\nu$. In this case the additional UPS measurement (where the band-to-band transition disappears) is needed to prove the nature of the peak.

work function ϕ of the investigated sample can be calculated from the width $\Delta\varepsilon = \varepsilon_{\mathrm{exp}}^{\mathrm{max}} - \varepsilon_{\mathrm{exp}}^{\mathrm{min}}$ of the measured spectra and the excitation energy $h\nu$, i.e. $\phi = 2h\nu - \Delta\varepsilon$. Referring the final state energy scale of Fig. 1.10b to ε_{F}, we obtain simply $\phi = \varepsilon_{\mathrm{exp}}^{\mathrm{min}}$.

1.3.2 Thermionic emission

Thermal electron emission from a heated metal surface is explained by the fact that the Fermi edge broadens thermally to such an extent that the high-energy tail extends above the vacuum level. The width of the cut-off is about $4k_{\mathrm{B}}T$ which is only 1 eV at 3000 K but the foot of the distribution then extends towards $\varepsilon_{\mathrm{Vac}}$ so that these electrons can overcome the surface barrier. At 3000 K the value of the Fermi-Dirac distribution function in the vicinity of $\varepsilon_{\mathrm{Vac}}$ is significant $f(4.9\mathrm{eV})_{T=3000\mathrm{K}} = 6\cdot10^{-9}$ while at room temperature $f(4.9\mathrm{eV})_{T=300\mathrm{K}} = 6\cdot10^{-83}$. The thermionic emission current density is given by the Richardson-Dushman equation

$$j = AT^2 e^{-\frac{\phi}{k_{\mathrm{B}}T}} \tag{1.15}$$

where j is the current density of the emission (in mA/mm^2), A the Richardson constant, T the absolute temperature, ϕ the work function of the material and k_{B} the Boltzmann constant.

We may ask the question whether this mechanism can contribute in femtosecond laser excitation. Initially the energy is delivered by photons what might suggest to talk about photoemission. On the other hand it is possible to evaporate deposited metal clusters of certain sizes by strong fs-laser radiation [Hub05]. Of course this will clearly be accompanied by true thermionic emission. The Rethfeld plot in Fig. 1.2 gives a criterion to distinguish between *n*PPE and thermionic emission: when the escaping electron was still in the step-like distribution it is clearly *n*PPE, if it was in the strongly smoothed (thermalized) distribution we should rather term it thermionic emission. The latter electron has no memory on the photon operator (Eq. (1.8)), because it suffered from inelastic collisions. This makes clear that there is no sharp transition between *n*PPE and thermionic emission. Conceptually, the electron's ″memory″ on the dipole operator is a well defined criterion for true photoemission. This is in complete analogy to common 1PPE where we clearly distinguish between the photoelectrons (with their characteristic energy and angular distribution) and the ″true secondaries″ that have no memory on the initial photoexcitation. Similarly, there is a possibility of experimental distinction: the photon operator leads to the well-known anisotropic angular distributions that are even more pronounced for multiphoton photoemission [Hip83]. In contrast, thermionic emission (similar to true secondaries) is characterized by an isotropic angular distribution except for the trivial angular term $\cos\theta$ for a plane surface.

It is possible to estimate the temperature by fitting the high-energy cut-off (at $\varepsilon_{\mathrm{exp}}^{\mathrm{max}}$) of the photoelectron spectra by a Fermi-Dirac function [Fan92a]. A sharp high-energy cut-off is a fingerprint of a nascent (not-thermalized) electron distribution and therefore is an evidence of the multiphoton photoemission mechanism. The ″smearing″ of the Fermi level onset indicates that electrons are emitted from a thermalized hot electron gas.

1.3.3 Thermally-assisted *n*PPE

If the photon energy is larger than the work function the photoemission current should be proportional (see Eq. (1.8)) to the photon intensity corresponding to the normal threshold photoemission. The number of emitted electrons by unit energy of absorbed light is proportional to the number of electrons within the metal which have energies and velocity components normal to the surface such that, when augmented by energy $h\nu$, they are sufficient to overcome the surface potential barrier. Therefore, just below the damage threshold, when the metal surface is already heated close to the melting point, nonequilibrium heating of electrons modifies the photoemission characteristic. So-called thermally-assisted photoemission takes place.

The first theory that successfully explained the temperature dependence of linear photoemission near the work function threshold was given by Fowler [Fow31] and was subsequently improved by DuBridge [Dub32]. Their starting point is the assumption that the electrons in metal obey the Fermi-Dirac statistics and are uniformly distributed in momentum space. Moreover, the following assumptions are made:

(i) The absorption probability of a photon is independent of the initial state of the electron.

(ii) An electron may escape from the metal if its ″normal kinetic energy″, associated with the component of velocity normal to the surface, is greater than the potential-energy barrier.

(iii) The whole energy of the photon ($h\nu$) when absorbed, is used to increase only the normal kinetic energy of the electron; its velocity components parallel to the surface remain unchanged.

(iv) The number of electrons emitted per absorbed photon is proportional to the number of electrons per unit volume of the metal whose normal kinetic energy, when increased by $h\nu$, is sufficient to escape the potential energy barrier.

The current density is then given by

$$j(\mathbf{r},t) = a\left(\frac{e}{h\nu}\right)A(1-R)I_{\mathrm{L}}(\mathbf{r},t)T^2(\mathbf{r},t)F\left(\frac{h\nu-\phi}{k_{\mathrm{B}}T(\mathbf{r},t)}\right). \tag{1.16}$$

Where e is the electron charge, a is a constant, R the reflectivity of the sample, A the theoretical Richardson coefficient (120 A/cm^{2}K^2), $h\nu$ the laser photon energy, ϕ the work function, k_{B} the Boltzmann constant, $I_{\mathrm{L}}(\mathbf{r},t)$ the incident laser intensity, and $T(\mathbf{r},t)$ the absolute temperature of the sample, both at coordinate $\mathbf{r}$ and time t. The function F is the Fowler function

$$F(x) = \begin{cases} \displaystyle\sum_{m=1}^{\infty}(-1)^{m+1}e^{mx}/m^2 & \text{for } x \le 0 \\ \displaystyle\frac{\pi^2}{6}+\frac{x^2}{2}-\sum_{m=1}^{\infty}(-1)^{m+1}e^{-mx}/m^2 & \text{for } x > 0 \end{cases} \tag{1.17}$$

tabulated in [Dub32]. Note, that for low intensity, T can be taken as the constant ambient temperature and j reduces to the simple $j \propto I_{\mathrm{L}}$ relationship describing the one-photon photoemission process. At higher intensity T is no longer the ambient temperature and the thermally-assisted photoemission comes into play. At still higher laser intensity thermionic emission becomes dominant, as is given by Eq. (1.15).

The model of Fowler and DuBridge was later extended by Bechtel [Bec73] to include *n*-photon photoemission. The basic assumption is that the total current density j is the superposition of partial current densities j_n, each of which has a simple interpretation

$$j(\mathrm{r},t)=\sum_{n=0}^{\infty} j_n(\mathrm{r},t) \tag{1.18}$$

where

$$j_n(\mathbf{r},t)=a_n\left(\frac{e}{h\nu}\right)^n A(1-R)^n I_{\mathrm{L}}^n(\mathbf{r},t)T^2(\mathbf{r},t)F\left(\frac{nh\nu-\phi}{k_{\mathrm{B}}T(\mathbf{r},t)}\right). \tag{1.19}$$

The constant a_n is a sample dependent constant which by analogy to the pure *n*PPE contains the transition matrix elements and electron escape probability and is proportional to the *n*PPE constant.

If one keeps only the first term of the Fowler function j_0 is independent of the incident laser intensity and reduces to (1.15). The current depends on the sample temperature, which is intensity dependent, but intensity does not enter directly in the equation for j_0. j_1 is just the Fowler equation for linear photoemission. For low intensity *n*PPE , in accordance with the spirit of perturbation theory, one keeps only the *n*th term j_n. For example, in the case of the excitation with a low intensity red laser beam at 800 nm (3PPE), the temperature rise of the sample is insignificant and only j_3 has any significant contribution

$$j_3(\mathbf{r},t)=a_3(e/h\nu)^3 A(1-R)^3 I_{\mathrm{L}}^3(\mathbf{r},t)T^2(\mathbf{r},t)F\left(\frac{3h\nu-\phi}{k_{\mathrm{B}}T(\mathbf{r},t)}\right). \tag{1.20}$$

However, for higher intensities, the temperature T in the equation above becomes an intensity dependent function and the photocurrent rises faster than I_{L}^3. Physically, the heating of the electron gas by the laser pulse causes the Fermi-Dirac distribution to develop a high-energy tail and more electrons can then participate in the three-photon photoemission process. This is presented graphically in Fig. 1.11.

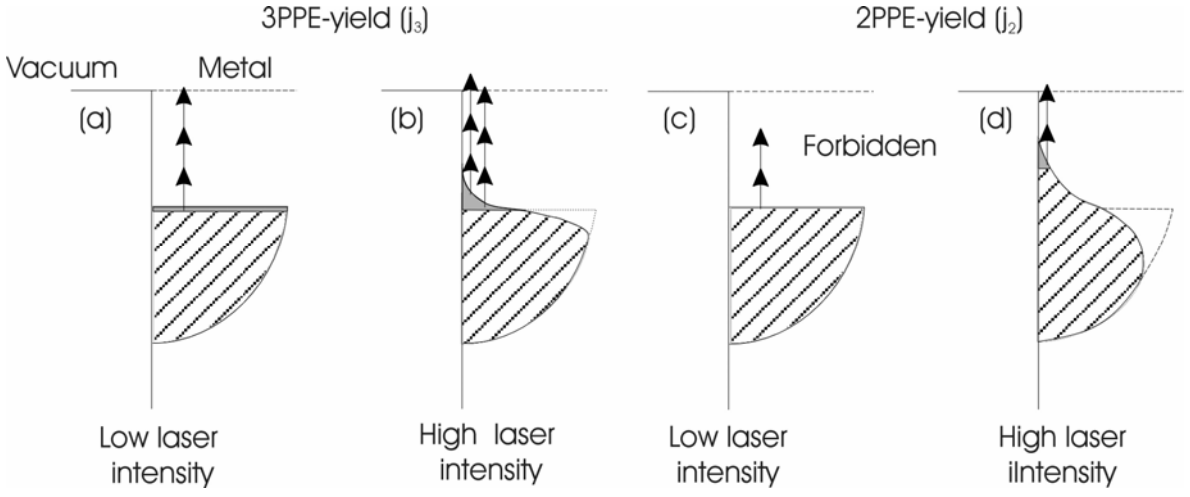

Figure 1.11: Schematic representation of three-photon photoemission without (a) and with heating (b) of the sample. With two photons ground-state photoemission is impossible (c) and only thermally-assisted photoemission (d) is possible. (b) and (d) will be termed thermally-assisted three- and two-photon photoemission, respectively.

For still higher intensities, partial currents beyond j_3 will start contributing to the total photoemission current. The situation, shown in Fig. 1.11d can be realized when only two photons are needed to eject the electron from the high-energy tail of the Fermi-Dirac distribution. Since this process is forbidden at lower intensities it is called *thermally-assisted 2-photon photoemission*. It is described by

$$j_2(\mathbf{r},t) = a_2\left(\frac{e}{h\nu}\right)^2 A(1-R)^2 I_{\mathrm{L}}^2(\mathbf{r},t)T^2(\mathbf{r},t)F\left(\frac{2h\nu-\phi}{k_{\mathrm{B}}T(\mathbf{r},t)}\right) \tag{1.21}$$

with a negative argument for the Fowler function.

In this regime the dependence of the photoemission current on the intensity of the laser beam will show a fractional power law with exponent higher than three for the case of Fig. 1.11b. A distinction should be made at this point between the terms *nonlinear* and *multiphoton* to avoid any confusion. A pure multiphoton process has an integer power dependence on the laser intensity, whereas a nonlinear process may have any dependence on the laser intensity. In a study of electron emission from gold with 1.9 eV photons, for example, Logothetis at al. [Log67] found a power law much higher than 3 at laser fluences greater than 10 MWcm^{-2} (see Fig. 1.12).

The fluences of the laser systems utilized were high enough for significant heating of the electron gas, although the pulse width is much shorter than in the experiment shown in Fig. 1.12. The study of the power law of the electron emission signal will be a good tool for studying the electron emission mechanism and also the dynamics of the nonequilibrium electron gas.

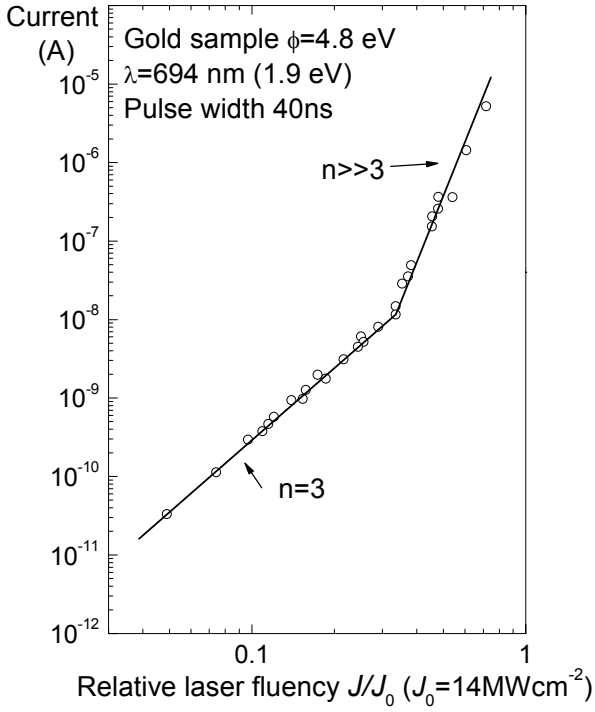

Figure 1.12: Photoemission current versus relative laser intensity of the first harmonic of a ruby laser. J_0=14 MWcm^{-2}. The photon beam diameter was 4.6 mm to avoid pure thermionic emission (from [Log67]).

1.3.4 Optical field emission

In section 1.2.1 the possibility of a static field emission mechanism was shown, occurring when a very high static negative potential is applied to a metal tip or nanoparticle. In principle, a similar emission mechanism can also be obtained dynamically when illuminating the metal with sufficiently intense laser light. In this case, the electric field E of the incoming wave may temporarily (E is time- and space-dependent) lower the surface potential barrier and allow electrons to tunnel through it. When a sufficiently intense laser illuminates the surface, the potential barrier is temporarily lowered. For free atoms this phenomenon was studied extensively in the context of attosecond spectroscopy [Dre05].

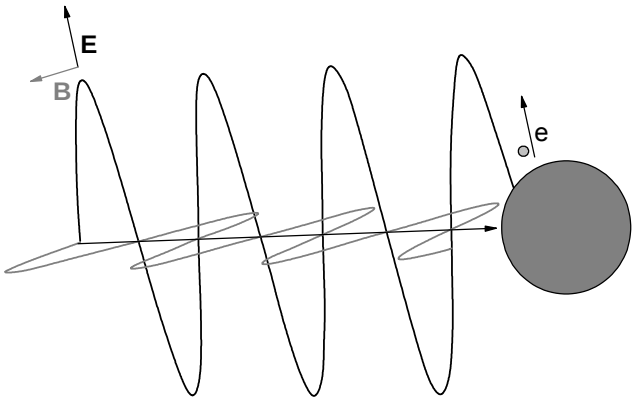

Figure 1.13: Electromagnetic wave of the laser near a small metal particle. Note that the polarization dependence of the electron emission will be generally weaker than in the case of bulk material, because ***E*** is always perpendicular to a certain region of the surface of a small particle.

Since the laser radiation is coherent it can be considered as a classical electromagnetic wave (Fig. 1.13). The magnetic component of this wave can be neglected.[4] The potential distortion in the vicinity of a small metal particle is schematically shown in Fig. 1.14.

The periodic electric field $E(t)$ acts on the surface potential of the small metal particle. If the unexcited electron (path A) or the electron excited by one or two photons to a state with energy between ε_F and ε_{Vac} (path B) tunnels through the lowered potential barrier (2) during a half-period of the optical field, it becomes free. It is clear from Fig. 1.14 that the probability of tunneling increases when the frequency of the laser decreases and when the electrons are thermally excited as indicated by the dots.

The reason for this is that the tunneling rate is determined essentially by the mean free time of the electron passing through the barrier of width $l = \phi / eE$, the average electron velocity is of the order of $\sqrt{\phi / m}$ (m being the electron mass). Therefore up to frequencies of the order of $\omega_t = \dfrac{eE}{\sqrt{2m\phi}}$ the tunnel effect is determined by the maximum value of the field intensity. At higher frequencies a frequency dependence of the tunneling probability is expected, since the electron does not have enough time to cross the barrier within one half-cycle of the optical wave.

[4] A magnetic field acts on the particles with the same force as an electric field if they are moving with relativistic velocities. Free electrons in metals are obviously non-relativistic.

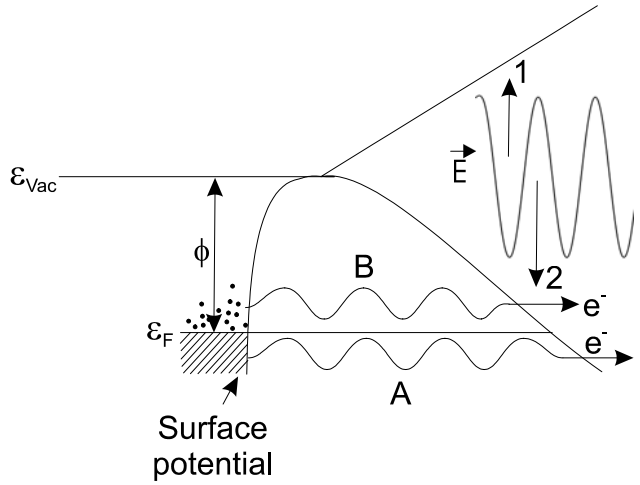

Figure 1.14: Appearance of tunneling in the alternating electric field. During one half-period the field in the vicinity of the small particle changes from curve (1) to (2). Paths A and B correspond to ″cold″ field emission and thermally-assisted field emission, respectively.

The common formula which goes over into the usual formula for the tunnel effect at low frequencies and very strong fields when $\omega << \omega_t$ and describes multiphoton photoemission when $\omega >> \omega_t$ was obtained by [Sil70] following [Kel64] and [Bun65]. The boundary between the multiphoton and tunnel emission is determined by the condition $\gamma = \frac{\omega\sqrt{2m\phi}}{eE} = 1$. When the so-called adiabatic parameter $\gamma >> 1$, the multiphoton photoemission is the main emission mechanism and the photocurrent is given by $j \sim I_{\mathrm{L}}^{n} \sim (E^2)^n$. In the case of strong fields $\gamma << 1$ the optical field emission mechanism exhibits a $j \sim E^2 \exp(-a/E)$ dependence (Fig. 1.15). Here, $n = [\phi/h\nu + 1]$ with square brackets denoting the integer value and a is a constant. From the general concept of multiphoton photoemission such a reduction of the slope is connected with a decrease of the number of photons *n* which are necessary to eject an electron. For bulk silver (ϕ=4.8eV) the transition interval should be expected at E~2.8×10^7 V/cm or J~1000 GW/cm^2. In metal nanoclusters the transition can occur at much (few orders of magnitude) lower powers due to the field enhancement on rough surfaces as discussed theoretically [Mes81] and observed recently on Ag nanoparticles [Cin04, Cin05].

The possibility of the excitation of localized surface plasmons in surface roughness features and nanoparticles produces an enhanced near-zone field in the vicinity of the roughness features themselves [Sha00]. In addition, the presence of sharp protruding inhomogeneities on the surface may strongly enhance the local field strength like in static field emission. The lowering of the potential barrier at surface roughness features can thus be by orders of magnitude more pronounced than for a homogeneous surface.

Let us finally consider the energetic signature of *n*PPE vs optical field emission. *n*PPE from metallic surfaces and nanoparticles is characterized by a sharp Fermi edge at a final state energy of $\varepsilon_{\mathrm{exp}}^{\mathrm{max}} = nh\nu$ and a low energy cut-off at $\varepsilon_{\mathrm{exp}}^{\mathrm{min}} = \phi$ (right and left cut-offs in Fig. 1.10b). If the nanoparticles charge the whole spectrum will shift accordingly. For

optical field emission the Fermi edge of the metal is the relevant energy (cf. Fig. 1.14, path A or a somewhat elevated energy if thermal excitation is additionally involved (path B)).

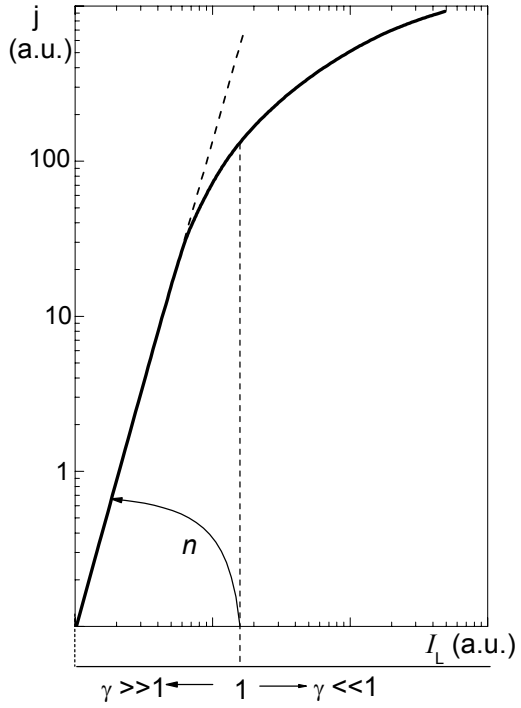

Figure 1.15: The dependence of the photocurrent j on the laser intensity I_L in a log-log plot. When the adiabatic parameter $\gamma >> 1$, n-photon photoemission is observed (slope n), when $\gamma << 1$, tunnelling in the strong optical field occurs (after [Kel64]).

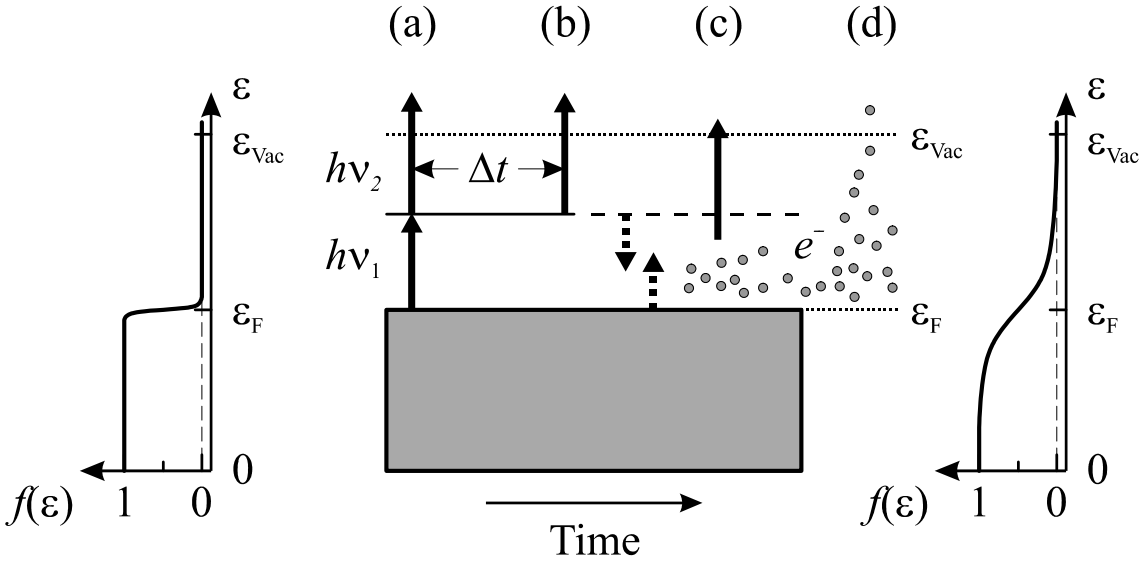

Figure 1.16: Schematic energy-versus-time plot of the different emission mechanisms, i.e. simultaneous (a), sequential (b) and thermally-assisted (c) nPPE as well as thermionic emission (d). The Fermi distribution reflects the cold (left) and hot (right) electron gas.

Concluding this section, Fig. 1.16 summarizes the possible emission processes and their time scales. Simultaneous *n*PPE (a) happens instantly, whereas sequential *n*PPE (b) may involve a time delay Δt in the few fs range. Thermally-assisted *n*PPE (c) may involve a time delay on the time scale where the steplike Rethfeld plot smoothes but before the thermal energy is dissipated into the phonon system, i.e. below about 1 ps. Thermionic emission (d) does not essentially depend on the duration of the laser pulse. The lower limit is again the time where the Rethfeld plot smoothes out, there is no upper limit because even a cw laser can yield thermionic emission. Finally, optical field emission (not shown) happens during one half cycle of the light wave, i.e. within 0.7 fs for 800 nm radiation.

1.4 Statistical approach to the light absorption by small metal particles

When the interaction volume on the sample is large enough to absorb a lot of photons in one laser pulse the mean value of the absorbed energy can be used to describe the photoemission. However, this approach is not valid when the mean number of photons absorbed by a particle per pulse is of the order of units or tenths. As one can see from Table 2.1 only 0.32 photons on average fall on an area of lateral size 1 nm^2 in one ″blue″ laser pulse. In this regime, obviously, quantum statistics must be applied.

In this paragraph we perform calculations of the absorbed energy distribution over an ensemble of silver nanoparticles and make on this ground a conclusion about the critical particle size where the emission mechanism changes from *n*PPE to thermionic emission.
We use a statistical model to describe the absorption process which does not take into account any absorption resonance phenomenon (like particle plasmon resonances) but highlights the effects connected with the quantum nature of light and fluctuations of the absorbed energy (Fig. 1.17).

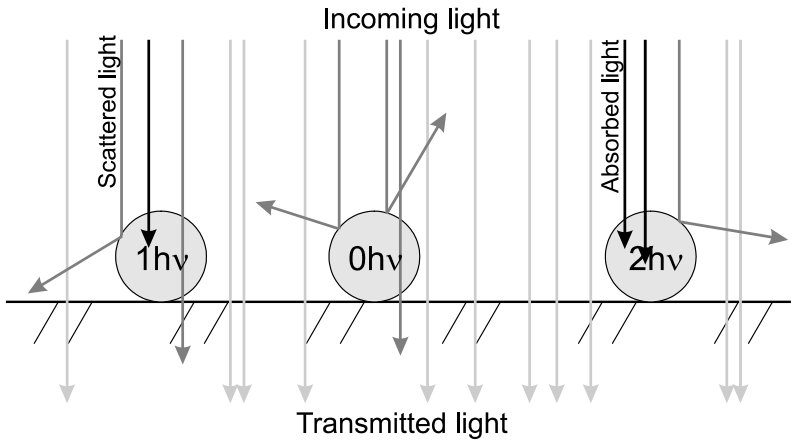

Figure 1.17: Model for the statistical approach of light absorption by small metal particles.

Let us consider an area S of the substrate and a deposited spherical particle of radius r and follow the assumption that the probability p_0 for one photon falling into this area to hit the particle is: $p_0 = \pi r^2/S$. Onto the area S fall $n = JS/h\nu$ photons (J is the fluence [J·cm^{-2}]) in one laser pulse. Then the probability $P_{n,m}$ for the particle to get m photons out of n can be described by the Bernoulli formula:

$$P_{n,m} = \frac{n!}{m!(n-m)!} p_0^m (1-p_0)^{n-m}. \quad (1.22)$$

Relying on Mie theory calculations [Boh83] we use a reasonable value of 0.2 for the absorption efficiency A of $r = 20$ nm particles and assume it to be proportional to the particle radius that is valid for $r \leq 20$ nm and 3 eV photons according to Mie theory[5]. The amount of absorbed photons is proportional to the volume of the particle i.e. to r^3. If the considered area S tends to infinity with the photon flux remaining constant, n also tends to infinity and $p_0 \to 0$. In this case one can use the Poisson approximation to calculate the probability of every absorption event:

$$P_m = \frac{y^m}{m!} e^{-y} \quad (1.23)$$

where $y = np_0$ *and* $n = AJS/h\nu$.

The results of this calculation of the statistical probability for a particle to absorb m photons in one laser pulse as a function of m and r are shown in Fig. 1.18 for $J = 6 \cdot 10^{-6}$ J·cm^{-2}. This fluence is comparable to that of our blue laser beam, see Table 2.1. It is seen that for particles of 2 and 5 nm radius the most probable event is to absorb no photons, for $r = 10$ nm four photons and for $r = 20$ nm already 33 photons.

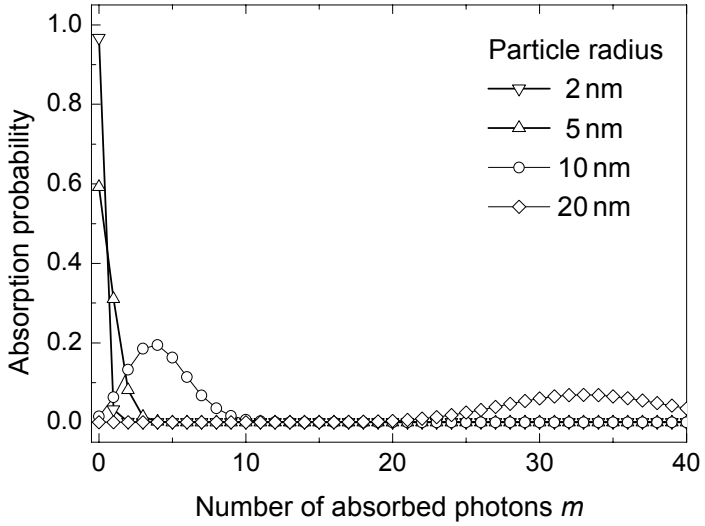

Figure 1.18: Statistical probability to absorb a certain number of photons m by particles with different radii r ; photon energy $h\nu$ = 3 eV.

Now let us estimate the rise of the electron temperature after absorption of m photons with an energy $h\nu$. We integrate the heat balance equation (1.1) and derive T_e from it taking into account that the heat capacity c_e of the electron gas depends on its temperature, and for N_e electrons takes the following form [Lan68]:

$$c_e = \frac{\pi^2 k_B^2}{2\varepsilon_F} T_e N_e = \gamma T_e N_e \quad (1.24)$$

[5] Note, however, that the absorption coefficient can even be larger than 1 in the maximum of a plasmon resonance as derived by Messinger et al. [Mes81].

where $\gamma = \frac{\pi^2 k_B^2}{2\varepsilon_F} = 6.2 \cdot 10^{-9}$ eV/K^2

Thus the electron temperature T_e is a function of the absorbed energy $m \cdot h\nu$ and the initial temperature T_0 which is equal to the phonon temperature T_{ph}:

$$T_e = \sqrt{3.2 \cdot 10^8 \frac{m \cdot h\nu}{N_e} + T_0^2}. \qquad (1.25)$$

Here we assume the number of free electrons in silver N_e to be equal to the number of atoms (one free electron per atom), that is $N_e = 4\pi r^3 \rho / 3$ ($\rho_{Ag} = 59$ atoms/nm^3). We further consider instantaneous impact of all photons and neglect, in a kind of ″sudden approximation″, the energy dissipation from the electrons to the particle phonon system and to the substrate.

The Eq. (1.25) is visualized in Fig. 1.19. It is clearly seen that absorption of even a few photons leads to very high electron temperatures in small (r<4 nm) particles, whereas absorption of 10000 photons does not lead to a significant change of the electron temperature in a 100 nm particle. Note that a 100 nm particle is hit by 2500 ″blue″ photons in one laser pulse (see Table 1.1). This results in a maximal electron temperature of only 633 K.

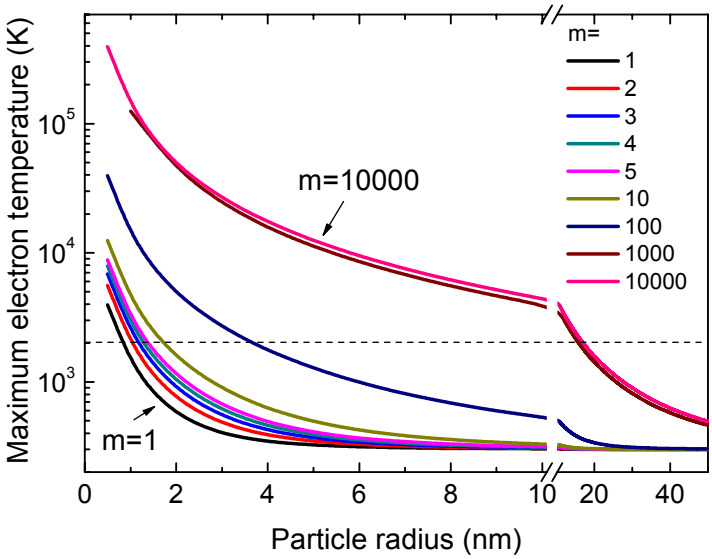

Figure 1.19: Dependence of the electron temperature on the number m of absorbed photons. The dashed line denotes the onset for thermionic emission.

In Fig. 1.20 the statistical probabilities to achieve a certain temperature are presented for different $h\nu$ and laser pulse fluences. One can see that in small particles the temperature fluctuations can be extremely high (similar probability for a broad temperature range) but drop down very fast with increasing r. Lower $h\nu$ with the same fluence gives better statistics and therefore lower probabilities for high temperatures.

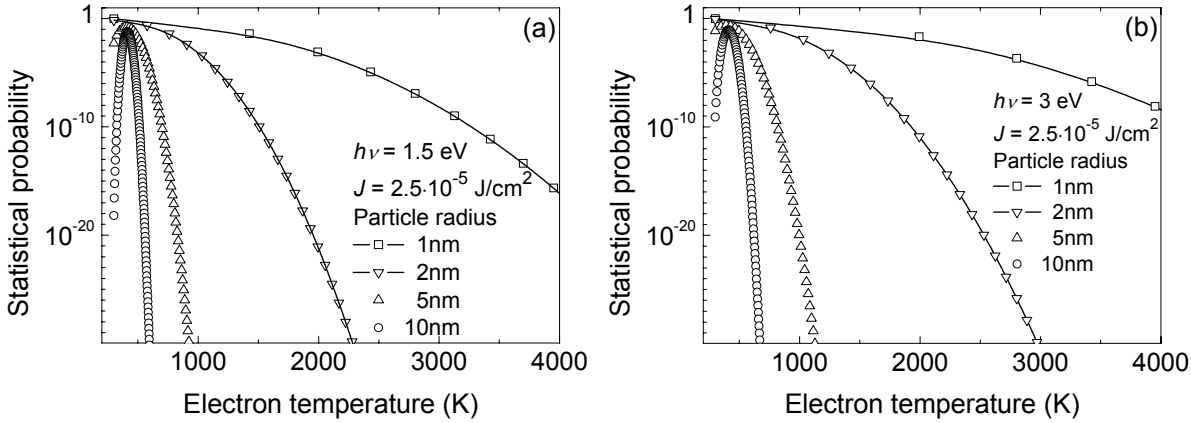

Figure 1.20: Statistical probability of electron temperatures in small metal particles under excitation by the ″red″ (a) and ″blue″ (b) laser beams.

If the system consists of a large number of identical particles being irradiated with the same fluence, Eqs. 1.23 and 1.25 represent a temperature distribution of the ensemble. A general view of the thermionic emission intensity j_{Therm} can be calculated over such a distribution using the Richardson-Dushman equation (1.10) and $P_m(r)$ as a weighting parameter in the sum

$$j_{\mathrm{Therm}} \sim \sum_m P_m(r) r^2 T_{\mathrm{e}}^2 e^{-\frac{\varphi}{k_{\mathrm{B}} T_{\mathrm{e}}}}. \qquad (1.26).$$

The result is presented in Fig. 1.21 as a function of particle radius for three different fluences. Extremely strong intensity enhancement for particles with $r < 5$ nm is obviously provided by high probabilities of significant deviation of the absorbed energy from the mean values and by the very strong nonlinearity of the Richardson-Dushman law. Note that the amount of silver diminishes here $\propto r^3$.

We can apply this model to the case of pure 2PPE (or 3PPE) that also exhibits a nonlinear dependence on the laser beam power. To calculate the probability of 2PPE one can also apply a statistical approach for the description of the process of energy transfer from plasmons to electrons of the particle. The probability $\tilde{P}$ for a given electron of the particle to get two energy quanta from m plasmons excited by one laser pulse can be calculated by means of Eq. (1.22) with number of trials n equal to m and number of events m equal to 2. The total two-photon photoemission intensity $j_{2\mathrm{PPE}}$ for an ensemble of particles normalized by the number of electrons in the particle N_{e} is given as follows:

$$\frac{j_{2PPE}(r)}{N_{\mathrm{e}}} \sim \frac{1}{N_{\mathrm{e}}} \sum_{m=2}^{\infty} P_m(r) N_{\mathrm{e}} \tilde{P}_{m,2}(r) = \sum_{m=2}^{\infty} \frac{y^m}{m!} e^{-y} \frac{N_{\mathrm{e}} m!}{2(m-2)!} \left(\frac{1}{N_{\mathrm{e}}}\right)^2 \left(1 - \frac{1}{N_{\mathrm{e}}}\right)^{m-2} \approx$$
$$\approx \frac{y^2 e^{-y}}{2N_{\mathrm{e}}^2} \sum_{l=0}^{\infty} \frac{y^l}{l!} = \frac{y^2}{2N_{\mathrm{e}}^2} = const. \qquad (1.27)$$

This ratio is independent of r because y and N_{e} are both $\sim r^3$, so the particle size cancels out.

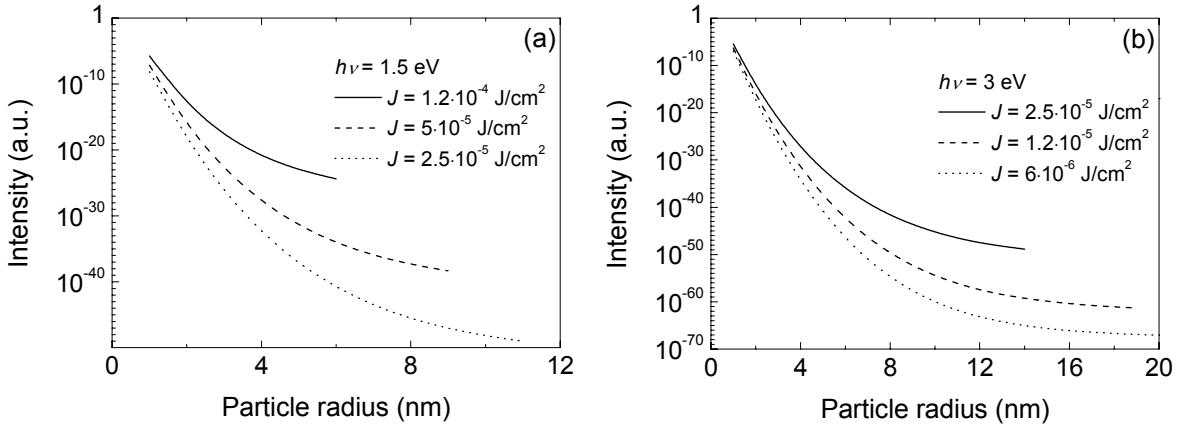

Figure 1.21: Statistical probability of thermionic emission intensity as a function of radius for different fluences.

This means that in the framework of the presented model two-photon photoemission is not sensitive to fluctuation of the absorbed energy in small particles and the 2PPE intensity is proportional to the amount of material (N_e) in the particle. The result for 3PPE and 2PPE is shown in Fig. 1.22a and b, respectively. In reality, this model is altered because the plasmon excitation probability depends on the particle size and shows a resonance-like behavior [Kre93].

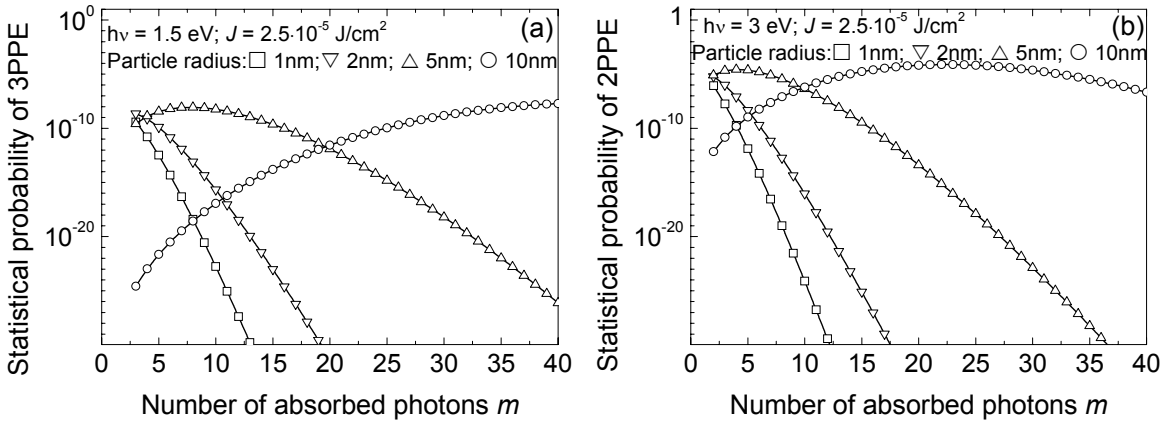

Figure 1.22: Statistical probability of multiphoton photoemission, 3PPE (a) and 2PPE (b) as function of the number *m* of absorbed photons for ″red″ (a) and ″blue″ laser pulses (b).

To find the particle size where multiphoton photoemission is changed to thermionic emission the probabilities of two-photon photoemission $P_m N_e \tilde{P}_{m,2}$ (Fig.1. 22a) and three-photon photoemission $P_m N_e \tilde{P}_{m,3}$ (Fig. 1.22b) have to be compared to the probabilities to achieve an electron gas temperature sufficient for thermionic emission (~2000K). Direct comparison of the maximal value of *n*PPE probability in Fig. 1.22a, b and the corresponding probability for a particle to achieve 2000K in Fig. 1.20a, b locates the switching point to be between r = 1nm and 2 nm.

Chapter 2.
Experimental details

The UHV setup consisted mainly of two parts: the preparation chamber containing components for sample preparation and characterization, and the main chamber for the photoemission electron microscopy studies. The chambers are connected by a sample transfer mechanism. We discuss very briefly the standard UHV components and give a detailed description of the used excitation sources and implemented experimental techniques.

2.1 UHV components

The preparation chamber was coupled to a sample transfer system, which allowed the insertion of new samples without breaking the vacuum (base pressure was 10^{-9} mbar) and their further transfer into the main chamber. The manipulator in the preparation chamber carried a sample stage, supplied with a resistive heater on the back of the sample. Direct heating could also be achieved by sending a current through the sample itself. The preparation chamber was equipped with a cesium dispenser. Deposition of cesium as adsorbate leads to a considerable decrease (down to 2.5 eV) of the work function of the object under study [Kin23, Lan71]. This allowed us to influence the electrophysical and emission properties of the metal films. The basic equipment of the preparation chamber consisted of a sputter gun, two electron-beam evaporators (evaporation by electron bombardment heating), a quartz balance to allow calibration of the evaporators, and a low-energy electron diffraction (LEED) system, used to check cleanness and geometrical order of the substrate and sample surfaces.

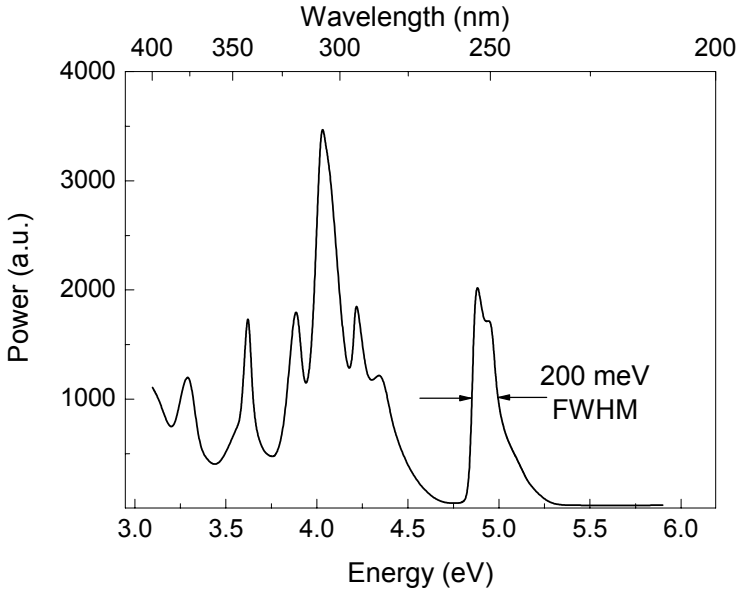

Figure 2.1: Spectrum of the UV light source (type HBO 100W/2, Osram). Note that the Franck-Hertz-line at 4.9 eV has a FWHM of 200 meV due to pressure broadening.

The photoemission electron microscope (PEEM) was mounted in a stainless steel main UHV chamber, kept at a base pressure of $8 \cdot 10^{-11}$ mbar. The base pressure was reached by pumping with a turbomolecular pump, an ion pump used in combination with a Ti-sublimation pump, and after baking out of the system at 150°C for 50 hours. The walls of the main chamber were covered with a μ-metal shield to avoid the effects of magnetic stray fields on the detection system. This is an absolute necessity if one is interested in detecting low energy electrons, as in the experiments described in this work.

Two fused silica viewports with a high transparency for UV radiation were mounted to allow illumination of the sample by the laser and by a high-pressure UV lamp. The latter was a standard UV mercury short arc lamp HBO 100W/2. Its spectrum is shown in Fig. 2.1. It was used as a reference excitation source for threshold photoemission.

2.2 General layout of the photoemission electron microscope (PEEM)

The PEEM is a full-field imaging microscope. It can image any flat conducting surface. We used a standard Focus PEEM [Sch02a] that is based on a three-lens electrostatic instrument with low column energy. Fig. 2.2 illustrates its basic principle. The planar sample acts as a cathode and is an integral element of the first lens. The photoelectrons emitted from the surface are accelerated by a positive voltage at the extractor electrode with respect to the sample potential. The standard technique of a strong electrostatic acceleration field between the sample and the first electrode of the objective lens ensures a good base resolution in the region of 20 nm, depending on sample quality. A size-selectable and adjustable contrast aperture in the backfocal plane of the objective lens restricts the range of starting angles of the electrons on the sample and thus optimizes contrast and resolution. A stigmator/deflector octopole compensates the astigmatism originating from geometrical misalignment. Finally, the photoelectron image is intensified by a multichannelplate (MCP) and imaged by a fluorescent screen for observation with a charge-coupled device (CCD) camera. The contrast observed in a PEEM image obtained using UV light results from spatial variations of the electron yield as a consequence of lateral variations of the local work function and of the surface topography. We will additionally exploit a potential contrast that is explained in section 3.1.4.

2.2.1 PEEM in time-of-flight mode

The standard imaging unit of a PEEM can be replaced by a time-resolving image detector (Fig. 2.3). A special asymmetric einzel-lens retards the beam down to a low kinetic energy of typically 50 eV in the drift tube without loosing the image quality. The energy distribution of the electrons is dispersed in the drift tube leading to different arrival times like in conventional time-of-flight electron spectroscopy. If the photon source is pulsed (in our case fs-laser radiation), this spatio-temporal dispersion can be exploited for energy-filtered imaging when using a time-resolving image detector. We used a 3D (x, y, t)-resolving delayline image detector bearing several important advantages compared to fast CCD cameras. This detector records the spatial (lateral) and time coordinates of every single detected electron. The kinetic energy $\varepsilon_{\mathrm{kin}}$ is related to the time-of-flight τ by the relation:

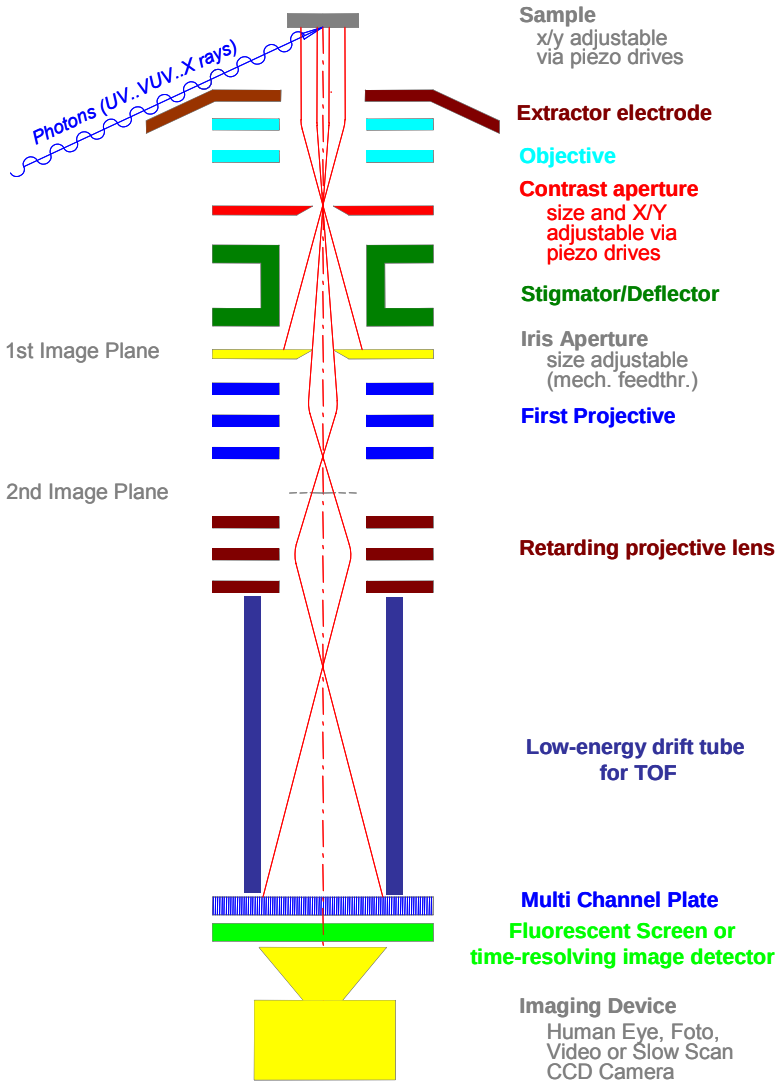

Figure 2.2: Principle of the PEEM with electrostatic lens system.

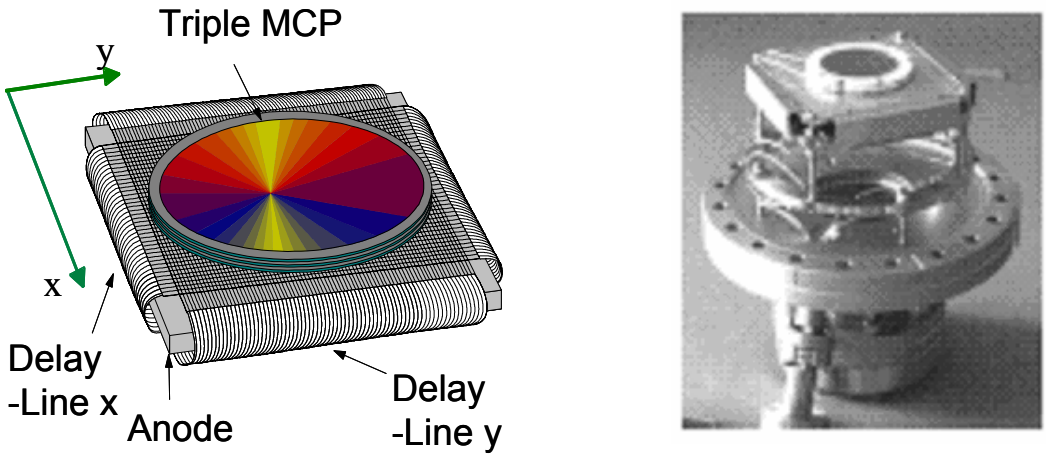

Figure 2.3: MCP detector with delay-line anode replacing the standard imaging unit of the PEEM for time-of-flight spectromicroscopy.

$$\varepsilon_{\mathrm{kin}} = \frac{mL^2}{2\tau^2} \qquad (2.1)$$

where m is the electron mass and L is the length of the drift tube. Details on its performance in an earlier stage of development can be found in [Oel01]. Its time resolution of about 120 ps is superior to fast CCD-cameras. For a typical value of drift energy (50 eV) the energy resolution is about 150 meV. The delayline image detector samples all time slices simultaneously. The ″thickness″ of the individual time slices (corresponding to energy slices) can be defined and optimized after image acquisition via the imaging software. In addition, spatial regions of interest can be defined to extract local spectroscopic information.

2.2.2 PEEM with imaging energy filter

The imaging energy filter (IEF) is a unit for PEEMs dedicated for spectromicroscopy. Its main advantages are the simplicity of operation and absence of restrictions on the excitation source. The energy filter consists of a preretardation lens forming a telescopic beam and a two-grid retarding field analyzer mounted in front of the imaging unit (Fig. 2.4). The retarding field acts as a high-pass energy filter. The first grid G1 is mechanically and electrically connected to L2; the second grid G2 is kept at the retarding potential U_{ret} (provided by a computer-controlled power supply). The two grids form a homogeneous electrical field that retards the electrons. All electrons with energies

$$\varepsilon = \varepsilon_{\mathrm{kin}} + e(U_{\mathrm{sample}} - U_{\mathrm{ret}}) > 0 \qquad (2.2)$$

will be able to pass the second grid and are registered by the imaging unit. ε_{kin} is the starting energy with respect to the vacuum level of the sample, $(U_{\mathrm{sample}} - U_{\mathrm{ret}})$ is the voltage difference between sample and second grid. The high-pass behavior is indicated in Fig. 2.5. The electrons in the shaded region will be able to pass the second grid.

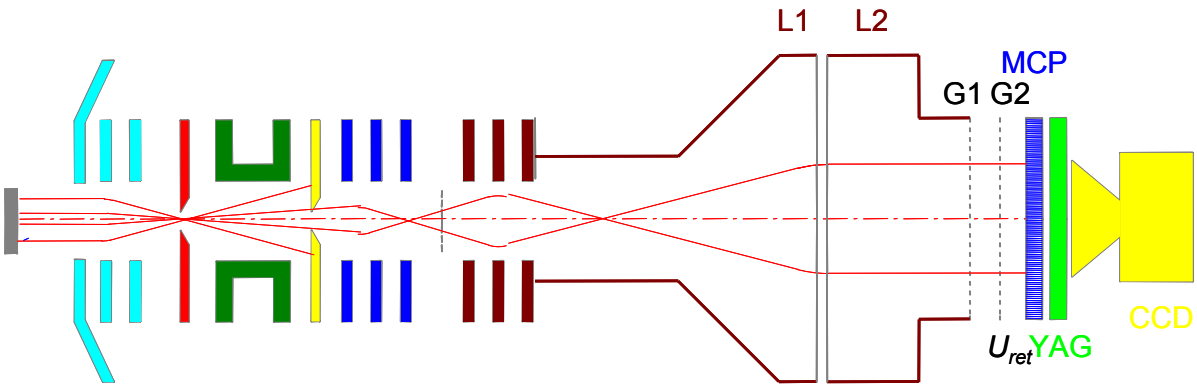

Figure 2.4: Schematic cross section of the PEEM with imaging energy filter. Two lens elements L1 and L2 form the preretardation lens. The two grids G1 and G2, the microchannelplate MCP and the Yttrium-Aluminum-Garnet screen form the imaging energy filter unit. The two grids shape a homogeneous electrostatic field that acts as high-pass energy filter. (From www.focus-gmbh.com)

The energy resolution depends on the preretardation voltage and is better than 2% of the kinetic energy of electrons when entering the first grid. To obtain a high energy resolution we have simulated the electron trajectories and calculated the optimal voltages of PEEM lenses at very low (<100 V) column potentials. We have reached an energy resolution of

about 300 meV while the lateral resolution was better than 200 nm. An example for a retardation energy of 0.7 eV in the second grid is shown in Fig. 2.6a. The spectrum of bulk silver under UV excitation is shown in Fig. 2.6b.

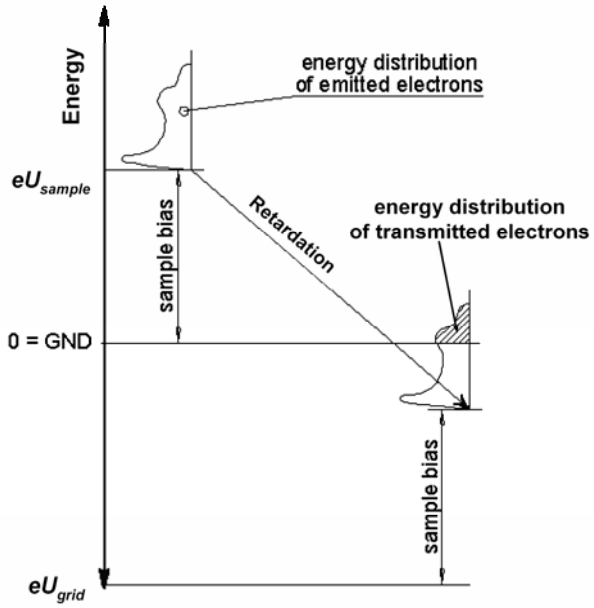

Figure 2.5: Electron energy diagram for the retarding-field energy filter. The shaded region indicates the part of the energy-distribution that is transmitted through the second grid here referred to ground GND. (From www.focus-gmbh.com)

(a) (b)

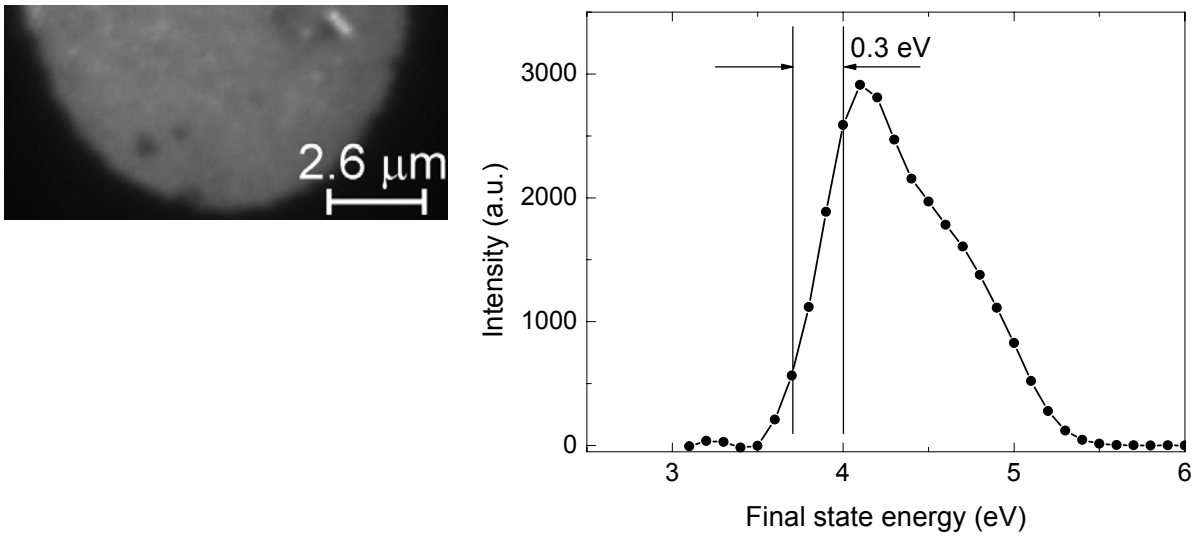

Figure 2.6: (a) Image of bulk silver under UV excitation (Hg lamp) recorded using the imaging energy filter with retardation energy of 0.7 eV in the second grid. The lateral resolution was 200 nm. PEEM parameters were the following: $U_{\text{extractor}}$=140 V, U_{Focus}=465 V, U_{Column}=$U_{\text{Projective1}}$=$U_{\text{Projective2}}$=U_{L1}=100V, U_{L2}=20V. (b) Spectrum of photoelectrons from bulk silver under UV excitation.

2.3 Set-up for the observation of current-induced emission

A schematic drawing of the experimental set-up for the observation of current-induced emission is shown in Fig. 2.7. The samples were placed in a conventional PEEM sample stage upgraded for the possibility to pass a current through the sample. The sample did not have an electrical contact with the sample holder.

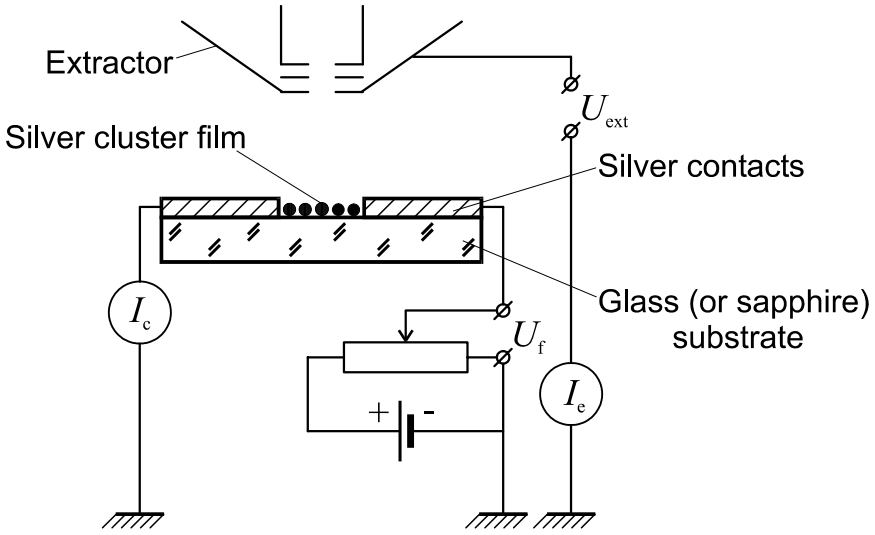

Figure 2.7: Schematic drawing of the experimental set-up for the study of current-carrying films. Explanations see text.

A positive potential of U_{ext}=500 volts was applied to the extractor in order to measure the emission current (I_e). The conduction current (I_c) was measured during the evaporation process that allowed to control the electrophysical properties of the samples.

While the electrical power fed into the silver cluster film during the experiment increases, irreversible changes of its structure may occur. This can be easily determined from a change of the conduction current-voltage characteristic. In this case the conduction current-voltage characteristic measured with decreasing voltage does not coincide with the curve measured before the increase of the voltage. If the maximum voltage was not exceeded, after a few cycles of the voltage application to the cluster film, its conduction current-voltage characteristic becomes reproducible. This testified that the cluster film structure was invariable. Moreover, to provide such invariability, all measurements of the current-voltage characteristics of conduction and electron emission currents as well as the measurements of the integral photon emission intensity as a function of the voltage were performed as the voltage decreased, i.e. from the maximum applied voltage down to zero. This ensured that the film structure did not change during the measurement of the electrophysical and emission properties of the cluster film.

2.4 Laser systems

The laser-systems used are commercial mode-locked Ti:sapphire lasers. Tsunami, Spectra Physics (Laser 1) and MaiTai, Spectra Physics (Laser 2) are pumped by about 7 W from a diode-pumped all-solid-state laser system and about 9W cw Ar+-laser, respectively

(see Fig. 2.8). We briefly describe the first laser system, located in the group of Prof. Aeschlimann at the TU Kaiserslautern. The parameters of both laser systems are collected in Table 2.1. The first system delivers transform-limited and $sech^2$ temporally shaped pulses of up to 6.25 nJ/pulse with a minimal pulse width (FWHM) of 18 fs and a repetition rate of 80 MHz. The wavelength can be tuned within a range of 740 to 830 nm (″red″ laser beam), corresponding to photon energies of 1.7 to 1.5 eV, respectively. The laser pulse width could be continuously varied up to values of 500 fs by detuning of the used dispersion compensator consisting of a pair of fused silica prisms. The linearly polarized output of the laser can be frequency doubled in a 0.2 mm thick Beta Barium Borate (BBO) crystal to produce ″blue″ laser pulses at $h\nu$=3 eV to 3.4 eV . The conversion rate of the BBO is about 20% giving pulse energies of up to 1.25 nJ. The ″blue″ beam is sent through a pair of fused silica prisms to pre-compensate for pulse broadening due to dispersive elements such as lenses, beam-splitters and the UHV-chamber window in the optical path. A group velocity dispersion and intensity loss matched interferometric auto-correlator set-up was used for the time-resolved (pump-probe) experiment. The pulses can be split by a beam-splitter to equal intensity (pump and probe pulses), and one path was temporally delayed with respect to the other by a computer-controlled optical delay stage. Before being directed into the UHV chamber both beams are combined collinearly by a second beam-splitter.

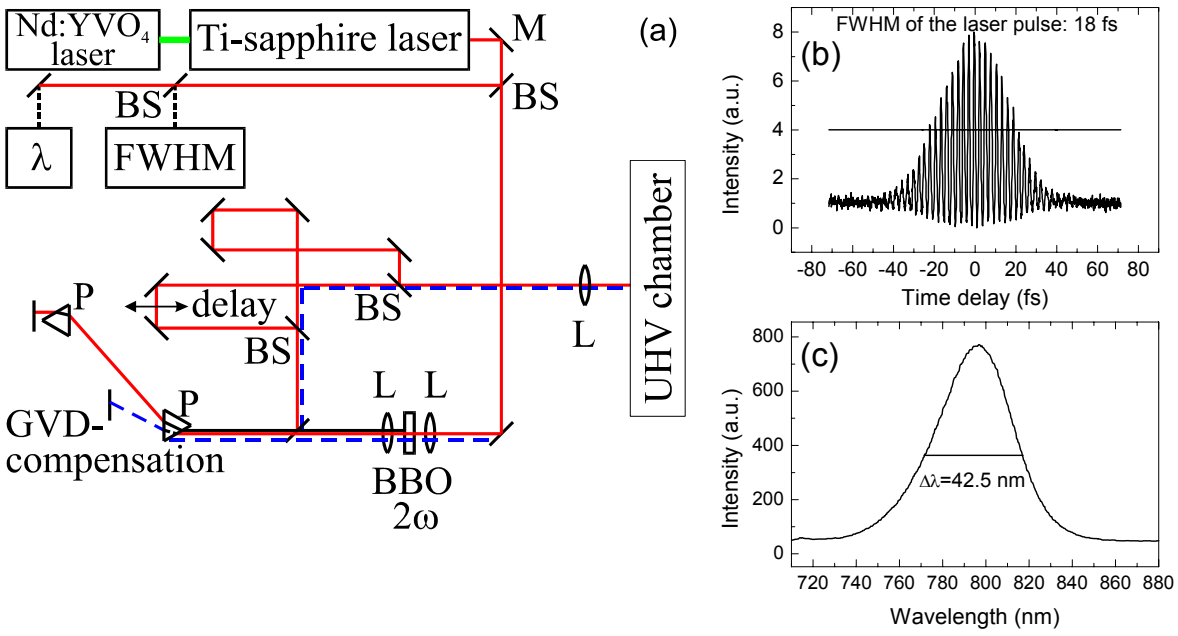

Figure 2.8: (a) Schematic view of the pump-probe laser setup used for the time-resolved photoemission experiments. L – a lens, M – a mirror, BS – a semi-transparent mirror (beam splitter), P – a prism, λ and FWHM – the devices for the measurements of the wavelength and the width of the laser pulse. (b) Autocorrelation trace and (c) spectral distribution of the red pulses of the first laser.

The second laser system is located in our group. It consists of a Ti:sapphire oscillator with a conventional frequency doubler. It was not used in a pump-probe mode.

	λ, nm	Mean power, mW	Pulse width, fs	Energy per pulse, nJ	Spot size, height x width, μm^2	Fluence per pulse, $\mu J/cm^{-2}$	Photons per pulse, $x10^9$	Photon flux per pulse, nm^{-2}
Laser 1 ″red″ beam	740-830	500	18	6.25	100x100	62.5	26	2.6
Laser 1 ″blue″ beam	370-415	100	28	1.25	100x100	12.5	2.5	0.25
Laser 2 ″red″ beam	750-850	700	100	8.75	100x200	43.7	35	1.75
Laser 2 ″blue″ beam	375-425	120	200	1.5	100x200	7.5	3	0.3

Table 2.1: The parameters of the two laser systems used in the photoemission experiments. Lasers 1 and 2 were used for the experiments shown in sections 3.2 and 3.3, respectively. The last column gives the number of photons per pulse per cross sectional area in the focus of the laser beam at the sample.

The photoemission studies of silver nanoparticle films were performed in two modes: normal emission mode and transmission mode. In the normal emission mode (see Fig. 2.2) the laser was focused on the sample at an angle φ (normally 65^o) with respect to the surface normal. A Fresnel rhomb could be used to rotate the polarization of the incoming light. For p-polarized light the electrical field vector E has a component perpendicular to the sample surface that is equal to $E \cdot \cos\varphi$, while for s-polarized light E lies in the plane of the sample surface. The extractor electrode (anode) and the excitation source are located on the same side of the sample.

In the transmission mode the anode and the excitation source are located at different sides of the sample. The photoelectrons were excited by illuminating the substrate from the back (outer) side normally to the sample surface. The electric vector of both s- and p-polarizations lies parallel to the sample surface. In this mode only thin films can be investigated because the penetration depth of the laser radiation is only several nanometers for the wavelengths used.

Chapter 3.
Results and discussion

3.1. Electrical and emission properties of current-carrying silver cluster films

3.1.1 Sample preparation

The silver cluster films were prepared and studied in UHV conditions. A glass (or sapphire) substrate with previously deposited silver contacts as shown in Fig. 3.1 was introduced into the preparation chamber.

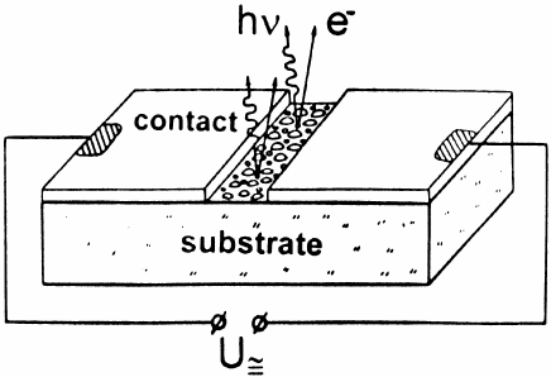

Figure 3.1: Schematic diagram of the sample with a silver island film between two contact electrodes.

These contacts had the thickness of 100 nm and a length of 2 mm. A shadow technique using wires with diameters of 25 and 5 μm was used to make a gap between the contacts. The substrate with contacts was cleaned by mild sputtering (Ar+, 1 keV, 5 min) prior to deposition. The silver cluster films were deposited using an electron beam evaporator. The rate of deposition was 0.03 nm/s. Since metals normally do not wet dielectric surfaces, the equilibrium growth mode corresponds in this case to the Volmer-Weber mechanism [Bau72]. Thus, if the mass thickness of the deposited film is small enough, the metal atoms coalesce during deposition or subsequent annealing into islands to minimize the surface and interface free energy.

During the deposition process a voltage of 1 V was applied to the contacts, and the conduction current was measured. Deposition was stopped when the surface resistivity (defined as the ratio of the DC voltage drop per unit length to the surface current per unit width for electric current flowing across a surface) reached the value of ~ 40 MΩ/sq. In this case the distance between clusters is approximately 1.5-2 nm [Bor65]. The average size of the clusters can be efficiently modified by changing the substrate temperature ant thus the mobility of the atoms. This size comprizes a few nanometers for room temperature deposition of Ag onto a glass substrate.

In order to obtain electron and photon emission from a cluster film using the conduction current excitation, it is first necessary to subject the film to an "electroforming" procedure

[Ble81]. The forming occurs when an increased voltage is applied to the as-deposited (high resistance) film.

The conduction current flow seems to induce the process of electromigration in the film facilitated by local Joule heating, which results in the formation of tunneling percolation paths (current channels) and, as a consequence, in a sharp and irreversible decrease of the film resistance [Ale88]. A current channel is a chain of clusters between contacts, which has a largest product of potential barrier transparencies.

The electroforming of a silver island film was done applying a voltage of up to 30 V for a time of ~3 min. It was interrupted when the resistance stopped to decrease. If a certain maximum voltage was not exceeded, then, after a few cycles of voltage application to the cluster film, its conduction current-voltage characteristic becomes reproducible. This is an indication that the cluster film structure is invariable. Moreover, to provide such invariability, all measurements of the current-voltage characteristics of conduction and electron emission currents as well as the measurements of the integral photon emission intensity as a function of applied voltage were performed as the voltage decreased, i.e. from the maximum applied voltage down to zero. This guaranteed that the film structure was not changed during the measurement of the electrophysical and emission properties of the silver cluster film.

The process of electromigration in cluster films is so far poorly investigated. Generally, the phenomenon of electromigration is rather complicated and highly sensitive to the chemical nature and the structure of systems under study. For example, electromigration in a number of bulk metals (Al, Ag, Au, In, Sn) and in their continuous thin films is driven by the scattering of electrons (″electron wind″), i.e. occurs towards the anode [Heu78, Agu98]. Films of the same metals being deposited on a semiconductor surface grow by the Stranski-Krastanov mechanism, i.e. they form a continuous monolayer with three-dimensional islands on it, and often exhibit electromigration towards the cathode (see e.g. review [Yas92]). Probably, the emission centers arise as a result of an interplay between the structure of the film and the processes of electro- and thermal migration. In particular, electromigration depends on the local current density and resistivity, depending in turn on the film structure. If a considerable enhancement of the current density appears in some place in the current channel, it can be anticipated that the electromigration, perhaps combined with somewhat enhanced Joule heating, causes a destruction (burning) of this segment of the channel. This results in a growth of the voltage drop across this segment at the expense of the potential drop across the remaining parts of the channel. This avalanche-like process appears as a kind of instability of the uniform potential distribution which, however, does not lead to a complete burning of the channel if the voltage applied to the film is not too high. The result is that only one emission center survives in a channel. Probably, at some stage of the process there occurs a stabilization of the film structure through a mechanism of self-limitation coming into play. This means that the film structure can be reconstructed when a large power is fed into it while at low powers the film structure remains unchanged. This is mirrored in the fact that electroformed films show practically stable conductivity and emission properties for thousands of hours under appropriate vacuum conditions. We stress this point, because it is just the segment in the current channel with a sharp potential drop across it that gives rise to the electron and light emission. The mechanisms of this effect were discussed in section 1.2.

3.1.2 Measurements of electron and photon emission versus applied voltage

Fig. 3.2a-f shows a series of EEM images of a silver cluster film in a 25 μm gap between the contacts at different applied voltages. The images are basically UV-PEEM images with

superimposed current-induced emission. The left contact was grounded. A positive voltage U_f of 0 (a), 5 (b), 15 (c), 40 (d), 50 (e) and 55 V (f) was applied to the right contact. The dashed line in Fig. 3.2a is drawn through the centre of the silver cluster film and is parallel to the contacts. When the voltage increases, the image of the silver cluster film widens, its contrast becomes more pronounced, and its character changes. Widening occurs as a result of a shift of the image of both contacts to the left, and the left contact shifts stronger. At U_f = 5 V the silver cluster film is visualized as two doubled alternating light and dark stripes parallel to the contacts (Fig. 3.2b). As the voltage increases (U_f = 15 V) the contrast between the light and dark regions of the stripe enhances stronger than in the case of the right one (Fig. 3.2c). Further increase of the voltage results in prevailing of the left band (Fig. 3.2d) and fading out of the contrast on the side of the right contact. This reflects the fact that PEEM-lenses were adjusted at U_f = 0 V i.e. to the potential of the left (grounded) contact.

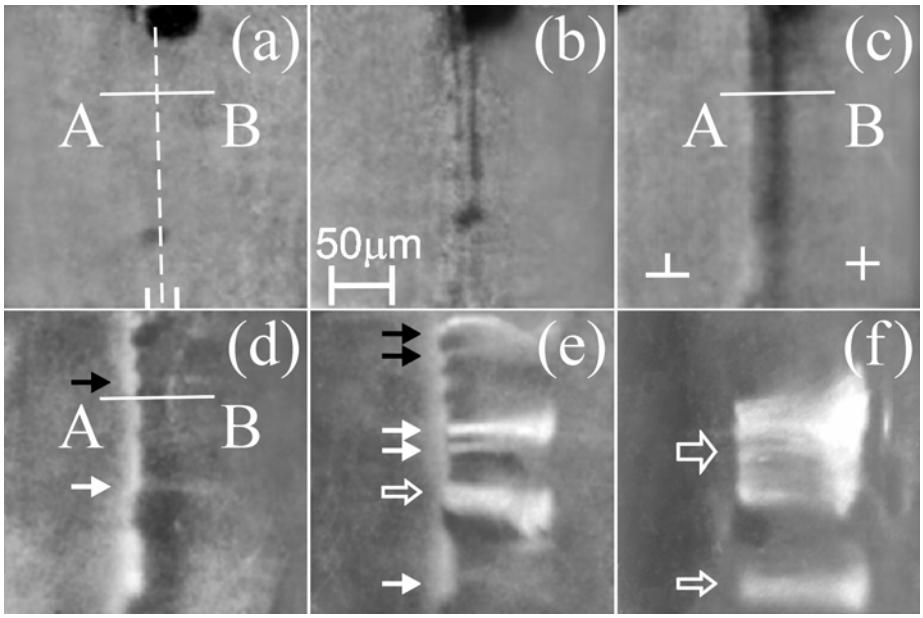

Figure 3.2: EEM-image series (UV-PEEM and superimposed current-induced emission) of a silver cluster film at voltages of U_f = 0 (a), 5 (b), 15 (c), 40 (d), 50 (e) and 55 V (f). The dashed line in (a) indicates the center of the 25µm wide silver cluster film deposited between two 100 nm thick electrodes (positions indicated at the bottom of (a)). Arrows indicate the electron emission centers (see text).

At the voltage of U_f = 40 V (Fig. 3.2d) the silver cluster film begins to eject electrons. In order to prove this, the UV-illumination of the silver cluster film was interrupted. Then the contribution of the photoelectrons to the image formation disappears, and only the contribution of current-induced electron emission by the silver cluster film remains (Fig. 3.3). It should be noted that pole switching leads to the similar emission pattern.

As is seen from Fig. 3.2d, the electron emission observed from the silver cluster film has a local character i.e. it arises from so-called emission centers. It is known that the emission centers are located within the current channels, mostly one center per channel [Ale87]. The location of the emission centers is actually unpredictable on substrates with flat surfaces prepared by ordinary methods such as mechanical polishing or cleavage. This is caused by the uncontrolled configuration of the current channels which reflects the statistical character of the nucleation of the islands. A typical emission center is a structure consisting of a relatively

large (≈100 nm) island surrounded by nano-sized islands [Fed00]. Such configurations are created in the course of electroforming. It is well known that in the process of Ostwald ripening of dispersed systems the large particles are growing at the expense of smaller ones due to the difference of the saturation vapour pressures over them. Thus, the emergence of local configurations of the type ″a large island + nano-islands around it″ should be quite probable, and such structures have indeed been documented in many studies on thin films (see [Had98] and references therein). However, as noted above, usually a single emission center appears within a current channel so the number of the centers in a film cannot be larger than the number of the channels in it. There is a depletion zone around the large island and due to this a considerable potential drop occurs at this place. The potential distribution in the film will be calculated in section 3.1.3 As will be shown in section 3.1.5, this plays an important role in the electron and photon emission from the film, since a substantial part of the power fed into the current channel is released within the center.

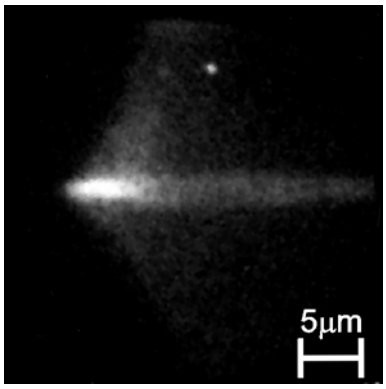

Figure 3.3: EEM image of a fragment of the cluster silver film at a voltage of 40 V. UV illumination is switched off.

In this section the studies of the emission characteristics from several emission centers are described. Along with this, it will be shown below how it is possible to vary the number of emission centers. If one purposely ″burns″ all of them, but one, by a slow increase of the applied voltage, it becomes possible to conduct measurements of the conduction and emission properties of a single, separate emission center. These experiments will be described in section 3.1.6

Two electron emission centers are visible in Fig. 3.2d (see arrows). The emission centre that was burnt as the voltage was increased to U_f = 50 V is marked with the black arrow and it is absent in Fig. 3.2e. In contrast, the emission centre, marked with the white arrow is strongly enhanced in Fig. 3.2e. Emission from this centre increases, however, it is possible that now electron emission stems from an extended region of the silver cluster film spreading around this emission center. The thick arrow with white border in Fig. 3.2e marks this region.

In the same manner, the black and white arrows are used to mark new emission centers in Fig. 3.2e. Two new emission centers (indicated by the black arrows in the upper part of Fig. 3.2e) irreversibly disappear if U_f increases from 50 to 55 V. These emission centers are absent in Fig. 3.2f. Three new emission centers marked with white arrows in Fig. 3.2e evolve when the voltage U_f increases from 50 to 55 V (Fig. 3.2f). The thick arrows with white border in Fig. 3.2f depict two broad areas of amplified electron emission from the cluster film.

At the increase of the voltage U_f from zero to 55 V, structure changes of the silver cluster film occurred. Structural changes were accompanied by irreversible changes of the electrical conductivity value (about 10 %). However, further variations of the voltage in the range of $0 \le U_f \le 55$ V showed reversibility of the current-voltage characteristics of the conduction and electron emission currents. The dependence of the integral photon emission intensity on the voltage applied to the silver cluster film was reversible as well. This means that after an initial electroforming of the cluster film its characteristics remained stable in this range. These experimental results are shown in Fig. 3.4 I_c, I_e and I_{ph} denote the conductivity current, the emitted electron current and the photon emission intensity, respectively. The latter is represented by the reading of the photomultiplier (in μA).

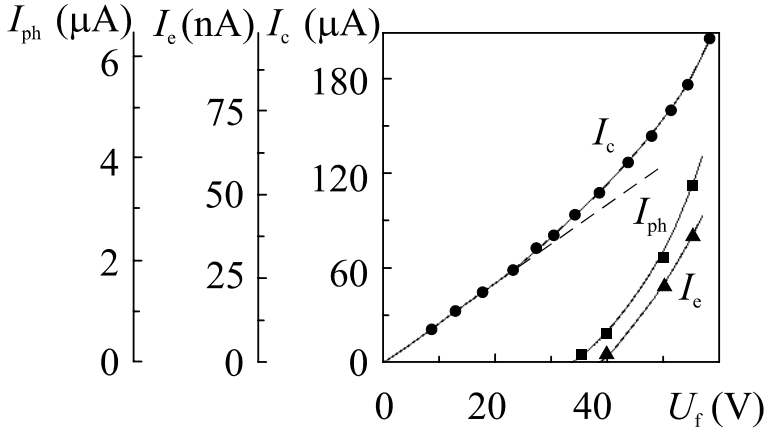

Figure 3.4: Current-voltage characteristics of the conductivity current I_c, the electron emission current I_e, and the dependence of the integral intensity of photon emission I_{ph} (reading of photomultiplier) on the voltage U_f applied across a silver cluster film.

Excellent correlation of electron and photon emission is evident. Along with this, the electron and photon emission was revealed to start from 40 and 35 V, respectively (see Fig. 3.4). The sensitivity of the photon emission measurement was higher than the sensitivity of the measurement of the electron emission current. The latter one could be increased using the microchannel plate of the emission electron microscope that amplifies the electron flux by several orders of magnitude. If necessary, the current on the microscope screen can be calibrated, thus giving access to absolute values of the electron emission current. At least, in the described measurements one emission centre was observed at an applied voltage of 35 V without illumination of the silver cluster film by the UV-lamp. Thus, the question whether the electron and photon emission from the silver cluster film has a threshold character or not, cannot be finally deduced from Fig. 3.4 because of the sensitivity of the methods used in our measurements. The figure indicates, however, that the electron and photon emission arise at about the same onset in the non-linear region of the current-voltage characteristic of conduction current (full circles). The beginning of the non-linear region is visualized by a deviation of the current-voltage characteristic of conductivity $I_c(U_f)$ from the dashed line being the continuation of its Ohmic region.

3.1.3 Determination of the potential distribution in the film

The performed measurements allow us to restore the electrical field (potential) distribution in the silver cluster film when a voltage is applied to it. This is illustrated for

two voltages: U_f = 15 (I) and 40 V (II). The intensity profiles $j(x)$ along line AB in Fig. 3.2a,c and d, shown by the solid curves (R), (I) and (II) in Fig. 3.5a, were taken as input for the calculations. The curve of photoemission current density distribution (intensity profile) at U_f = 0 V serves as reference (R). In the given case the intensity profile is close to a constant, and its value is taken as 1 arb. unit. At U_f = 15 V, the profile is deformed into a non-monotonous curve with several distinct minima and maxima (I). At U_f = 40 V, the silver cluster film just starts to eject electrons, (II). The x-axis runs from point A to point B. The length of line AB exceeds the linear dimensions of the area where the contrast caused by the silver cluster film changes if the voltage is applied. The analysis shows that the areas under the three solid curves in Fig. 3.5a are equal. It means that the number of photoelectrons, forming the image of the cluster film at different voltages, remains invariable. Variation of its image contrast is exclusively caused by a re-distribution of the photoelectron density due to deflections of their trajectories by the electrical microfields. For the measurements of Fig. 3.2 the contrast aperture was fully opened. The contrast formation for this case, i.e. without restriction of the electron beam demands to use the approaches and formulas from [Nep03]. The case with restriction of the electron beam by an aperture is considered in [Nep02].

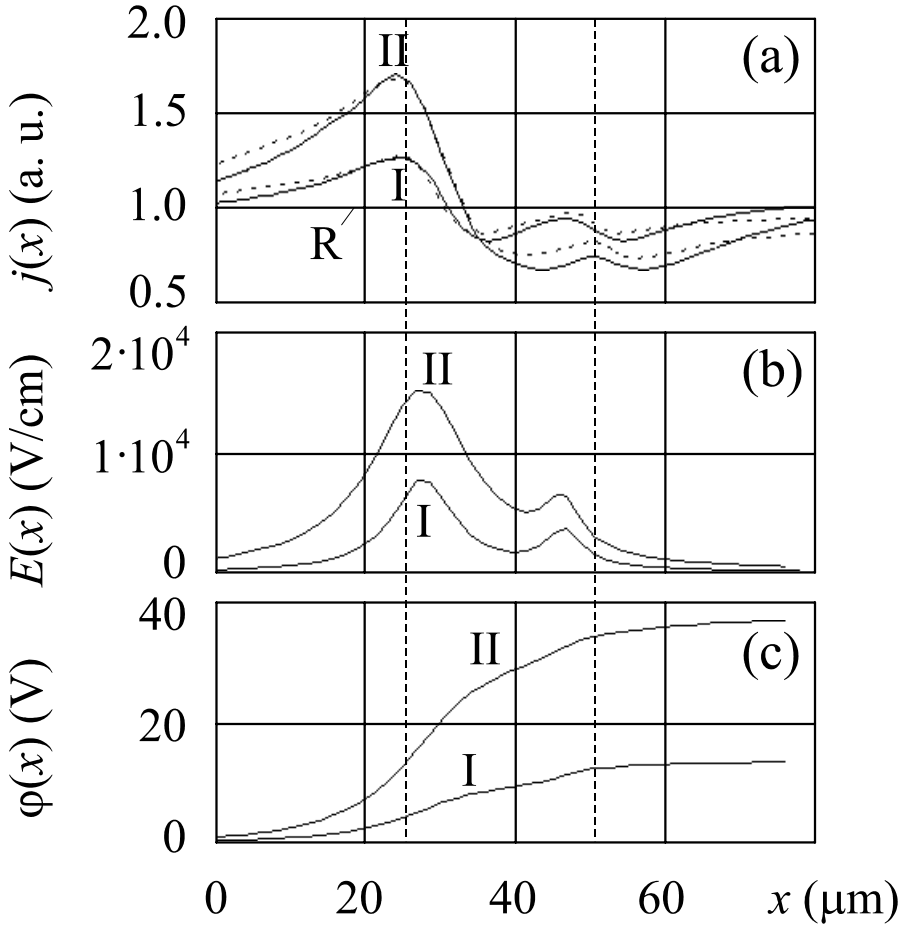

Figure 3.5: Intensity profiles along line AB in Fig. 3.2a,c and d (a), and corresponding curves of the electrical field (b) and potential (c) distribution. The voltage applied to the silver cluster film amounts to U_f = 15 (I) and 40 V (II). The intensity profile at U_f = 0 V served as reference (R). Theoretical curves of the distribution of photoemission current

density (intensity profiles) are shown by dashed curves (explanations and estimated uncertainty, see text). Vertical dashed lines denote the supposed position of the Ag cluster film.

In an emission electron microscope restriction of the electron rays deflected by microfields can be due to apertures or knife edges. And, conversely, the presence of an aperture not always means that the electron beam is restricted. In the case of weak microfields and large voltages applied to the microscope anode (extractor) the trajectory deflections are not large and all electrons from the sample can pass through an aperture of medium size and further through the projective optics to the screen.

Using the intensity profile curves $j(x)$ measured in the field-free case and in the cases when a voltage is applied to the cluster film as input in Eq. (5) in [Nep03], the function of a shift $S(x)$ of the image elements at the emission electron microscope screen is found. From the latter dependence and Eq. (4) in [Nep03], the potential distribution $\varphi(x)$ or electrical field distribution $E(x)$ in the cluster film is unambiguously reconstructed [Kra75] (*the so-called inverse problem*). Another possibility lies in the use of Eq. (3) in [Nep03] (*the direct problem*). In this case a distribution of the electrical field (or the potential) is chosen so that the initial curve of the intensity profile measured at $U_f = 0$ V is varied until the best fit is achieved with the measured intensity profile, at a given voltage.

It seems that *the inverse problem* should be always preferable. However this problem is ″ill-posed″ [Nep05]. In practice this manifests itself in the fact that the experimental curves of the current density profiles $j(x)$ are always measured with certain errors, and the curves of the electrical field $E(x)$ (or potential $\varphi(x)$) distribution calculated from $j(x)$ are characterized by several times larger errors. A dependence of the solution on the dimensions of the area where the profile $j(x)$ was measured is another disadvantage of this method. This area may considerably exceed the linear dimensions of the area of the local field concentration on the object area. In practical cases, however, the function of the current density distribution $j(x)$ can be reliably measured in a limited interval only. In such cases it is worthwhile to give preference to the solution of *the direct problem*. In our case we estimate the accuracy of the measurement of the current density distribution $j(x)$ as 10 %. Then we arrive at an inaccuracy in the determination of the potential distribution function $\varphi(x)$ of ≈ 30 %.

The results of the calculation of the electrical field distribution, obtained by the solution of *the inverse* and *direct problems* are quite similar. Fig. 3.5b shows curves (I) and (II) of the electrical field distribution $E(x)$ in the cluster film at voltages U_f = 15 and 40 V, respectively. The solution of *the direct problem* gives the intensity profiles $j(x)$ shown as dashed lines in Fig. 3.5a. In these measurements and calculations the following parameters were used: the accelerating voltage applied to the anode (extractor) U_{ext} = 4 kV, the distance between the cathode (object) and anode (extractor) l = 2 mm. As it can be seen, the dashed and solid curves are close to each other in both cases (I) and (II), i.e. quite good coincidence of the ″theoretically calculated″ (the *direct problem*) and experimentally measured curves of the intensity profiles $j(x)$ is evident.

In Fig. 3.5c the resulting curves (I) and (II) of the potential distribution $\varphi(x)$ in the silver cluster film at voltages U_f = 15 and 40 V, respectively, are shown. They are obtained by numerical integration of the corresponding curves $E(x)$ in Fig. 3.5b. As is seen from Fig. 3.5c, the voltage drops in two areas of the silver cluster film near the contacts. It is essentially larger in the left near-contact area. At U_f = 15 V the voltage drop in the left and

right near-contact areas equals 12 and 3 V, respectively. As the voltage increases to $U_f = 40$ V, the areas of the voltage drop remain the same, but nonuniformity of the voltage drop becomes more pronounced. Now in the left and right near-contact areas the voltage drop is 36 V and 4 V, respectively. This result allows us to conclude that the voltage drop (corresponding to the value of electrical field) in a given region of the cluster film is a non-linear function of the applied voltage. In the ideal case one can expect the field distribution similar to that of the plane capacitor, i.e. box- or bell-shaped.

This origin of the observed asymmetry can be explained by the difference in the structure of the central part of the silver cluster film and its near-contact areas [Bor76]. One of the factors determining this difference can be the deposition under the mask (a wire of 25 μm in diameter) when the contacts are made. It could happen if the point source of silver (silver evaporator) is situated not directly in front of the gap between the contacts. In this geometry silver atoms fly towards the substrate not perpendicular but at the certain angle that results in somewhat different film structure in the near contact areas. It should be mentioned that the diffusion length increases with the presence of the large objects in the vicinity of the cluster silver film, i.e. in the near contact areas. Also, the electromigration proceeds towards the cathode (see section 3.1.1), what results in further structural differences of the areas near contacts and in the middle of the film. Such a structural inhomogeneity results in a different local resistivity that is larger in the near contact areas. There is a depletion zone around the large islands which serve as the emission centers in the left near contact area and due to this a considerable potential drop occurs at this place. This is in accordance with the fact that the emission centers appear at the left contact.

3.1.4 Formation of the field contrast in an emission electron microscope

Formation of the field contrast in an emission electron microscope for the case of open contrast aperture (i.e. non-restricted electron beam) is described in [Nep03]. The contrast is caused by the redistribution of the current density of photoelectrons due to deflection of their trajectories by the microfields, which appear when a voltage is applied to part of the sample (in our case to the silver cluster film in section 3.1. It is rather unexpected (but at the first glance only) that photoelectrons and electrons, ejected from emission centers, are deflected to different sides. In reality, all of them are deflected towards the positive electrode. The scheme of Fig. 3.6 makes clear the different contribution to the total image shift and the apparent deflections to different sides. Here K is the plane of the real object (cathode), K′ is its virtual image plane arising due to the acceleration field. A is the plane of anode (extractor) that accelerates the electrons, E is the screen.

The increase of a positive voltage applied to the object leads to two effects: 1) the microfield increases and 2) the effective accelerating voltage changes. The first effect results in a deformation of the parabolic trajectory ″a″ on the way from the object to anode. The tangent to it ″b″ crosses the plane K′ at the distance S_1 from the optical axis. When no voltage is applied to the object, i.e. there are no microfields, $S_1 = 0$. The tangent to the parabolic trajectory, which is not deformed by the microfields (dotted line), corresponds to this case. The second effect leads to a shift of the virtual plane of cathode K′. Its new position is depicted by K′′. If a positive potential is applied to the object, or part of the object as in our case, the electron energy decreases, the focal length of the lens becomes shorter, and the plane K′′ is shifted to the right. Then the tangent ″b″ crosses the plane K′′ at the distance S_2 from the optical axis. S_1 and S_2 are located on different sides from the optical axis, i.e. they have different signs. Prevailing of one or the other effect depends on the value of the applied voltage. Thus, as the voltage applied to the object increases, the

apparent direction of shift is reversed. Let us note that the image of the left contact remains sharp because it is always grounded, thus the conditions of focusing are practically unchanged and the rim of the left contact remains well focused in Fig. 3.2c-f.

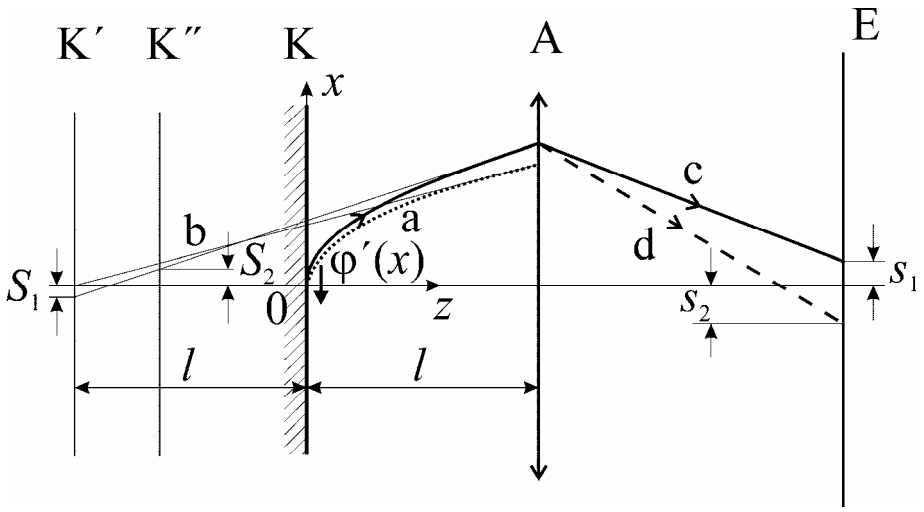

Figure 3.6: Scheme of the image formation in an emission electron microscope. E is the microscope screen, A is the anode plane (the focusing lens is drawn as thin lens at A), K is the real object plane (cathode), K′ is the plane of the virtual object image in the field-free case, K′′ is the plane of the virtual image of an object area, to which a voltage is applied (positive potential in this case). The shift S_1 is caused by the deformation of the parabolic trajectory due to the microfields on the object surface. The shift S_2 is caused by the displacement of the virtual image plane due to a change of the effective accelerating voltage when a voltage is applied to part of the sample. In the screen plane the corresponding shifts are s_1 and s_2, respectively. Other designations are explained in the text.

Under illumination with the UV-lamp, threshold photoemission from silver occurs, i.e. the image of the silver cluster film is formed by low-energy electrons. The spread of their energy is about 0.5 eV and thus can be neglected. An attempt to estimate the energy distribution of the electrons ejected by the emission centers by means of EEM will be presented in section 3.1.5. When the voltage is applied to the film, the slowly-moving electrons ejected by the emission centers are deflected by microfields towards the cathode. This effect becomes more pronounced when the extracting field strength (determined by the voltage applied to the extractor lens of the PEEM) is comparable with the strength of the microfield between the contacts. It should be noted that in the measurements shown in Fig. 3.2 the PEEM was operated in the so-called “low magnification mode” with U_{extr}=300 V. This explains the apparent cloud-like emission pattern and allows to localize the electron emission centers in the area of the silver cluster film which is adjacent to the left contact (Fig. 3.2d-f).

The emission center marked by the black arrow in Fig. 3.2d, is located in the immediate vicinity of line AB. The electrical field distribution $E(x)$ along this line is shown by the curve (II) in Fig. 3.5b. This allows the value of the electrical field near the marked emission center to be estimated. It amounts to $2 \cdot 10^4$ V/cm. Certainly, the electrical field on the emission center itself can be somewhat larger, but hardly by three orders of magnitude. This result is important because it rules out the possibility of the field emission mechanism due to the ″macroscopic″ field determined in Fig. 3.5. An electrical field of 10^7 V/cm is necessary

to realize this type of emission [Mül56]. Locally, however, such a field strength can occur (see next section).

The orientation of the deflection of the ejected electrons gives clear evidence that the electrical microfields in the area of the emission centers are directed perpendicular to the contacts of the silver cluster film. This behavior is anticipated for a homogeneous cluster film. The image of the beam of electrons, ejected by the upper emission center in Fig. 3.2e, shows that this is not always true. As is seen from Fig. 3.2e,f, the beam of electrons, ejected by emission centers becomes wider while moving away from the center towards the right. This effect is observed only at high voltages applied to the silver cluster film and disappears reversibly when the voltage decreases (compare Fig. 3.2e,f and Fig. 3.2d).

3.1.5 Investigation of the local electron emission

Fig. 3.7 shows an EEM image of another cluster film formed by both photoelectrons and spots that emit electrons under the same voltage of $U_f = 31$ V. All emission centers are located in the right near-contact area. This is most likely caused by the structural difference of the areas near contacts and in the middle of the film (see section 3.1.3). In this case the right electrode was grounded and a positive voltage was applied to the left contact. To resolve the single emitting centers we have to operate the PEEM in the ″high magnification mode″ i.e. the extractor lens voltage was much higher (>10 kV) that in the measurements shown in Fig. 3.2. In this case the microfields that appear in the sample plane when the voltage is applied to the film do not affect the trajectories of the emitted electrons. This explains the difference between Fig. 3.7 and Fig. 3.2d-f where the electron trajectories were strongly influenced by the microfields.

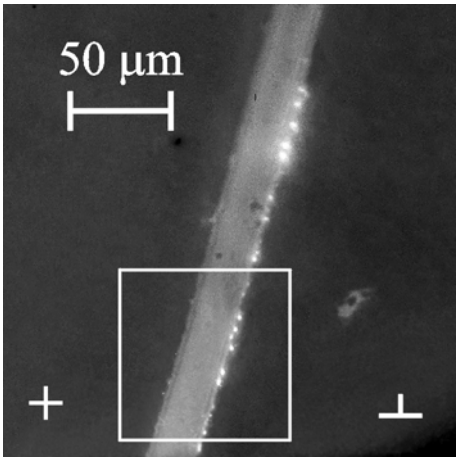

Figure 3.7: EEM image (UV-PEEM and current-induced emission) of a silver cluster film in the 25 µm gap between two contact electrodes at a voltage of $U_f = 31$ V applied across the film. Electron emission centers are visualized as spots and localized in the right (grounded) near-contact area. The positive voltage is applied to the left contact.

The region marked with a square in Fig. 3.7 is given at higher magnification in Fig. 3.8a. The image of the same region of the cluster film in Fig. 3.8b was obtained when the voltage was increased to $U_f = 32$ V. These images were reproducible. Reproducible images were ensured if the voltage across the film did not exceed the electroforming threshold

($U^* = 45$ V in this case). When the voltage was increased from 31 V to 32 V, the spots exhibit an intensity increase (the spot, marked with a black arrow is the only exception) and a shape deformation. In addition, new emission centers appear (corresponding spots are marked with white arrows). The behavior of the emission center, marked with a black arrow was of a special interest for us. The decrease of the electron emission intensity with the increase of the applied voltage was found to be reversible. A possible explanation is a Coulomb blockade. This phenomenon can occur if the emission center is located on a current channel or on the cross of several current channels. In the last case an enhanced current density through the emission center occurs. Coulomb blockade is originating from the creation of space charge on a current channel (one cluster or a group of clusters obtain a large negative charge) that leads to a current restriction or even to the full current being blocked through this current channel.

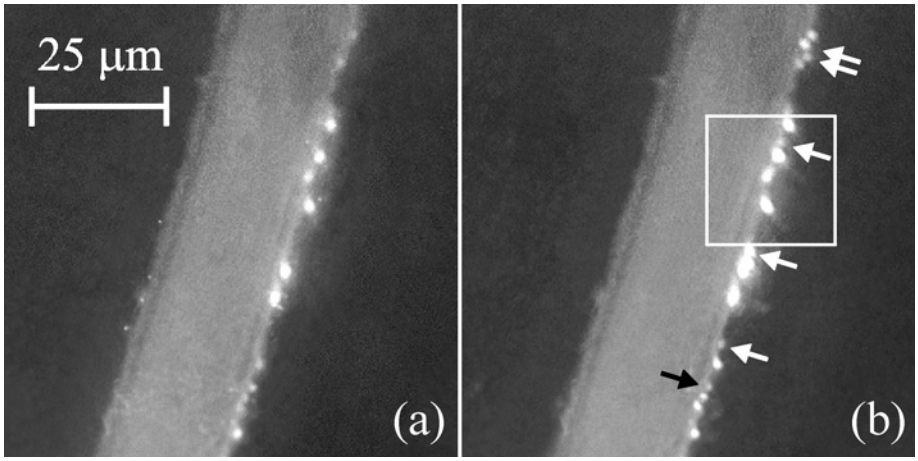

Figure 3.8: EEM images of the area, marked with a square in Fig. 3.7. A voltage of U_f = 31 V (a) and 32 V (b) is applied to the silver cluster film. When the voltage increases, the intensity of the spots increases (except the spot, marked with a black arrow) and new spots also appear (marked with white arrows).

The spot size visible on the microscope screen is determined by the angular and energy distribution of the emitted electrons. When the emission current density increases, an additional broadening of the energy distribution takes place due to the longitudinal Boersch effect [Boe54]. A significant impact of the electrostatic repulsion of emitted electrons sets in at current densities approaching 10^2 A/cm^2 [Luk36]. In our case, when the voltage on the cluster film was $U_f^* = 45$ V, the total emission current comprised approximately 10^2 nA, and the number of spots was about 30. Therefore the current emitted from a single spot reached a value of several nA. Let us point out that the use of an emission electron microscope allows us to determine the current value from a single spot. Let us assume a size of an individual emission center being equal to several tens of nanometers as an upper boundary (in the film under study all clusters were smaller than this value). Then it follows that the current density of emitted electrons can considerably exceed 10^2 A/cm^2. 3 nA from a r=20 nm particle corresponds to a current density of 240 A/cm^2. This estimation points to the importance of taking into account electrostatic electron repulsion.

The area marked with a square in Fig. 3.8b is shown in more detail in Fig. 3.9. The second spot from the top (it was absent at $U_f = 31$ V) has almost a round shape with an

apparent diameter of 0.7 μm. Note that the size of the emission center is almost 2 orders of magnitude smaller than the spot on the screen. It differs from the other spots (they were already present at U_f = 31 V) by intensity and shape. For example, the bottom spot has a size of the short and long axes of 2.1 and 3.7 μm, respectively. The higher the voltage applied to the cluster film, the larger the deformation of the spot shape (at U_f = 33 V a shape deformation of the second spot from the top also becomes visible). The reason for the strong increase of the apparent spot size as compared with the true emission centre is as follows. Electrons emitted by an emission center undergo an influence of the local electric field near to it, and also the influence of the ″macroscopic″ field between the contacts of the cluster film. The latter is directed perpendicular to the contacts. Since the current channels have a complicated non-predictable configuration and do not connect the two contacts in the shortest possible way, the local field at a given point can have an arbitrary direction. As the spots in Fig. 3.9 are elongated in different directions, one can conclude that the electrons emitted by an emission center retain a memory on the direction of the local field when they leave the surface.

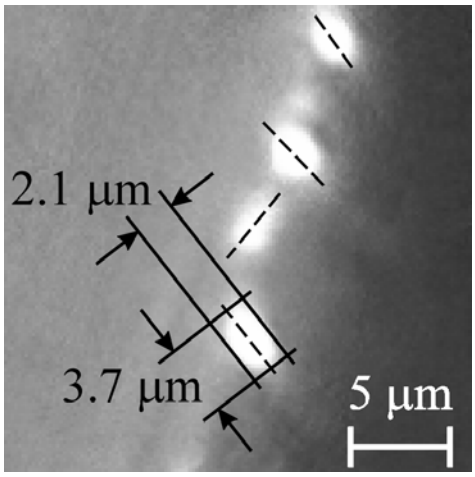

Figure 3.9: Detail EEM image of the area, marked with a square in Fig. 3.8b.

Since the emitted electrons are a sensitive probe for the emission centers, let us make several estimations. Describing the second spot from the top in Fig. 3.9 one can most likely neglect the influence of the electrostatic repulsion and the interaction with the local field. Then its linear dimensions D and the width of the energy distribution $\Delta\varepsilon$ of the electrons emitted in all directions are connected with each other by the formula

$$D = \frac{\Delta\varepsilon / e}{U_{ext} / l} \qquad (3.1)$$

where U_{ext} is the anode (extractor) voltage, l is the distance between the cathode (object) and anode, and e is the electron charge. In our case D = 1 μm, U_{ext} = 1 kV, l = 2 mm, yielding an energy distribution is not wider than $\Delta\varepsilon$ = 0.5 eV. We note that this is a crude estimation because it does not account properly for the potential distribution of the cluster surface.

If the spot has an elongated shape, one can estimate the value of the local field near the emission center. Let us consider for this purpose the first spot from the bottom in Fig. 3.9. It

has a rather pronounced elongated shape. The size of its short axis $D_s = 2.1$ µm is caused by two effects, i.e. the angular and energy distribution of emitted electrons and also the electrostatic repulsion of the electrons in the beam. It is equivalent to the model, where the electrostatic repulsion is absent and the effective energy distribution is $\Delta\varepsilon_s = eD_s U_{ext}/l = 1.05$ eV. The spot size along the long axis $D_l = 3.7$ µm is caused by three effects. The effect, connected with the local field is added to the two above mentioned contributions. The local field is directed along the long axis of the spot. In the framework of the model, where electrostatic repulsion of the electrons in the beam and their interaction with the local field are taken into account through their impact on the effective energy distribution, the latter is equal to $\Delta\varepsilon_l = eD_l U_{ext}/l = 1.85$ eV. Therefore, the influence of the local field on a beam of emitted electrons is equivalent to the situation where it passes a sector with a potential difference of $\Delta U \approx (\Delta\varepsilon_l - \Delta\varepsilon_s)/e \approx 0.8\,V$ (it is the value of the potential drop in the vicinity of the emission center). The higher boundary of the size of this sector b is comparable with the clusters size in the region containing the emission center (several tens of nanometers). The lower boundary of the size is the gap between the clusters, i.e. about 1 nm. Indeed the distance can not be larger than 2 nm (otherwise the tunneling is absent) and not much less than 1 nm (otherwise neighbouring clusters can coalesce, because their distance would approach the lattice constant). Then, the maximal value of the local field near an emission center is $E = \Delta U/b = 10^7$ V/cm by order of magnitude. This is a typical condition for tunnelling currents as used, e.g., in an STM. As it is the same mechanism of electron emission it is also in the range of field emission that needs a larger field value (of $> 10^7$ V/cm) [Mül56].

3.1.6 Investigation of electron emission at low voltages

The investigation of electron emission at low voltages close to the onset is very interesting. For these studies the structure of the silver cluster film is optimized to attain a very low onset. Along with it, the distances (gap) between the clusters are in the tunneling regime of the electroconductivity and are in a narrow range of 1-2 nm. The size of the clusters can be varied to some extent by changing the evaporation parameters (deposition rate and substrate temperature). Very simple and effective is the use of a very thin wire with 5 µm diameter instead of 25 µm for the preparation of the gap between the contacts. Then, the same fields in the cluster film are realized by voltages being 5 times lower. Also it is helpful to use an adsorbate, for example cesium, to reduce the work function.

In Fig. 3.10 we show a series of EEM images of a cesium-covered silver cluster film at different voltages between the contacts. The coverage of the cesium layer is less than a monolayer because the surface of the silver cluster film is much larger than that of a plane substrate surface. The right contact was grounded and a positive voltage U_f of 0 (a), 7 (b), 8 (c), 10 (d), 11 (e), and 14 V (f) was applied to the left electrode. Comparing the images taken at $U_f = 0$ V (Fig. 3.10a) and 7 V (b) one can see the contrast from the silver cluster film under applied voltage to appear as a doubled bright-dark stripe parallel to the contacts. When the voltage increases, the contrast becomes more pronounced and the gap between the contacts apparently widens. At $U_f = 8$ V (c) two centers of electron emission appear, the corresponding spots are marked with arrows. The intensity and apparent size of the upper spot is much higher than that of the lower one. A voltage increase up to $U_f = 10$ V (d) leads to an intensity increase of both spots, but now the lower spot has a higher intensity than the

upper one. The reason is a partial burning of the upper spot. At U_f = 11 V (e) it burns completely (it irreversibly disappears), but a new spot appears. The further development of the spots is shown for U_f = 14 V (f), where the pattern merges into a cloud-like shape.

The contrast formation is influenced by interaction of the emitted electrons with the microfields that arise in the silver cluster film when the voltage is applied to it. They are deflected towards the contact with a positive potential (to the left in this case). The electrons, emitted by the emission center, are also deflected to the left. Along with that, a shape deformation of the corresponding spots occurs. For example, the bottom spot in Fig. 3.10c has an almost circular shape, but when the voltage increases, it enlarges and elongates firstly to the left (d) and than finally to the right (e,f). This behavior is reversible and was explained in section 3.1.4 and Fig. 3.6. The image of the object in an emission electron microscope is only focused with certain accuracy. Let the initial image be overfocused (the distance between the virtual cathode and anode is > 2l). If a positive voltage is applied, then the position of the virtual cathode plane remains the same for the grounded electrode, whereas it shifts for the other electrode. When the positive voltage increases, the distance between virtual cathode and anode for this electrode decreases, passes the value of 2l (position of precise focusing) and becomes < 2l (underfocusing). Consequently, the visible direction of the deflections (cf. Fig. 3.6) of the emitted electrons on the screen of the microscope may change its sign during a continuous rise of the applied voltage.

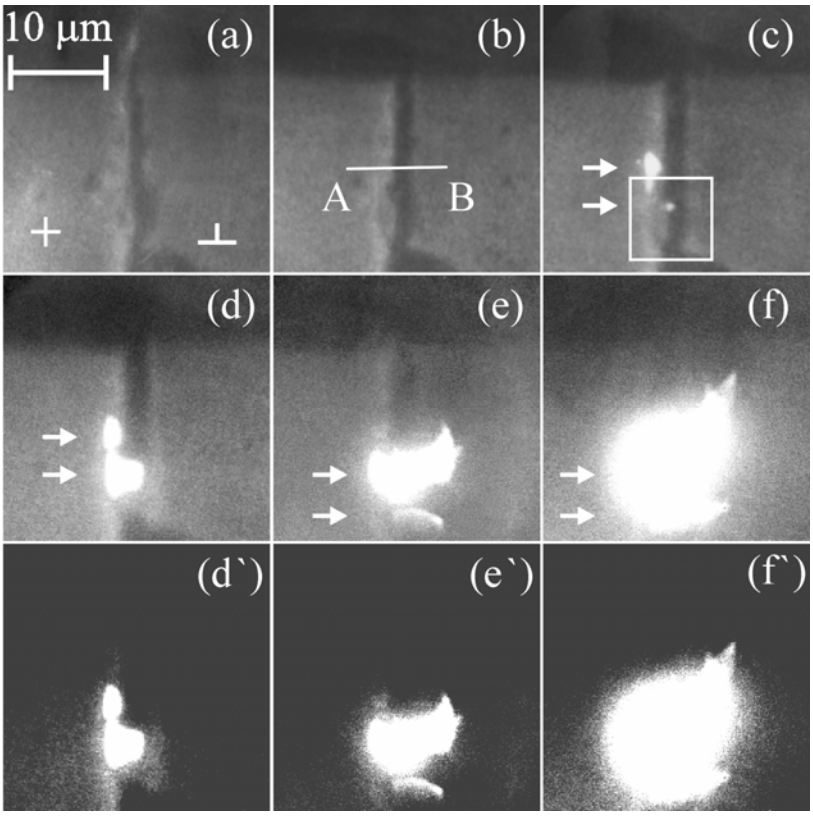

Figure 3.10: EEM (UV-PEEM and current-induced emission) image series of a silver cluster film covered with cesium in a 5 µm gap at voltages of U_f = 0 (a), 7 (b), 8 (c), 10 (d), 11 (e) and 14 V (f). The electrical field (potential) distribution was determined along line

AB. Arrows indicate the electron emission centers. The bottom row (d`, e`, f`) shows the same images as the second row but with darker contrast.

We measured a field (potential) distribution along line AB (denoted in Fig. 3.10b) at an applied voltage of 7 V. The photoemission intensity profiles along line AB in Fig. 3.10b,a are shown in Fig. 3.11a by solid and dashed lines, respectively. Using these intensity profile curves, the function of shift of the image elements was found (b). From the latter dependence and Eq. (4) from [Nep03] the electrical field distribution $E(x)$ (c) and potential distribution $\varphi(x)$ (d) were calculated. The method was described in more detail in section 3.1.3 . The difference is the following: the field in section 3.1.3 was determined along the line perpendicular to the electrodes and passing near an emission center. In this study, the electrical field distribution $E(x)$ was measured along line AB at U_f = 7 V (Fig. 3.10b), where the emission center appears after a further voltage increase by less than 1 V (c, upper spot). It obviously forms in the area of maximal electric field (voltage drop). As one can see from Fig. 3.11c the local field strength is $3 \cdot 10^4$ V/cm. The use of a wire with a diameter < 10 μm as a mask does not lead to silver deposition under the rim and, therefore, the silver cluster film is characterized by only one bell-shaped maximum of the electric field as expected for a flat capacitor.

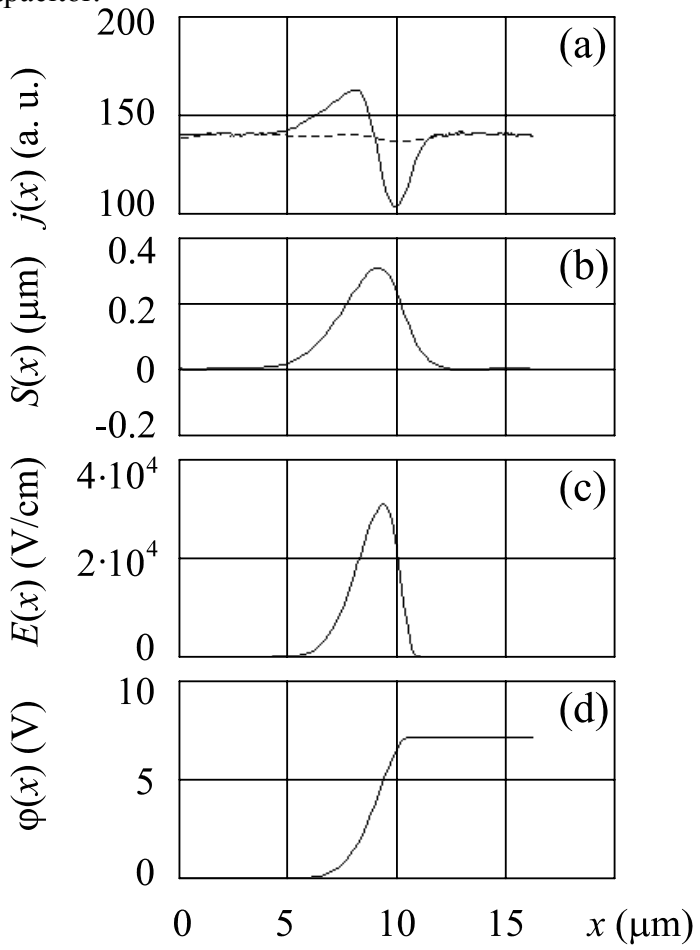

Figure 3.11: (a) The electron emission intensity profiles $j(x)$ along line AB in Fig. 3.10b at U_f = 7 V (full line) and without voltage (dashed line). (b) Image shift $S(x)$ resulting from

the intensity profiles. (c) Electric field distribution $E(x)$ and (d) potential distribution $\varphi(x)$, calculated using the image shift curve $S(x)$ and Eq. (4) from [Nep03].

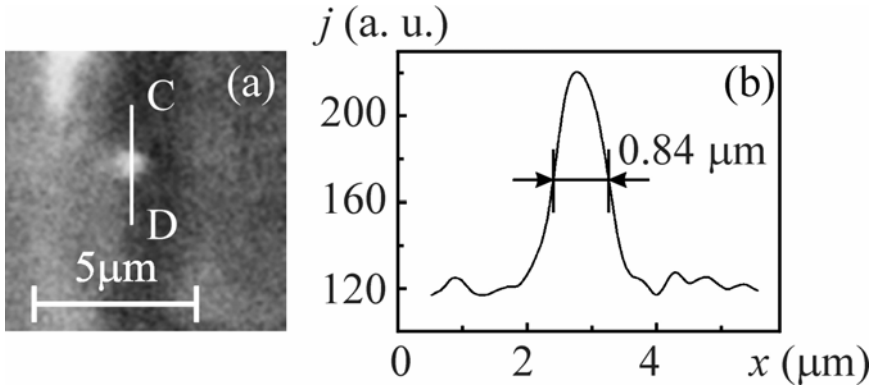

Figure 3.12: (a) Detail image of the area marked with a square in Fig. 3.10c and (b) intensity profile along line CD.

An approximate expression was used to estimate the energy spread of emitted electrons. Really, movement of the emitted electrons starting from a cluster takes place in a field that is the superposition of the local field around the cluster resulting from the (lateral) flow of tunnelling current and of the extractor field of the objective lens, being perpendicular to the film, see Fig. 3.13. Values of the field between the contacts (macrofield, Volts per μm) and the extractor field (kV per mm) are comparable. At the same time, the spatial extent of the macrofield normal to the surface is comparable with the value of the gap between the contacts, i.e. it reaches out far less (≈10 μm) than the extractor field (2 mm). Therefore, the contribution of the macrofield only leads to a small lateral displacement.

We also made an attempt to study the laterally resolved current-voltage characteristics of the silver cluster films. It should be mentioned that during the experiment we did not aim at a quantitative estimation of the dependence of the electron emission current from the single emitting centers on the applied voltage. There are two reasons that make these studies complicated: (i) the emission current grows exponentially with applied voltage and varies from several picoamperes to several hundred nanoamperes. This wide current interval is out of the linear range of the amplification unit (microchannel plate and fluorescent screen). Therefore, images taken at high electron emission currents sometimes appeared to be overexposed. (ii) The PEEM used to visualize the electron emission in this experiment was equipped with a non-ajustable 2mm contrast aperture. In this geometry one should apply an extremely high (>10 kV) voltage on the extractor lens to reach the resolution that is needed to resolve the single emitting centers. As the distance sample-extractor was approximately 2 mm sometimes sparking was spontaneously initiated between the sample and the extractor. Obviously this mostly destroyed the metal cluster film.

The best spatially-resolved series of electron emission images from the silver cluster film under different voltages is shown in Fig. 3.10. As the images (d)-(f) are slightly overexposed we take the apparent area of the emission center as a measure of the electron emission current. The result is plotted in Fig. 3.13. Comparing the obtained data with the integrally measured dependence that is shown in Fig. 3.4 we can conclude that both curves exhibit an exponential growth of the electron emission.

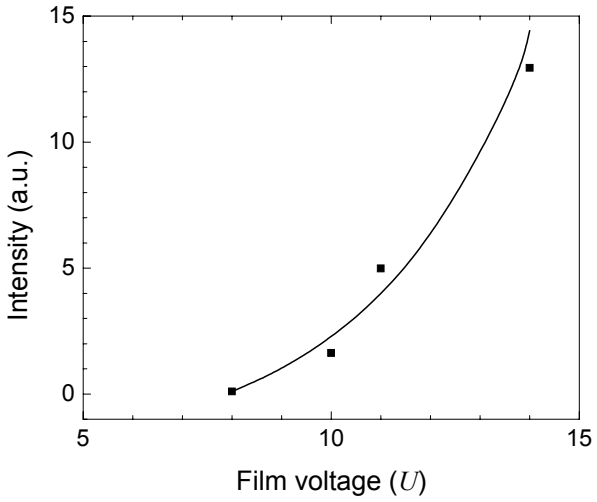

Figure 3.13: The local electron emission intensity versus the voltage applied across a silver cluster film. Data points were taken from the image series shown in Fig. 3.10c-f.

3.1.7 Discussion and conclusions

In section 3.1 we presented an investigation of the electrical and emission properties of silver cluster films that were carried out for the first time in an emission electron microscope. The following results have been obtained:

1. The conduction and emission characteristics of the silver cluster film as well as the electrical field (potential) distribution in the film were measured. The conduction current-voltage curve is initially linear, but it rises stronger than linear above a certain voltage onset. Within the accuracy of the performed measurements, the onset of electron and photon emission from the cluster film coincided with the onset of the non-linear region of the conductivity curve.

2. The electron emission originates from distinct emission centers. They are formed at certain individual voltage thresholds in the region of the largest electrical field in the silver cluster film. The apparent sizes of the emission centers were initially about 0.8μm and increased to several μm upon further increase of the applied voltage.

3. Though normally the metal cluster film ejects electrons from many emission centers under the passage of a current, its study in an emission electron microscope has a local character, which enables a single emission center to be investigated. To ensure the stability of these measurements the EEM should be operated in the high magnification mode. Moderate vacuum conditions (base pressure better than $2 \cdot 10^{-10}$ mbar) have to be maintained in the main chamber.

The EEM investigations have shown that the emission centers in a current-carrying silver cluster film are point sources of electrons that can provide very high emission current densities (up to more than 10^2 A/cm^2). It can be interesting for applications where the absolute value of the current is not important, but its high local density. The increase of the current density is restricted by physical principles (electrostatic repulsion of the electrons in a beam – Boersch effect). The energy spread of the electrons from a single emission center (the width of its most intense part) was estimated to be 0.5-0.6 eV.

We propose the following emission mechanism:

As the electron emission starts at the onset of the deviation from Ohmic behavior it is clearly connected with the tunnelling conductance. There, new current paths are opened that were absent in the Ohmic regime at lower voltages, see Fig. 3.14. The detail in Fig. 3.14 (bottom) shows the local behavior. The current I_{in} arises from tunneling through a barrier, whereas the current I_{out} runs through Ohmic contact(s) with neighboring particles. We assume a tunneling voltage of the order of 1V although it could in some cases even be several volts. Then, each tunneling electron carries an excess energy of 1eV or more into the nanoparticle. This electron is thermalized first with the electron system in the particle on a time scale of few fs and later with the lattice of the particle on a time scale of 1ps (for details, see section 3.2). Finally, the energy is dissipated by heat conduction into the substrate. We propose another energy dissipation channel that is thermionic emission from the steady-state ″hot″ electron gas in the particle. Hence, charge conservation demands $I_{in}=I_{out}+I_e$.

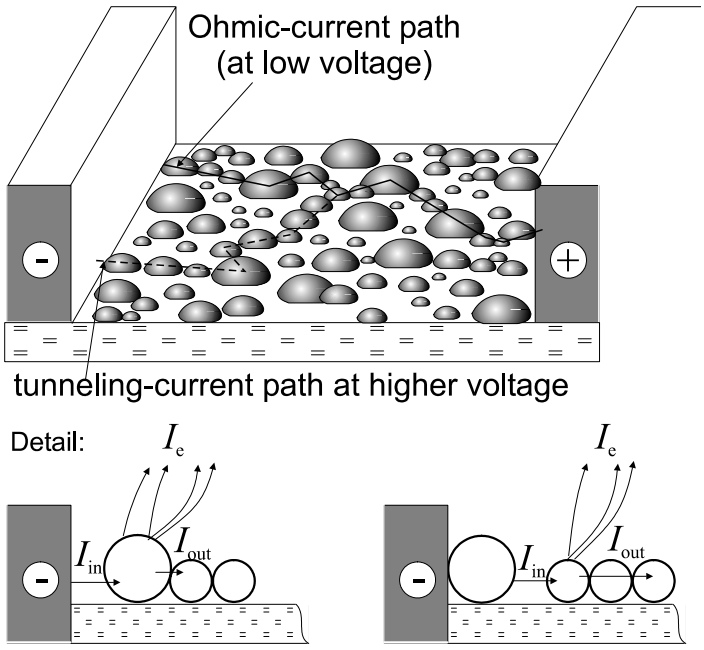

Figure 3.14: Proposed mechanism of electron emission induced by current passage through a granular film.

The emission current causes a considerable energy drain from the particle because every emitted electron has to surmount the surface barrier. It thus ″carries away″ about 4.5 eV of energy, corresponding to the work function of the particle. In other words, this can be considered as a ″cooling″ mechanism.

From the present experiments we cannot estimate the lattice temperature in the steady-state. As some of the tunneling paths are ″blown″ at certain voltages it is clear that the lattice temperature can rise most likely to the melting point. Before being blown the lattice temperature will also reach high values sufficient for ″normal″ thermionic emission. The energy drain by electron emission can have a regulating effect in a certain parameter range.

In the case of high voltages, corresponding to high currents (like in Fig. 3.2f or 3.10f), also Ohmic heating along a current path could come into play. In principle, larger areas of the cluster film can start thermionic electron emission. This phenomenon is finally

discontinued by ″burning″ of part of the current path, comparable to a fuse. Again the energy drain of the clusters by the leaving ″hot″ electrons may have a stabilizing effect.

The question whether the emission mechanism is true thermionic emission (thermal equilibrium of electron gas and lattice) or ″hot″ electron emission can not be unambiguously decided from these experiments. Therefore, another method has been applied utilizing the fs-laser as an excitation source.

3.2 Emission properties of metal cluster films under femtosecond laser excitation

3.2.1 Electron yield spectroscopy of Ag and Au nanoparticle films excited by ultrashort fs-laser pulses

In this section we present the results of studies of electron emission from nanoparticle Ag and Au films grown on a glass substrate excited by fs-laser radiation. The measurements were integrated over a microspot of about 100 μm diameter. Particle films with particle sizes ranging from the sub-nanometer range to a continuous film have been studied using the Laser 1 set-up described in section 2.4 (Fig. 2.8) providing fs-laser pulses with photon energies of 1.55 and 3.1 eV and with the radiation of a UV-lamp (photon energy ≤ 5.2 eV, see Fig. 2.1). It has been demonstrated that the dependence of the photoemission current on the mass thickness of the Ag film is non-monotonous. The transition from a continuous film to a nanoparticle film is accompanied by an increase in photoemission current by more than an order of magnitude. The dependence of the photoemission current on the power of the photon pulse is characterized by a saturation behavior. At fixed pulse power, the photoemission is more intense if the laser pulse is shorter. Pump-and-probe experiments with variable delay gave information on the lifetime of intermediate states. Experimental results are interpreted in terms of two electron emission mechanisms, i.e. multiphoton photoemission and thermionic emission or thermally-assisted multiphoton photoemission. The first mechanism prevails for continuous films and particles with sizes above several ten nanometers, the second one for films of nanoparticles with sizes of a few nanometers.

3.2.1.1 Sample preparation and characterization

Silver films with a wedge-shaped thickness profile have been prepared on a glass substrate. The substrate was manufactured from Uviol-glass that is transparent in the visible and ultraviolet range. It had a round shape, with a diameter of D = 36 mm. It served as a window in a glass vacuum device, see. Fig. 3.15a. The device was pumped by a sublimation pump reaching a base vacuum of $1 \cdot 10^{-8}$ mbar. An Ag film was prepared immediately before the measurements by using a thermal evaporator. It was placed at a distance of h = 7.5 mm from the substrate and close to its edge. As a result, the distance from the evaporator to different areas of the substrate varied from h to $l = \sqrt{h^2 + D^2}$. This geometry of the experiment allowed us to obtain a metal film, along which the mass thickness varied by a factor of 100. The evaporation rate at the region of maximum thickness was approximately equal to 0.03 nm/sec. The substrate was kept at room temperature. The particle sizes were measured after finishing the emission measurements by means of an atomic force microscope (AFM, type SIS) and a high-resolution transmission electron microscope (HRTEM, type Hitachi-8100). For characterization of the Ag films with the second method, 9 copper transmission electron microscopy (TEM) grids of 3 mm in diameter covered with a

continuous amorphous carbon film ~10 nm thick were attached to the substrate along the direction of the mass thickness gradient, see Fig. 3.15a. The grids were characterized by a sufficient mechanical strength and transparency for the electrons used in the HRTEM with 200 keV beam energy. HRTEM and AFM in combination provided a lateral resolution of 0.12 nm and a resolution in the direction perpendicular to the substrate surface of a hundredth of a nanometer, respectively. Gold films were prepared in a second similar device.

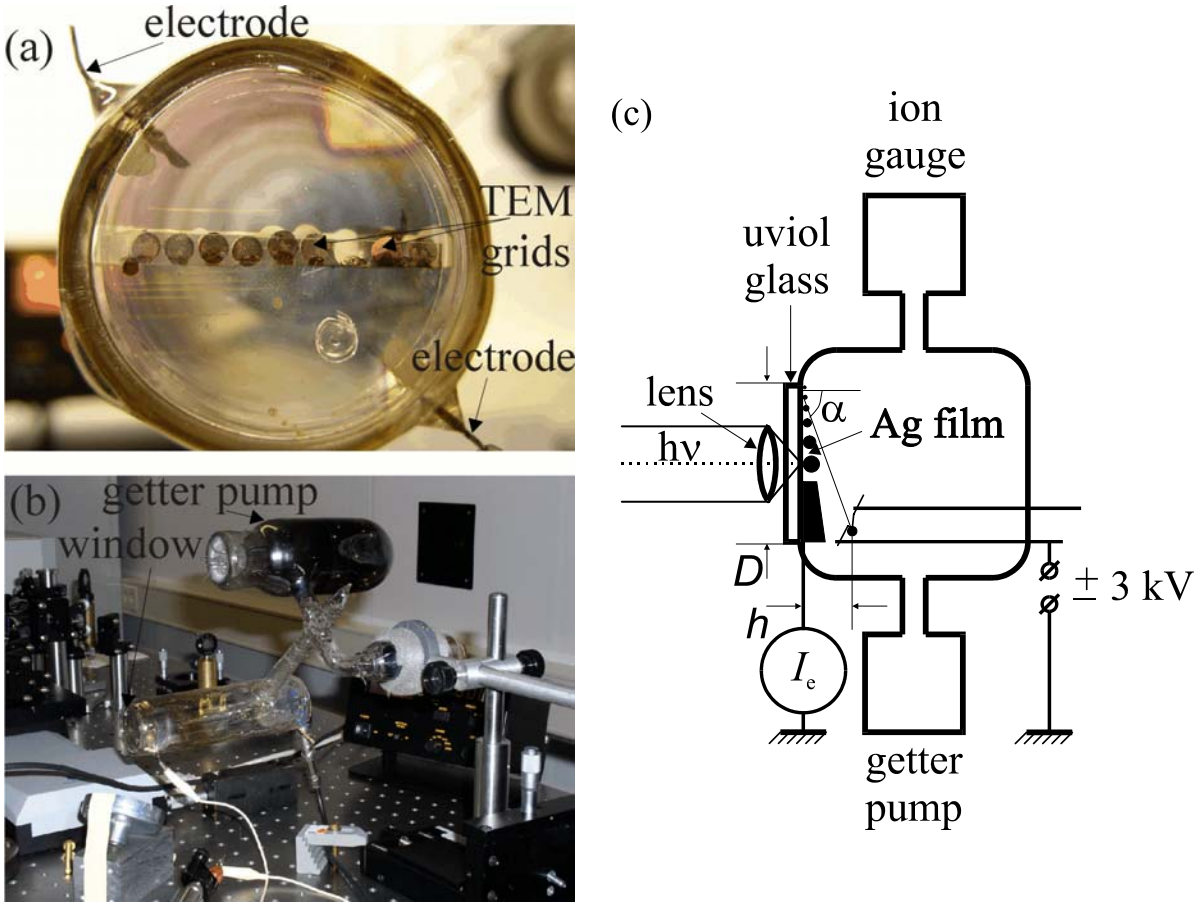

Figure 3.15: Photograph (a, b) and schematic view (c) of the device for the integral yield spectroscopy studies of Ag and Au films. D is the diameter of the window, *h* is the distance from its inner face to the evaporator, α is the angle between the direction to the evaporator and the surface normal of the silver film plane.

After preparation of the film, the evaporator was used as a collector of the emitted electrons. For this purpose, a potential of +3 kV was applied to it. It was sufficient to ensure the saturation mode at which all photoelectrons emitted from any, even the most distant areas of the wedge-shaped Ag and Au films, reach the collector. The rim of the window was coated with a thin ring of conducting glue to ensure an electrical contact between the film and the electrode. For measurements of the emission current, the sample (Ag and Au film) was grounded, and the incident beam was focused on it. The diameter of the illuminated area (100 μm) remained unchanged for different modes of excitation because in all the cases the same focusing optics was used. The photon beam was kept fixed and scanning was achieved by means of precision mechanical movement of the whole glass device containing

the sample, see Fig. 3.15b. The photoelectrons were excited by illuminating the substrate from the back (outer) side. The spot of the illuminating radiation was scanned along the Ag film in the direction of its mass thickness gradient. Repeatability of the experimental results was checked several times. This indicates that the structure of the Ag and Au films being studied remained unchanged at different modes of excitation.

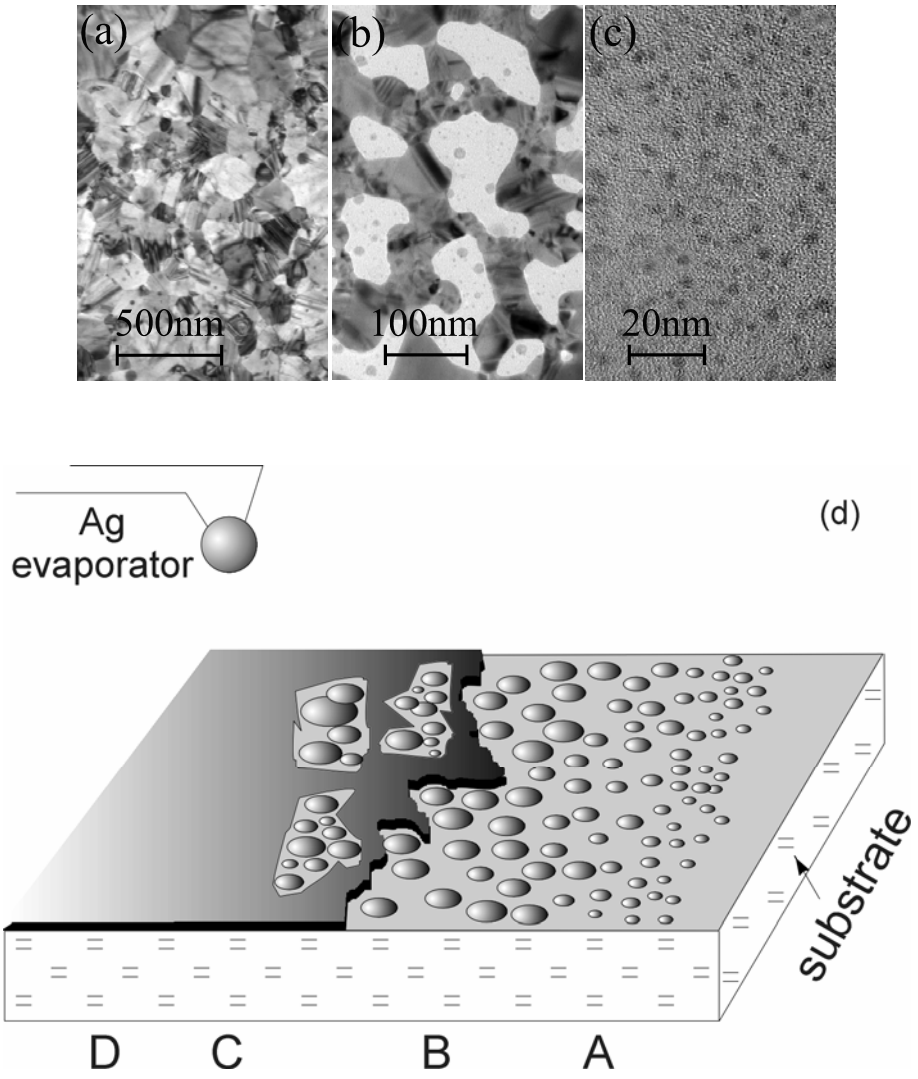

Figure 3.16: TEM images of Ag films on 10nm carbon foil with mass thicknesses of 33 (a), 2.5 (b) and 0.6 nm (c). Schematic view (d) of the film, defining areas A (isolated clusters of few nm size closed film), B (isolated clusters with a size up to several tens of nm), C (percolated film with nanoparticles) and D (closed film).

The structures of the Ag films obtained by means of HRTEM are shown in Fig. 3.16a-c. As is seen from (a), the Ag film with a mass thickness of 33 nm is polycrystalline and continuous (i.e. closed). With decrease of the mass thickness, gaps appear in the continuous film. Further decrease of the mass thickness leads to an increase of the gaps so that separate Ag particles are observed on the bare substrate in gaps of the percolated film. At a mass thickness of 2.5 nm the typical lateral size of the particles within the gaps is 10 nm (b). Ag films of still smaller mass thickness consist of isolated particles only (c). Along with

HRTEM characterizing the lateral dimensions well, AFM was used for precision measurements of the structure of the Ag film in the direction perpendicular to the substrate. The HRTEM and AFM measurements allowed a precise determination of the mass thickness d_{eff} of the Ag films as given in the examples in Fig. 3.16a-c. These values correlate well with the dependence $d_{\text{eff}} \propto l^{-2} \cos\alpha$, where l is the distance from the film to the evaporator and α is the angle between the direction to the evaporator and the surface normal of the film plane.

With increasing mass thickness we find isolated small clusters of few nm size (regime A), clusters with gradually growing size up to several tens of nm (B), partly coalescence of the clusters (C) and finally a closed Ag film (D).

Systematic structural investigations allowed us to characterize the thickness dependence of the coefficient of the substrate coating, the particles' average sizes and the distances between them. They also provide information about the work function. Fig. 3.17 illustrates particles in the gaps of the Ag film shown in Fig. 3.16b in more detail. These particles are visible as faint dark spots in the bright areas. The particle analyzed in Fig. 3.17 is a decahedron. Its fifth order symmetry axis is normal to the image plane and passes through the point in which the twinned boundaries converge (they are marked with white lines). Note that a fivefold symmetry is prohibited for bulk metal. In the image of this particle the atomic planes of (111) orientation being parallel to the twinned boundaries are visualized. The distance between them is a_{111} = 0.236 nm. Formation of multiple twinned particles is a characteristic feature of materials with f.c.c. lattice. In fact, it is possible to cut a tetrahedron out of the f.c.c. lattice by using four planes of the (111) type. All of its outer facets are close-packed, i.e. (111)-oriented, too. At the same time, it is known that the more closely-packed the facet, the higher its work function, and the lower the surface energy. Five tetrahedrons with a common edge form a decahedron and 20 tetrahedrons with a common edge form an icosahedron. The shape of such particles is close to spherical, and they are formed from facets with the smallest surface energy, i.e. their total surface energy is minimal. On the other hand, the smaller the particle size, the more essential is the surface effect. The minimum of the particles' free energy is achieved for minimum surface energy. The multiple twinned particles satisfy these requirements. Their formation is typical in case of a weak interaction with the substrate. Faceting of the multiple twinned particles determines their work function. It is known that the electronic work function is 4.52, 4.64, and 4.74 eV for facets of a clean Ag monocrystal of (110), (100), and (111) orientation, respectively [Dwe73, Dwe75]. Hence we conclude that the work function of relatively large Ag particles like that in Fig. 3.17 (decahedron with a lateral size of about 20 nm) is close to 4.74 eV, as long as the surface is clean.

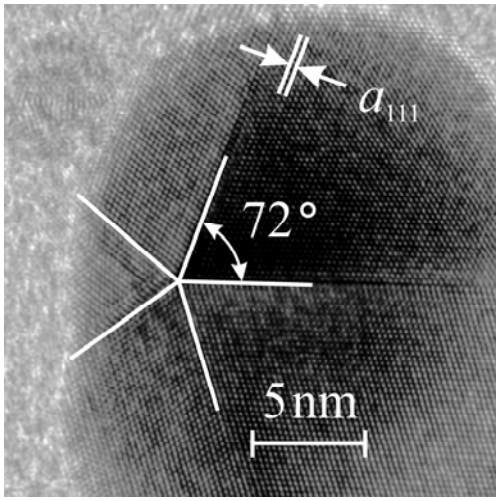

Figure 3.17: (a) HRTEM image of Ag particles located in a gap between continuous islands of the Ag film with a mass thickness of 2.5 nm: decahedral particle with 20 nm diameter with resolved fringes of atomic planes of (111)-orientation and icosahedral particle with 5 nm diameter in the upper left corner.

Another dodecahedral particle with a diameter of 5 nm is shown in the upper left corner of Fig. 3.18 (mass thickness 0.6 nm). Its diffraction pattern (Fourier transform) shown in the inset in Fig. 3.18 shows five sets of (111)-type reflexes (fivefold symmetry is prohibited for bulk metal). This particle is faceted by closely packed surfaces of the (111) type, too. However, due to the size dependence of the work function [Woo81, Kat87] the latter is smaller than 4.74 eV. It can be explained by the decrease of the mirror charge potential for a neutral metal sphere with radius r by the value of $\frac{5}{8}\frac{e^2}{r} = \frac{0.90}{r[nm]}eV$. This work function reduction is considerable in the size range of r=2-15 nm. For still lower sizes the work function increases again due to quantum-size effects approaching the value of the ionization potential of a single atom [Hee93].

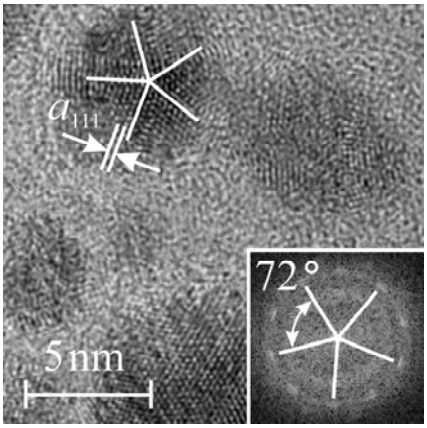

Figure 3.18: HRTEM image of the Ag particle film with a mass thickness of 0.6 nm. The Fourier transform of the image of the decahedral particle in the upper left corner is given in the inset. It contains 10 reflexes of the 111 type illustrating the fivefold symmetry of the multiple-twinned particle.

Ag films with a mass thickness of d_{eff} < 1.5-2 nm contain only insulated nanoparticles (a percolation is not observed). Histograms of the particle size distribution for Ag films with mass thicknesses of 1.2 and 0.6 nm are shown in Fig. 3.19a and (b), respectively. The histograms have been determined by evaluating areas of 15000 nm^2 and 7200 nm^2 with a total number of about 310 and 560 particles, respectively. The clusters were assumed to have a spherical shape. A good correlation is observed with the particle size distribution presented in section 3.2.2 for Ag on Si.

We recognize that the 0.6nm distribution (b) is rather narrow, centering at a diameter of 4 nm with a FWHM of about 2.5 nm only. There are no particles with sizes > 8 nm The 1.2 nm distribution (a) centers only slighter higher (at 5.5 nm diameter) but is much wider (about 6.5 nm FWHM) and extends up to diameters of 15 nm. This result is important in the context of size-selective excitations, see below.

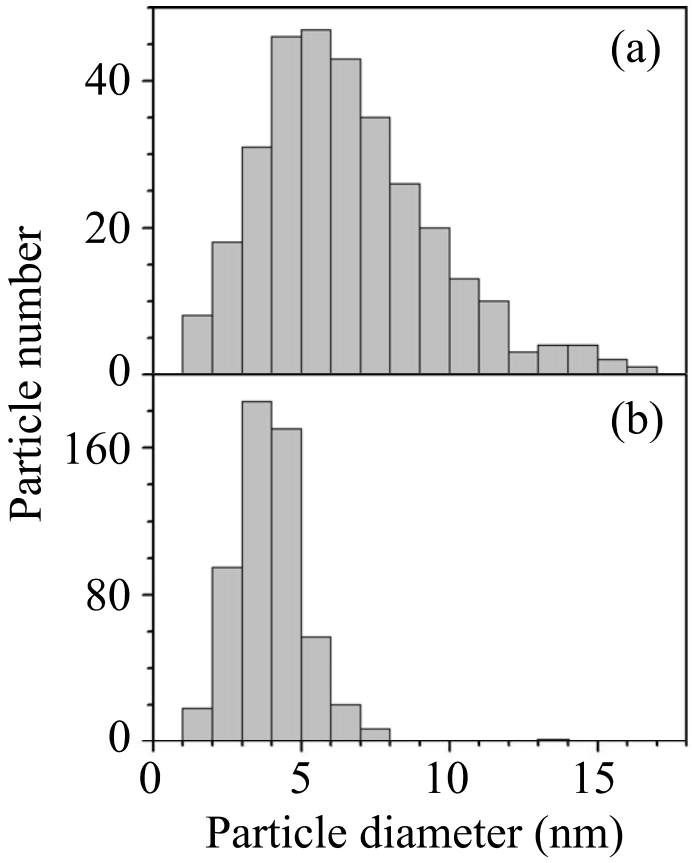

Figure 3.19: Histograms of particle size distributions for Ag films with mass thicknesses of 1.2 (a) and 0.6 nm (b).

3.2.1.2 Results

Dependence on the mass thickness

The experimental dependences of the electron emission current versus mass thickness for excitation with the 800 nm (b) and 400 nm (c) laser beam are given in Fig. 3.20. For the measurement the average powers of the "red" and "blue" laser beams differed and were equal to 500 mW and 100 mW, respectively, corresponding to fluences of 80 mJ/cm^{-2} and 16 mJ/cm^{-2} per pulse, respectively. The laser pulse duration was 18 fs and 28 fs in the first and second cases, respectively. Due to these short pulse lengths the photon energy

bandwidths are rather large, i.e. 1.55 ± 0.07 eV and 3.1 ± 0.15 eV, respectively. The latter interval covers the central range of the particle plasmon resonance spectrum of Ag. The maximum thickness of the studied Ag films was 33 nm. The penetration depth of the 800 nm, 400nm and 240 nm radiation is about 10 nm, 15 nm and 16 nm, respectively. This makes it possible to measure the photoemission current of the Ag film in the transmission mode, i.e. from the direction opposite to its illumination.

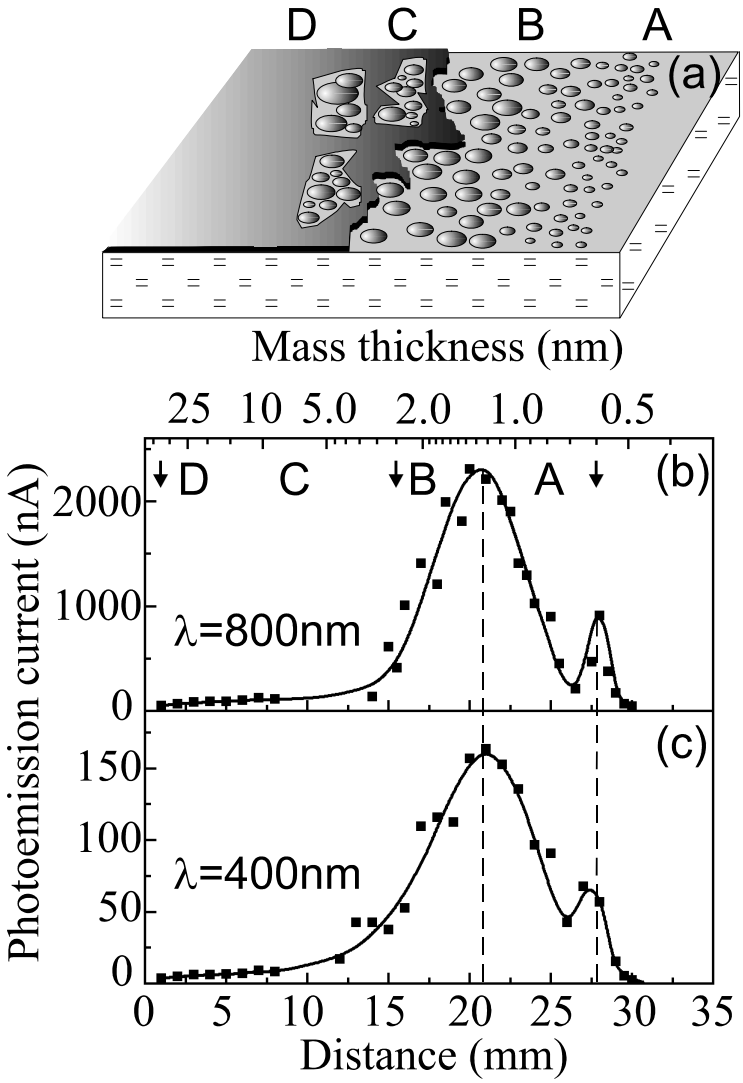

Figure 3.20: Electron emission current from a Ag film with wedge-shaped thickness profile. The distance from the edge of the film and corresponding mass thickness are plotted on the bottom and top abscissa, respectively. The results correspond to laser excitation at 800 nm (500 mW average power, 18 fs pulses) (b), and 400 nm (100 mW, 28 fs pulses) (c). (a) shows a schematic sketch of the Ag film. The curves through the experimental points are to guide the eye. Arrows in (b) denote the regions of the film visualized in TEM in Fig. 3.16.

In regime D the laser-induced signal is negligible for both wavelengths. This means that multiphoton photoemission from the closed Ag film or from extended Ag islands is negligible on the intensity scale of Fig. 3.20. Note that our geometry corresponds to

s-polarized excitation that is ″parity-unfavoured″ because the electric vector lies parallel to the surface. This leads to preferential electron excitation in the surface plane, whereas we detect the electrons above the surface. In addition, the transparency is only about 10% for 30 nm film thickness.

In regime C the decrease of the mass thickness is accompanied by the appearance of gaps in the continuous film, i.e. the coating coefficient decreases. In this range the multiphoton photoemission signal of electrons increases due to an increase of the film roughness [Stu89]. The formation of gaps in the continuous film comes along with an increase of its roughness. The slow increase of the photoemission intensity with a decrease of the mass thickness between 4 nm and about 2.5 nm very likely results from this effect.

In the region where Ag particles on the 10 nm size scale are found inside the gaps of the Ag film, the photoemission current increases abruptly (boundary of regions C and B). This increase amounts to one and two orders of magnitude at λ=400 nm and 800 nm, respectively. This result is most probably determined by a new mechanism of photoelectron emission, femtosecond laser-induced thermionic emission, which competes with the ″conventional″ multiphoton photoemission. The origin of this process will be discussed in detail below. It agrees with prior experiments [Cin04], in which it has been demonstrated that upon excitation at 400 nm the transition from a continuous film to a nanoparticle film is characterized by a strongly increasing photoelectron yield and, what is more essential, by a change of the electron energy distribution.

Although a contribution of resonant absorption by coupling of the exciting light to the localized plasmon modes of the particles to forming the intensity maxima in Fig. 3.20b,c can not be excluded, this process is not dominating. The characteristic plasmon resonance energies of silver particles are located around 3 eV. Much lower energies may be possible in case the particle exhibit extreme deviations from a spherical shape. Besides, after completing the emission measurements, we opened the set-up and measured the dependence of the transmission coefficient for the "red" laser beam on the mass thickness of the Ag film (Fig. 3.21a, solid line). As can be seen, the curve is essentially unstructured, thus ruling out significant resonance features. For our relatively wide size distributions like Fig. 3.19a we expect that certain particles are resonantly excited (see next section) but this does not lead to significant features in the yield spectra in Fig. 3.20b due to averaging over wide size fractions.

The transparency I_{L1}/I_{L0} of a homogeneous closed film is given by Lambert-Beer`s law: $I_{L1}/I_{L0} = e^{-\frac{4\pi k}{\lambda}d}$, where I_{L0} is the intensity of the incident light, I_{L1} is the transmitted intensity, k is the extinction coefficient, λ is the photon wavelength and d is the film thickness. It is shown in Fig. 3.21a as a dashed curve assuming the literature value for Ag at 800 nm, i.e. k=5.6 [Pal91]. The rather large deviation between the theoretically calculated and experimentally measured transparency curves can be explained taking into account that Lambert-Beer`s law (i) does not account for the scattering of light and for peculiarities of the light absorption by small particles; (ii) is valid for continuous films (or solutions with known concentrations); (iii) is derived for linear optics. The extinction coefficient calculated from the experimental data is shown in Fig. 3.21b. In the region 15 nm<d_{eff} <25 nm where the silver film is continuous it varies only weakly and is of the order of the literature value of 5.6. It is two times larger due to the third order effects. It is well known that the absorption coefficient and extinction depend on the light intensity at moderate fluxes. However, in the region d_{eff}<15 nm the extinction coefficient increases due to strong deviations of Lambert-Beer`s law for non-continuous films. In particular, below 5 nm it

rises steeply owing to the strong optical response of the Ag nanoparticles, i.e. Mie-scattering and plasmon excitations.

Under illumination at 400 nm and 800 nm, the dependence of the photocurrent on the mass thickness of the Ag film in the range of $d_{\mathrm{eff}} > 2.5$ nm exhibits qualitatively the same behavior. Obviously this reflects the structural properties of the film in different regions. With decrease of the mass thickness the photoemission current slowly increases. In the range of $d_{\mathrm{eff}} < 2.5$ nm the photoemission current exhibits two maxima at about 1.2 and 0.6 nm mass thickness. The photoemission current for $d_{\mathrm{eff}} = 1.2$ nm exceeds the current in the range of $d_{\mathrm{eff}} > 2.5$ nm by almost two orders of magnitude and by more than one order of magnitude for 800 nm and 400 nm excitation, respectively.

The electrical conductivity of the continuous film including the continuous film (D), the percolated island film with gaps (C), and the region of the particle film (B), immediately adjacent to region (A) is high enough to avoid charging of the sample. Here, the particle film is an ensemble of Ag particles coupled by tunneling through the glass substrate. However, upon a further decrease of the mass thickness, the Ag particle film is characterized by a decrease of the particle size as well as by an increase of the average distance between them. The latter causes loss of the tunneling conductivity. Hence, Ag films with a mass thickness of $d_{\mathrm{eff}} < 0.4$ nm could not be studied in the present work because of their insufficient electrical conductivity that resulted in charging of the sample during the photoemission measurements.

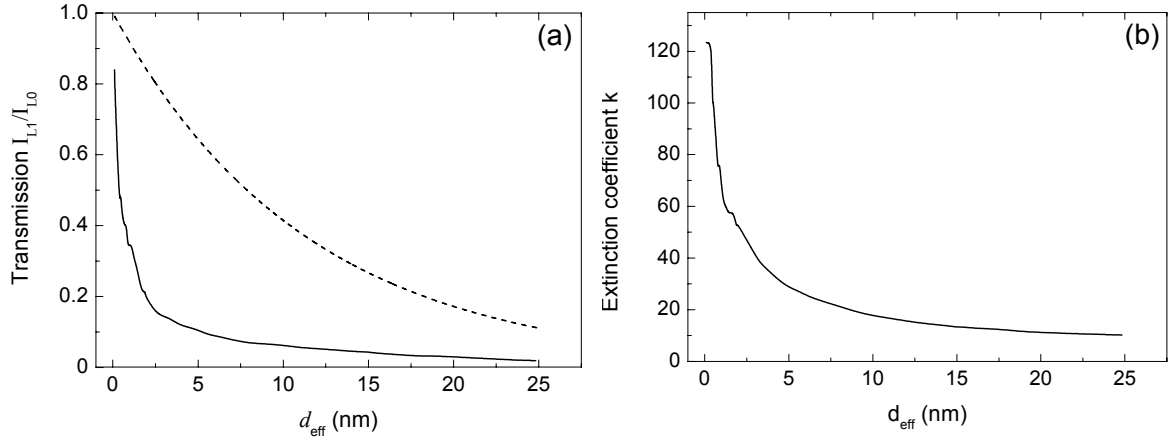

Figure 3.21: (a) Transmission of the wedge-shaped Ag film (solid line). The measurement was performed for the 800 nm laser beam with average power of 590 mW. The transparency curve calculated using Lambert-Beer`s law (see text) is shown as dashed line. (b) The extinction coefficient calculated from the experimentally measured transparency curve.

For comparison, the identical film has been investigated under illumination with the high-pressure Hg lamp, i.e. for the case that the quantum energy exceeds the work function of electrons from Ag. Thus, this result (shown in Fig. 3.22) reflects "normal" 1PPE or threshold emission, originating from the near-surface region with a depth of a few nm. The UV spot size is about 2 mm and is thus a factor of 20 larger than the spot size of the laser beam. From regime D towards C the UV photoemission signal varies only weakly reflecting the surface coverage.

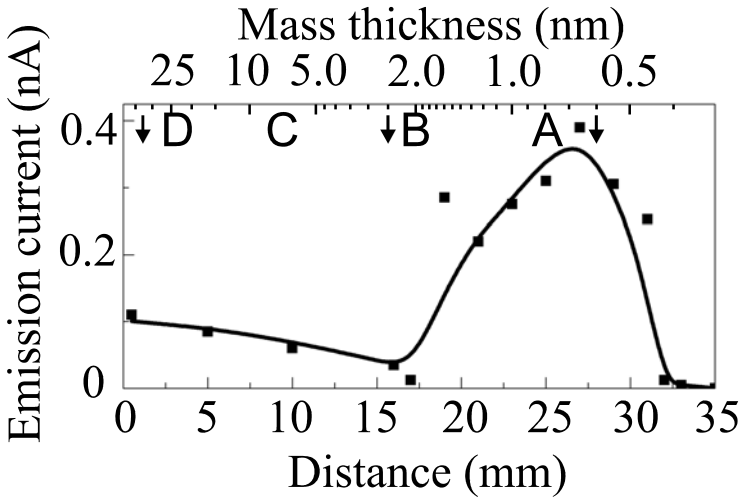

Figure 3.22: Electron emission current from the same film as Fig. 3.20 but under high-pressure Hg lamp excitation ($h\nu \leq 5.2$ eV). The distance from the edge of the film and the corresponding mass thickness are plotted on the bottom and top abscissa, respectively. The curve through the experimental points is to guide the eye.

In regime C the decrease of the mass thickness leads to a decrease of the electron emission current for UV excitation. The photoemission current decreases down to $d_{\text{eff}} \approx 2.5$ nm. After further decrease of the mass thickness the photocurrent rapidly increases. In the range of $d_{\text{eff}} < 2.5$ nm (regimes B and A) the dependence of photoemission current on mass thickness exhibits a non-monotonous behavior with a maximum at about 0.6 nm. Obviously, the cluster film has a higher photoemission yield as compared with the closed film in Regions D and C. Threshold photoemission is observed for the case of the continuous film, if an electron has an energy exceeding the work function, and its momentum is directed within the so-called escape cone with respect to the surface normal. The latter requirement is absent for the case of a nanoparticle film. Furthermore, the 2 mm diameter UV-beam causes a considerable photoconductivity of the surface. This shifts the emission cut-off to lower mass thicknesses (<0.3 nm) compared with Fig. 3.20.

Power dependence

In order to shine further light into the mechanism of electron emission, the dependence of its intensity on the power of the laser beam is informative. As it was shown in section 1.3.1 in case of *n*-photon photoemission in weak fields it is characterized by a power law with the exponent of *n*. Fig. 3.23 shows the dependence of the photoemission intensity of the Ag film with $d_{\text{eff}} = 1.2$ nm on the average power upon excitation with 800 nm (squares) and 400 nm (crosses) laser radiation. The maximum of the particle size distribution histogram corresponds to about $2r = 5$ nm (see Fig. 3.19a). Under 400 nm excitation the dependence of the photocurrent on the beam power exhibits the expected value of $n=2 \pm 0.05$. Obviously, this is a clear fingerprint of true 2PPE throughout the accessible power range from 15–100 mW.

In the case of 800 nm excitation the accuracy of the measurements (see error bars in Fig. 3.23c) does not allow us the exact approximation of the experimental curve with a power function. Nevertheless, the measured curve does not obey a single power law. Instead, it can be separated into two regions. Between 30 and 40 mW average power the

data approximately reflect a power law with a high exponent of about 8, whereas above 40 mW the slope is considerably smaller (about 2) tending to an almost linear behavior followed by a saturation above 300 mW. The steep rise between 30 and 40 mW can also be interpreted as a kind of threshold behavior, smeared out due to the cluster size distribution in the probing spot. The change in slope for 800 nm excitation starts at ~45 mW that corresponds to a field strength value of E~1.2x10^6 V/cm what is in good agreement with the value for the Ag/Si system (see section 3.2.2.).

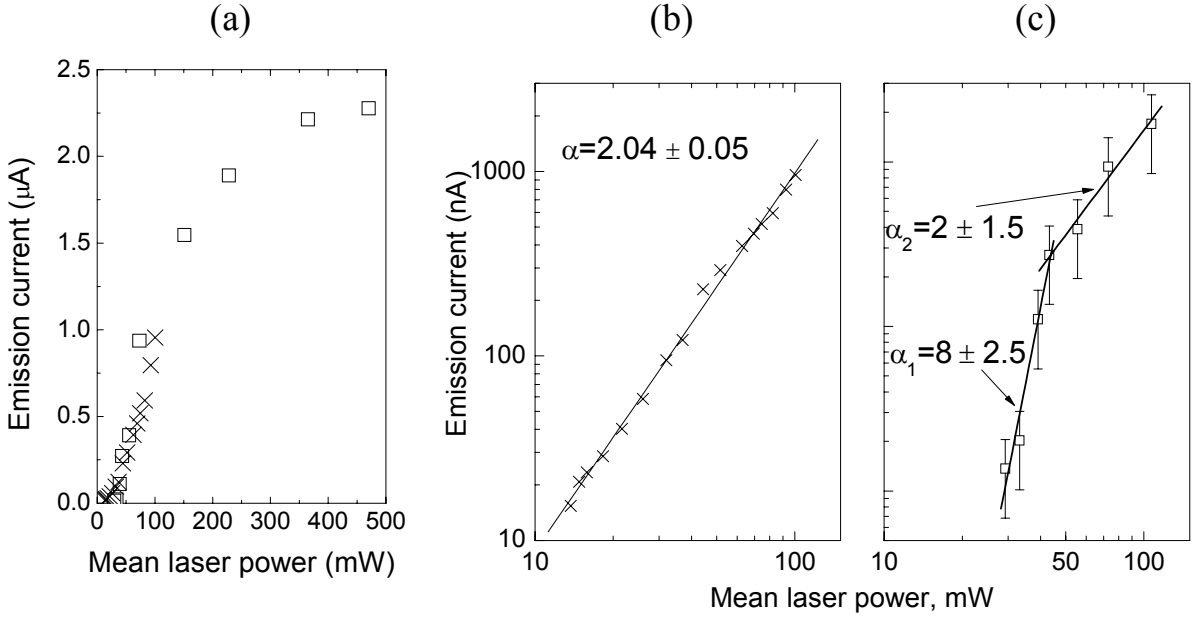

Figure 3.23: Plot of the electron emission current versus average laser power for a Ag particle film with mass thickness of 1.2 nm at 800 nm (squares) and 400 nm excitation (crosses). (b) and (c) show the region up to 100 mW on a logarithmic scale with linear fits.

Pump-probe measurements

The result of the pump-probe experiment is shown in Fig. 3.24. This measurement was performed for a Ag film with d_{eff} = 1.2 nm using the 800 nm excitation. These data give us information on the temporal correlation between two laser pulses incident on the sample. Any correlation time exceeding the temporal width of the laser pulses is characteristic for a sample-intrinsic response time to the laser induced excitation. Using the beam splitter (BS in Fig. 2.8) the fundamental beam was split into two identical beams. To exclude the optical field emission mechanism the pump and probe beams were set to equal average power of 100 mW (weak field regime) and equal pulse widths of 30 fs. Note that this value is only 12 fs (60%) larger than the pulse width of the fundamental beam used for the studies of the electron emission on the mass thickness and the power dependences. Such a small broadening of the pulse width leads to the decrease of the electron emission current from 1700 nA at 18 fs down to 80 nA at 30 fs (see Figs. 3.23 and 3.24). The dependences of electron emission intensity on the laser pulse width are described below.

Upon the combined action of both pulses the electron emission current strongly exceeds the sum of photoemission currents for the cases when either the pump beam, or the probe beam is blocked. The shorter the delay time $\Delta\tau$ between the pump and probe pulses, the more significant is this effect. The photoemission currents for the cases when only the pump

beam or only the probe beam is active are about 5 nA, i.e. 10 nA in sum. When switching on the second beam at $\Delta\tau = 0$ the power is doubled but the current goes up by a factor of 16 (from 5 nA for one 100 mW beam to 80 nA for both beams, i.e 200 mW). This corresponds to a power of n=4. With the accuracy of the measurements for combined action of pump and probe beams the current is equal to 10 nA for delay times $\Delta\tau > 100$ fs. This value is much larger than the pulse width of pump and probe beams (30 fs) but much less than the distance between adjacent pulses, being 12.5 ns (at a repetition rate of 80 MHz). More important, we observe an increase in this time with decreasing mass thickness (i.e. decrease of the average particle size) up to values of several picoseconds.

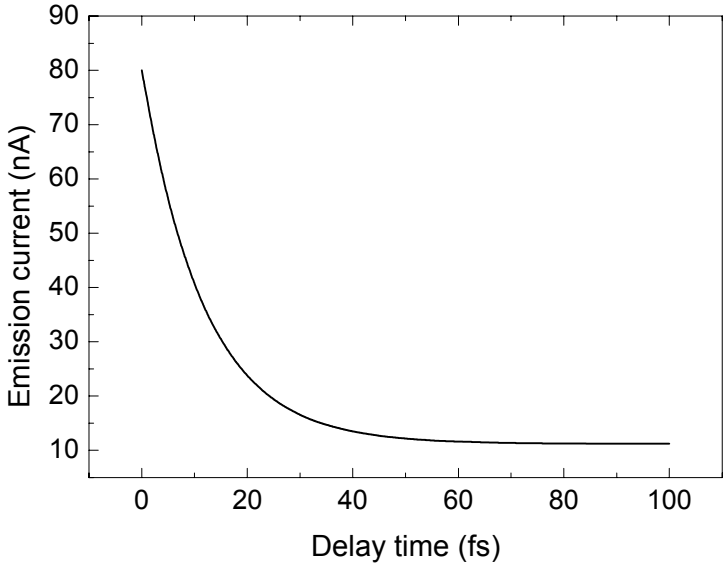

Figure 3.24: Electron emission current measured for a Ag film with mass thickness of 1.2 nm versus delay time between pump and probe pulses (photon energy 1.55 eV, FWHM 30 fs, average power of both pump and probe beams 100 mW). The full line serves to guide the eye.

We studied the dependence of the electron emission intensity on the time delay between pump and probe pulses also for a gold particle film. A typical auto-correlation trace is shown in Fig. 3.25a. Its FWHM increases with decreasing film mass thickness (Fig. 3.25b). It shows that the microscopic mechanism responsible for the photoemission is strongly affected by the size of the emitter. This confirms the result of the quantum-statistical treatment presented in section 1.4 that the probability of thermionic and thermally-assisted multiphoton photoemission increases when the particle size decreases. The step increase of the relaxation time at a mass thickness of 10 nm is most likely attributed to the appearing of the gaps and clusters inside them in the continuous gold film.

Furthermore, in a nanoparticle, the quantization of the energy levels in the conduction band can be an important factor, as the level spacing increases with decreasing particle size. Therefore in a sufficiently small nanoparticle the quantization of the energy levels should manifest itself in a larger relaxation time, as electron-electron scattering events have to obey both energy and momentum conservation laws which get harder to satisfy when certain energies and momenta are forbidden.

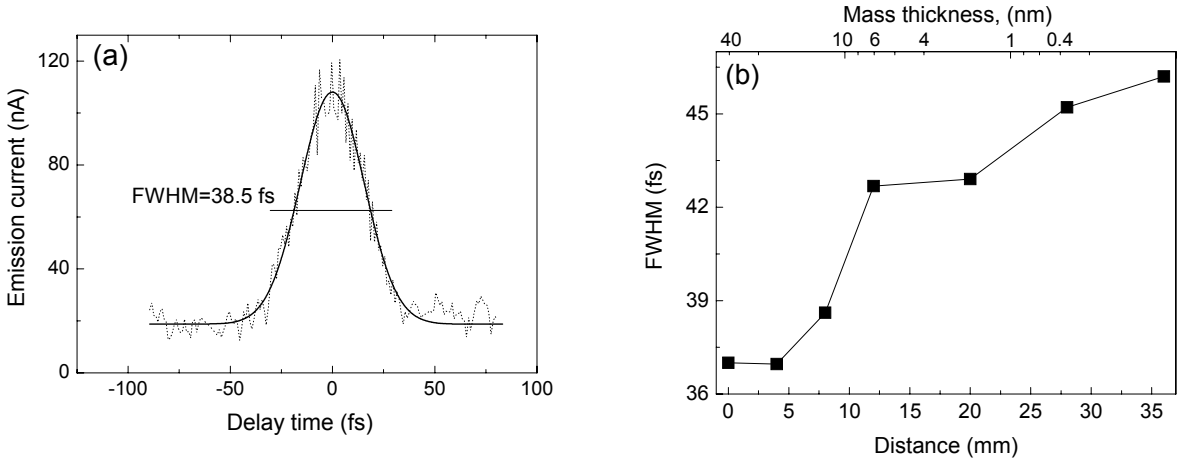

Figure 3.25: (a) Auto-correlation trace as obtained during a monochromatic pump and probe experiment (quantum energy 1.55 eV, pulsewidth 30 fs) on a gold film. (b) The dependence of the FWHM of the autocorrelation trace on the distance of the gold film from the evaporator. The mass thickness is shown on the top.

Dependence on the laser pulse width

The dependence of the electron emission intensity on the laser pulse width is informative for understanding the mechanism of electron emission. The minimum laser pulse width used in this set-up was 85 fs and the average power was 400 mW. The current sensitivity was 0.1 nA.

Fig. 3.26 illustrates such dependences for excitation at 800 nm and for Ag films with mass thicknesses of $d_{\text{eff}} = 0.6$ (curve 1), 1.2 (curve 2) and 2.5 nm (curve 3), respectively. This measurement can be considered as a quasi-pump-probe experiment where only one wing of the auto-correlation trace is measured. The maximal emission current registered in this experiment was 30 nA that is two orders of magnitude smaller than the current from the same sample excited by 18 fs pulses, see Fig. 3.23. Due to the increase in the peak intensity, a decrease of the laser pulse width causes an increase in the electron emission intensity. This effect is non-linear and depends again on particle size. The nonlinear slope of this dependence becomes weaker when the Ag particles become smaller: curves 1 and 2 correspond to average particle sizes of $2r = 3.5$ and 5 nm, curve 3 is measured on an island film with gaps.

This behavior does not follow directly from the mechanism of multiphoton photoemission. In the framework of the thermally-assisted multiphoton photoemission (see section 1.3.3) this means that the electron and phonon subsystems remain in the non-equilibrium state longer in the case of smaller particles. This experimental result agrees with the suggestion of a reduced electron-phonon coupling in small particles (section 1.2.2). In the performed experiment the emission current could not be registered for films with mass thicknesses $d_{\text{eff}} \geq 3$ nm excited at 800 nm.

Note that according to Fig. 3.20 the total photoemission current shows in this size regime a non-monotonic dependence on particle size (see also scaling factors in Fig. 3.26). We particularly observe that for the continuous silver films exhibiting gaps the nonlinear dependence on the laser pulse width increases with the number of gaps, but the total current value decreases. Even more, the photoemission current dropped below the sensitivity limit of 0.1 nA of the used picoampere meter for films with mass thicknesses $d_{\text{eff}} \geq 3$ nm. Note

that at the minimum pulsewidth of the ″red″ laser beam of 78 fs and an average power of 400 mW the laser pulse intensity in this set-up was far below that one used to record the data shown in Fig. 3.20.

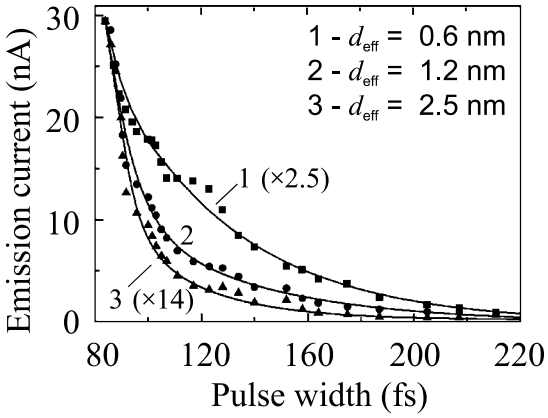

Figure 3.26: Electron emission current measured as a function of the width of the laser pulse for Ag films with mass thicknesses d_{eff}= 0.6 (curve 1), 1.2 (curve 2) and 2.5 nm (curve 3) excited at 800 nm (average power 400 mW).

3.2.1.3 Discussion and conclusions

The above results indicate a change from the multiphoton photoelectron emission process dominating for a continuous Ag film to another prevailing mechanism acting in the case of a particle film for excitation with the fs-laser. The electron emission current first increases with decreasing mass thickness because of an increasing number of clusters in the film. Below d_{eff} =1.2 nm the current decreases because the amount of Ag drops and tends to zero. It means that the non-monotonous dependence of the photoelectron emission current on the mass thickness of the Ag film in the range of d_{eff} < 2.5 nm is not directly related to the emission mechanism. This conclusion follows from the fact that the positions of the main maxima of these curves for the two wavelengths coincide (Fig. 3.20b,c) while the emission mechanisms are different. The maximum at 1.2 nm simply reflects an ″optimum″ particle density in the film, i.e. it is a structural feature of the film morphology. In the right boundary of region A where multiphoton photoemission is weakened due to the reduced amount of metal (right dashed line in Fig. 3.20) the increasing number of particles with the size < 5 nm most likely gives rise to the thermionic electron emission channel, present at both photon energies (see section 1.4).

Striking characteristics of this new emission process are the rather moderate dependence of the electron yield on the excitation wavelength and the specific and particle-size dependent temporal response (see Figs. 3.24-3.26). As discussed above, both effects cannot be brought in line with a conventional multiphoton photoemission process. Instead we can relate the electron emission at least partly to a *laser heating of the electron gas in the metal particles* (see section 1.3.2). This emission channel opens if sufficient energy can be fed and accumulated in the electron subsystem of the particle. In this connection it is helpful to remind that on sub-picosecond time scales the electron and phonon gas are initially

decoupled, where the efficiency of the internal energy transfer between both subsystems is determined by the electron-phonon coupling constant.

Consequently, heating of the electron gas with a femtosecond laser-pulse gives rise to a *transient non-equilibrium ($T_e > T_{ph}$) state*. At temperatures T_e high enough (by analogy with the thermionic emission it is ≥2000 K), the tail of the non-Fermi-Dirac electron energy distribution exceeds the vacuum level. Electrons from this tail area can leave the cluster and escape into the vacuum. Owing to multiple scattering processes, these electrons have lost their ″memory″ on the initial photoexcitation, comparable to the so-called ″true secondaries″ that arise in any photoemission experiment with sufficient excess energy. The total emission current j is given by the Richardson-Dushman equation for thermionic emission (Eq. (1.15)). It is evident that this equation contains no explicit dependence on the excitation wavelength. Implicitly, however, the achievable electron gas temperature T_e is in first order governed by the absorbed fluence of the incident electromagnetic wave, and depends therefore on the wavelength-dependent absorption cross section of the material. In the visible regime this dependence is rather weak and the sensitivity of the total photoemission yield on the photon energy should be much less pronounced than in case of multiphoton photoemission, in correspondence with our experimental observations.

To account for the observed *particle size dependence* of the photoemission yield characteristic (see Fig. 3.20 and Fig. 3.26), the exponential dependence on T_e and the work function comes into play. For a metal we can estimate the mean free path l_{e-ph} for electrons close to ε_F by $l_{e-ph} = \tau \cdot v_F$, where τ is the Drude relaxation time and v_F is the Fermi velocity. For silver at room temperature values of τ and v_F are 40 fs and $1.4 \cdot 10^8$ cm/s [Ash00] giving rise to 60 nm mean free path, which is indeed much larger than the size of the particles under investigation. The inequality $2r < l_{e-ph}$ means that the electron in the particle can move without phonon scattering, reflecting several times from its surface, comparable with an electron oscillator. For evaluation of its frequency $\omega_e = v/2r$ let us assume a particle diameter of $2r$ = 10 nm. Thus the frequency of the electron oscillator ω_e = 10^{14} s^{-1} significantly exceeds the Debye frequency (maximal frequency of the phonon spectrum) for Ag $\omega_D = 4.7 \cdot 10^{12}$ s^{-1} [Nei58]. The smaller the particle size, the stronger is the inequality $\omega_e >> \omega_D$ and, therefore, the weaker is the interaction between the electron and phonon subsystems. Weakening of the electron-phonon interaction means that the energy absorbed by the particle from the laser pulse is stored more efficiently by the electron subsystem before being transferred to the phonon system so that the electron gas dwells at high temperatures for a longer time. Such a weakening in the electron gas cooling rate for small particles fits to the observed dependence of the photoemission current on the laser pulse width and, hence, laser pulse intensity (Fig. 3.26) which becomes less steep as the particles become smaller. For the different laser pulsewidth the changes in T_e and, therefore, the changes in the emission yield is obviously less pronounced for small particles than for the larger particles. Such an observation does not follow directly from the mechanism of the instantaneous multiphoton photoemission.

The role of *the work function of the silver particles* with respect to the dependence of the photoemission yield on particle size as shown in Fig. 3.20 has been discussed already above. The exponential dependence of the thermionic emission current on ϕ in Eq. (1.15) accounts

for the appearance of the work function governed maximum in the photoemission yield located at $d_{\text{eff}} = 0.6$ nm in the case of excitation of the particles with the pulsed lasers.

The threshold photoemission under excitation with the UV-lamp is also determined by the work function. Thus the position of the maximum of the curve in Fig. 3.22 reflects the minimum of the work function of the particles followed by the steep drop at $d_{\text{eff}} = 0.5$ nm caused by the increase of the work function for very small particles along with the low conductance of the cluster layer.

What do we expect in femtosecond laser-induced thermionic emission when the energy pumped in the particle is successively increased (see Fig. 3.23)? Initially T_e will increase, however, this increase is limited by the fact that with growth of the electron temperature the heat capacity of the electron subsystem also increases. The electron temperature grows until a balance between the amounts of energy fed to the electron subsystem from the outside and transferred from it to the phonon subsystem is achieved. It means that the value of the electron temperature and, therefore, the electron emission intensity tends to saturation with growth of input power. Nonlinear dependence of power transferred from the electrons to the phonons $\sim\left(T_{\text{e}}^2 + T_{\text{ph}}^2\right)$ as well as the fact that with growth of the electron temperature additional ways of energy losses from the electron gas can appear, promote the saturation. The data points for the 800 nm excitation in Fig. 3.23a show this saturation. It is absent for the data points for the 400 nm excitation beam because the maximum value of the average power of the 400 nm laser beam is a factor of 5 smaller than that of the 800 nm laser beam.

The saturation can also be explained using the Rethfeld formalism. Following [Ret02], after a low power excitation, the phonon cooling of the nonequilibrium electron gas is much less efficient than the cooling of a corresponding thermalized Fermi-distributed electron gas, while in the case of the strong perturbation the cooling of the laser-excited electron gas by phonon emission is nearly as efficient as the cooling of the Fermi-distributed electron gas. Therefore, the cooling rates of the electron subsystem are far from being the same for low- and high-power excitations (see section 1.1). This means that in the case of low-power excitation the electron subsystem stays thermally decoupled from the phonon bath for a longer time favouring the thermionic emission mechanism.

Let us estimate the *quantum yield of electron emission*. As is seen from Fig. 3.20b,c, the maximum of the photocurrent is observed for excitation of the particle film with $d_{\text{eff}} = 1.2$ nm using the fs-laser system. This corresponds to an emission current of $I_{\text{e}} = 2.3$ μA for the "red" laser beam with an average power of $P = 500$ mW and to $I_{\text{e}} = 0.16$ μA for the "blue" laser beam with an average power of 100 mW. Thus the quantum yield is $(I_e / e)/(P / h\nu \cdot e) = 6.9 \cdot 10^{-6}$ and $4.8 \cdot 10^{-6}$ electrons per photon for the ″red″ and ″blue″ laser beams respectively. This value is very large for multiphoton emission. It should be noted that good scintillators are characterized by a quantum yield of 10^{-8}. An increase of the quantum yield of photoelectrons from metal nanoparticles is described in Refs. [Kat61, Leh00, Sab90]. The quantum yield increases further by several orders of magnitude if a Ag particle film is activated by cesium and oxygen [Sab90, Nol04].

Now we will estimate how high the electron temperature can be in the present experiment. The duration of the fs-laser pulses was varied from tens to hundreds of femtoseconds, i.e. it lies between the characteristic times of the electron-electron $\tau_{\text{e-e}} = 1$-10 fs [Gin55, Gro95] and electron-phonon $\tau_{\text{e-ph}} = 1$ ps [Fuj84, Els87, All87] interactions. The thermalization time of the electron and phonon subsystems is less than 1 ps [Ani70, Ret02] and 1-10 ps [Gro95, Fat98, Fan92a, Ani70, Ret02], respectively. Thus, the

heat transfer from the electron subsystem to the phonon system can be neglected during the pulse action. Therefore, the change of the electron gas temperature dT_e and increment of the quantity of heat δQ (from the laser pulse) are related by the expression (1.7)

$\delta Q = c_e dT_e$.

The heat capacity of the electron gas depends on its temperature, and for N electrons takes the following form [Lan68]:

$$c_e = \frac{\pi^2 k_B^2}{2\varepsilon_F} T_e N = \gamma T_e N \qquad (3.2)$$

where $\gamma = \frac{\pi^2 k_B^2}{2\varepsilon_F} = 6.2 \cdot 10^{-9}$ eV/K^2. We will integrate expression (1.7) and will derive T_e from it. Thus, neglecting all kinds of energy dissipation (″sudden approximation″), we have for the *transient electron temperature*:

$$T_e = \sqrt{\frac{2Q}{\gamma N} + T_{ph}^2} = \sqrt{3.2 \cdot 10^8 \frac{Q}{N} + T_{ph}^2}. \qquad (3.3)$$

The fluence in a single pulse for the 800 nm laser beam with average power of 500 mW and diameter of 100 μm is $J = 8 \cdot 10^{-5}$ J/cm^2 = $5 \cdot 10^{14}$ eV/cm^2. We assume a Ag particle size with $2r$ = 5 nm (see Fig. 3.20a corresponding to a Ag film with d_{eff} = 1.2 nm, for which the maximal photoemission is observed) and a density of Ag atoms of $\rho = 5.9 \cdot 10^{22}$ cm^{-3}. Then, we arrive at 63 photons per 5nm particle so that per electron fall on average $\frac{3J}{2\rho a}$ = 0.025 eV for the 800 nm laser pulse. Substituting $\frac{Q}{N}$ = 0.025 eV and T_{ph} = 300 K (room temperature) in expression (3.3), gives 2800 K. The density of electron states in Ag, reflection, transmission, as well as local statistical deviations of the quantity of energy absorbed by the particles from their average values, related to the quantum character of laser radiation absorption by particles and fluctuations of the photon flux density, were not taken into account in this estimation. The latter effect is the more essential, the smaller the particle size, see the quantum-statistical treatment in section 1.4.

The derived dependence (3.3) is plotted in Fig. 3.27. It is clearly seen that the contribution of the hot electrons to the electron emission from a 5 nm particle can not be neglected even if only 15% of the laser flux is absorbed. In this case the maximal electron temperature is far beyond 1000 K. Also it should be noted that the absorption cross-section of the metal particles can significantly exceed their geometrical cross-section (criterion is the extinction coefficient of the particles at the given photon wavelength) [Mes81]. It depends on the size of the particles (proportional to the surface area, i.e. $\sim r^2$), their shape and the optical constants. As was shown above, in the present experiment the Ag particles' shape was close to spherical (multiple twinned particles). In the general case the absorption cross-section significantly depends on the actual shape of the particles. This dependence is more essential, the higher the value $(\omega_p/\omega)^4$, where ω_p is the plasma frequency.

The energy distribution of free electrons is deformed (non-Fermi-Dirac) and develops into a Fermi-Dirac distribution, described as transient electron gas heating after a certain time (see section 1.1). When the temperature increase of the electron subsystem is small (low-perturbation regime), the tail of the thermal distribution of electrons does not reach the

vacuum level. In this case photoemission may appear due to the absorption of an additional photon by the heated electrons, see Fig. 1.11. However, sufficiently strong heating may lead to direct thermionic emission without absorption of a further photon. The higher the absorbed power and the lower the energy dissipation to the phonon subsystem, the higher the maximal electron gas temperature. The first condition can be realized by increasing the laser pulse power or decreasing the spot size or pulse width, the second one by the reduction of the size of the metal particles. Au particles with sizes of a few tens of nanometres and smaller are stable to the irradiation with a CO_2 laser with a power density of 0.1 J/cm^2 (wavelength of 10.6 μm, pulse width of 1 μs) [And84, Ben86, Ben88]. This is four orders of magnitude greater than in the present paper. Thus in the case of infrared illumination ($h\nu$ = 0.1 eV) where the multiphoton processes are excluded, the escape of the electrons from the tail of their thermal distribution above the vacuum level could be responsible for the electron emission from Au nanoparticles. It is important to mention, however, that (i) this long pulse width can be considered as cw-excitation rather than pulsed excitation on the time scale of electron-phonon thermalisation and (ii) optical field emission mechanism can also come into play at such low frequencies.

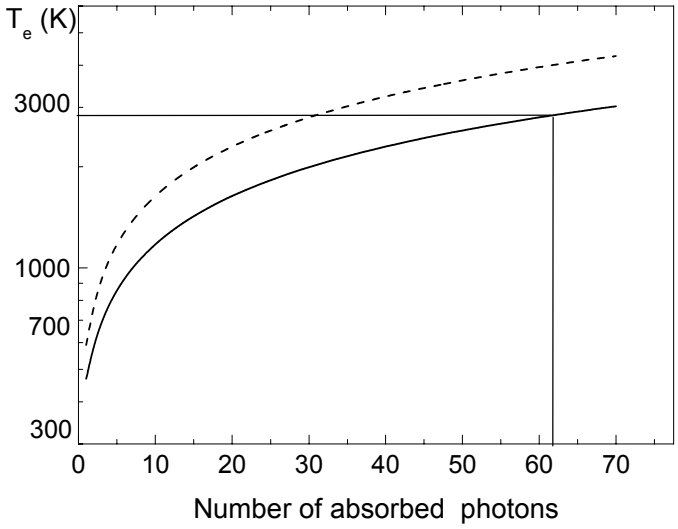

Figure 3.27: Maximum electron temperature T_e (in the ″sudden approximation″) induced by absorption of 1.55 eV (full line) or 3.1 eV (dashed line) in a spherical silver particle with a diameter of 5 nm as a function of the number of absorbed photons.

Energy dissipation channels

Each laser pulse carries 6.25 nJ that is partly absorbed by the metal cluster film. This energy is absorbed by the electron subsystem. Apart from the radiative decay channel (Mie scattering) there are three energy dissipation channels that can be considered: (i) electron emission, (ii) blackbody emission and (iii) energy transfer from the electrons to the lattice followed by heat transfer from the lattice to the substrate. Let us estimate their quantitative contribution.

(i) Each electron emitted to the vacuum carries approximately the energy equal to the work function $\phi \approx 4.7$ eV. Considering the maximal registered current of 2.5μA we can estimate that approximately $2 \cdot 10^5$ electrons are emitted in/after one laser pulse. The energy

outflow due to the electron emission is thus 0.15 pJ per pulse ($4 \cdot 10^{-4}$ % of laser beam energy) that equals 12 μW average power.

(ii) The electron subsystem being heated to 3000 K emits electromagnetic waves (blackbody radiation). The total energy radiated per unit surface area in unit time (energy flux density) j_{BB} of the thermal radiation from the black body is described by a Stefan-Boltzmann law: $j_{BB} = \sigma T^4$, where $\sigma = 5.67 \cdot 10^{-8}$ $J \cdot s^{-1} \cdot m^{-2} \cdot K^{-4}$ is the Stefan-Boltzmann constant. To estimate the electromagnetic energy emitted after a single laser pulse we plot the time dependence of the temperature of the electron subsystem (Fig. 3.28a) in the framework of the two-temperature model (see section 1.1, Eq. (1.4)). We assume instantaneous excitation with $T_{e,t=0} = 3000K$ and equal temperature distribution in the area 100 x 100 μm illuminated by the laser, $\gamma = \frac{\pi^2 k_B^2}{2\varepsilon_F} N_e = 58\left[\frac{J}{m^3 K^2}\right]$, where N_e is the number of free electrons in $1m^3$ of silver, $\alpha_{e\text{-}ph} = 3 \cdot 10^{16}\left[\frac{W}{m^{-3} K^{-1}}\right]$ [Hod00]. Temperatures of the electron and phonon subsystem will be equalized at T=600 K because the heat capacity of the electron subsystem is about 10 times smaller than that of the phonon system.

Fig. 3.28b shows the time evolution of the electromagnetic radiation power calculated using the Stefan-Boltzmann law. As we do not know the time evolution of the temperature after cooling of the electron gas, we estimate the quantitative value of the power only when $T_e >> T_{ph}$. The integration of the power dependence (Fig. 3.28b) gives the value of energy loss due to black body radiation of about 0.052 pJ per laser pulse or 4.2 μW power. This radiation could in principle be measured by means of an IR sensor mounted near to the metal cluster film. The power of the black body radiation is higher than the sensitivity limit of the commercial IR sensors.

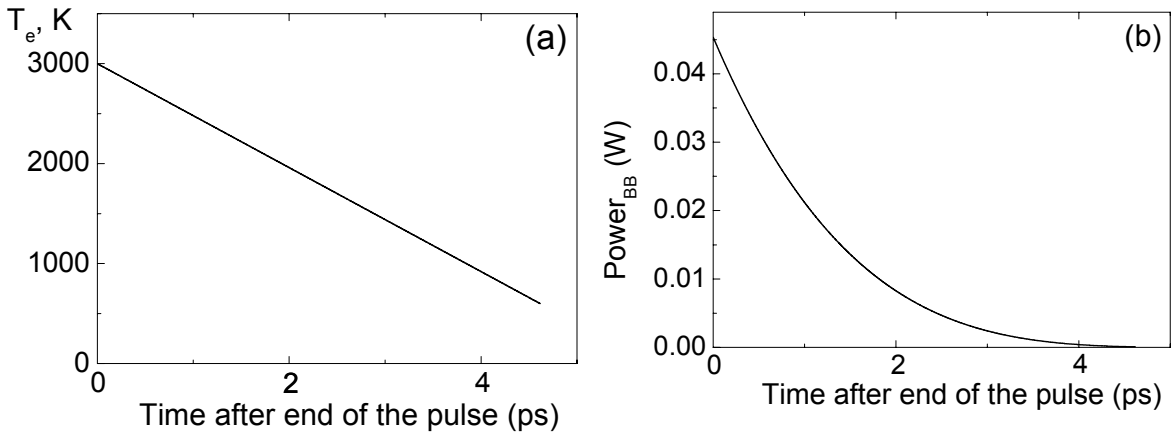

Figure 3.28: (a) The time dependence of the temperature of the electron subsystem. Time t=0 denotes the moment of instantaneous heating. (b) The respective time evolution of the black body emission power.

(iii) The heat transfer from the nanoparticles into the substrate occurs on a much longer time scale than electron-phonon relaxation time and is not well studied. However, this

mechanism is the main channel of the energy dissipation from the metal cluster film under femtosecond laser excitation. The heat transfer rate should be high enough to keep the particles temperature below the melting point (1260 K for a bulk silver). It should be noted that even with the unamplified Ti:sapphire oscillator used in this experiment laser beam focusing to a spot of <100 μm diameter caused the particles in the center of the laser spot being melted.

In this section we presented the results of electron emission from Ag and Au films on a glass substrate with a gradient of the film thickness from 1 nm to 25 nm under fs-laser excitation at $h\nu$ =1.55 eV (pulsewidth 18-300 fs, fluence 80 μJ/cm^{-2}, photon flux 3.3 nm^{-2}) and at $h\nu$ =3.1 eV (pulsewidth 28 fs, fluence 16 μJ/cm^{-2}, photon flux 0.32 nm^{-2}), and also under UV excitation ($h\nu \leq$ 5.2 eV). The main characteristics the of photoemission signal are presented, such as the dependence of the emission current on the pulse duration, the average power of the laser radiation, and the delay time in a pump-probe measurement. The results obtained allowed us to distinguish possible mechanisms of electron emission by means of analyzing a set of conditions of their realization. In particular, the following results have been obtained:

- An increase of the electron emission intensity during transition from a continuous film to a particle film is observed under fs-laser excitation with the quantum energy below the work function ($h\nu < \phi$) (as well as under excitation with a high-pressure Hg lamp ($h\nu \geq \phi$) (threshold photoemission)). Upon excitation with the fs-laser the intensity increased by orders of magnitude.

- In the whole range of mass thicknesses of the Ag particle film the electron emission intensity upon excitation by the 800 nm laser beam (18 fs pulsewidth) is higher than for the 400 nm laser beam (28 fs pulsewidth), the average powers in both cases were of the same order of magnitude (few hundreds of mW).

- The photoemission intensity increases with decreasing pulse width in the range of 18-200 fs, but this dependence becomes less steep as the particles become smaller. The latter fact does not follow directly from the mechanism of multiphoton photoemission.

- Under excitation of the particle film by the fs-laser, more intense electron emission (by more than one order of magnitude higher) having obviously a different mechanism is added to the pure multiphoton emission which occurs for the continuous and percolated Ag films. It dominates for the particle films in particular for diameters below 5 nm. By comparison with model calculations and quantitative estimations we demonstrate that the novel mechanism is thermally-assisted single- or multiphoton photoemission. This hypothesis is capable to explain the whole set of the obtained experimental results.

3.2.2 Spectromicroscopy of Ag nanoparticle films

In this section we present the results of multiphoton spectromicroscopy studies of Ag nanoparticle films on Si using fs-laser excited PEEM. The thin films under study had discrete, rather narrow cluster size distributions that allowed to study the dependence of the electron emission intensity on the cluster size and the fs-laser wavelength. The laser pulses had widths of 100 fs and 200 fs for the 800 nm and 400 nm radiation, respectively. In the previous experiment (section 3.2.1) the size distribution of the clusters was broader but the laser pulses were much shorter (18 fs and 28 fs, respectively).

3.2.2.1 Sample preparation and characterization

The Ag films were deposited in UHV by electron beam evaporation onto a Si(111) substrate at room temperature. Before, the passivating native oxide layer was removed by substrate heating in UHV. The sample consists of regions with different nominal thicknesses, prepared by moving a shadow mask in front of the surface during exposure to the Ag atom beam. The mass thickness changes from 0 to 100 nm with five intermediate steps (stripes); each terrace is about 20 μm wide. Mass thickness was determined by a quartz balance thickness monitor. We label the regions of different coverage by numbers, with 0 corresponding to 0 nm Ag coverage (i.e. to the bare Si substrate), 1 to 5 corresponding to the regions with Ag film nominal thickness of 1, 2, 5, 10 and 20 nm, respectively (see Fig. 3.29), and 6 for bulk silver (nominal thickness 100 nm).

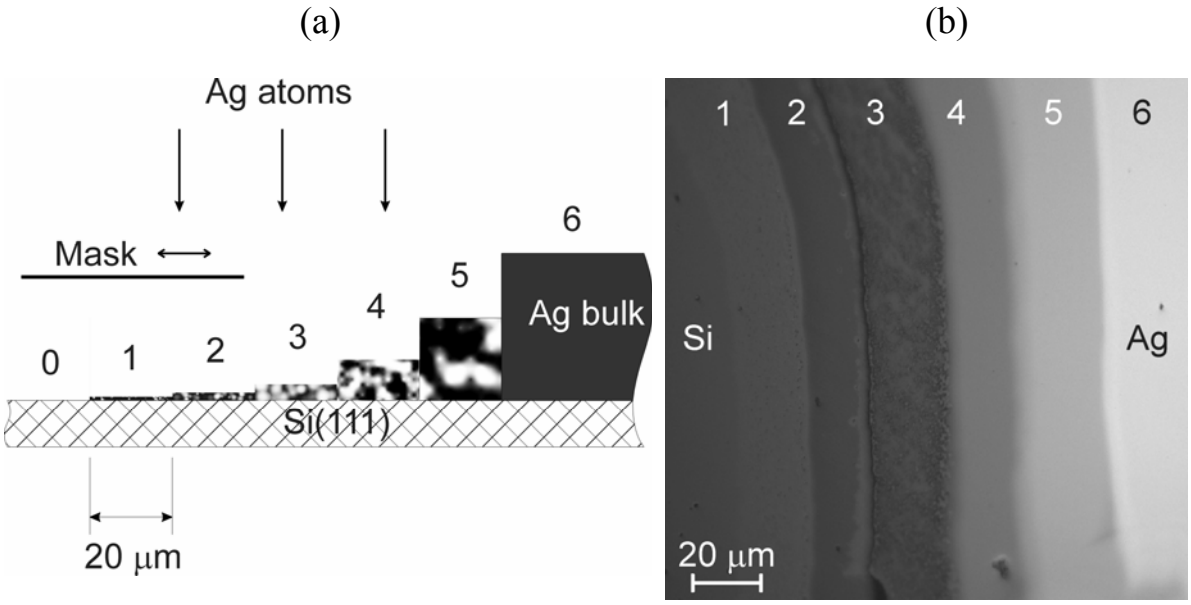

Figure 3.29: (a) Schematic representation of the sample preparation procedure and structure. Regions 0 to 6 correspond to an Ag film nominal thickness of 0, 1, 2, 5, 10, 20 and 100 nm, respectively. The parameters of the different regions are given in Table 3.1. Terraces 1 to 5 are about 20 μm wide. (b) Optical image of the sample showing the stepped Ag wedge.

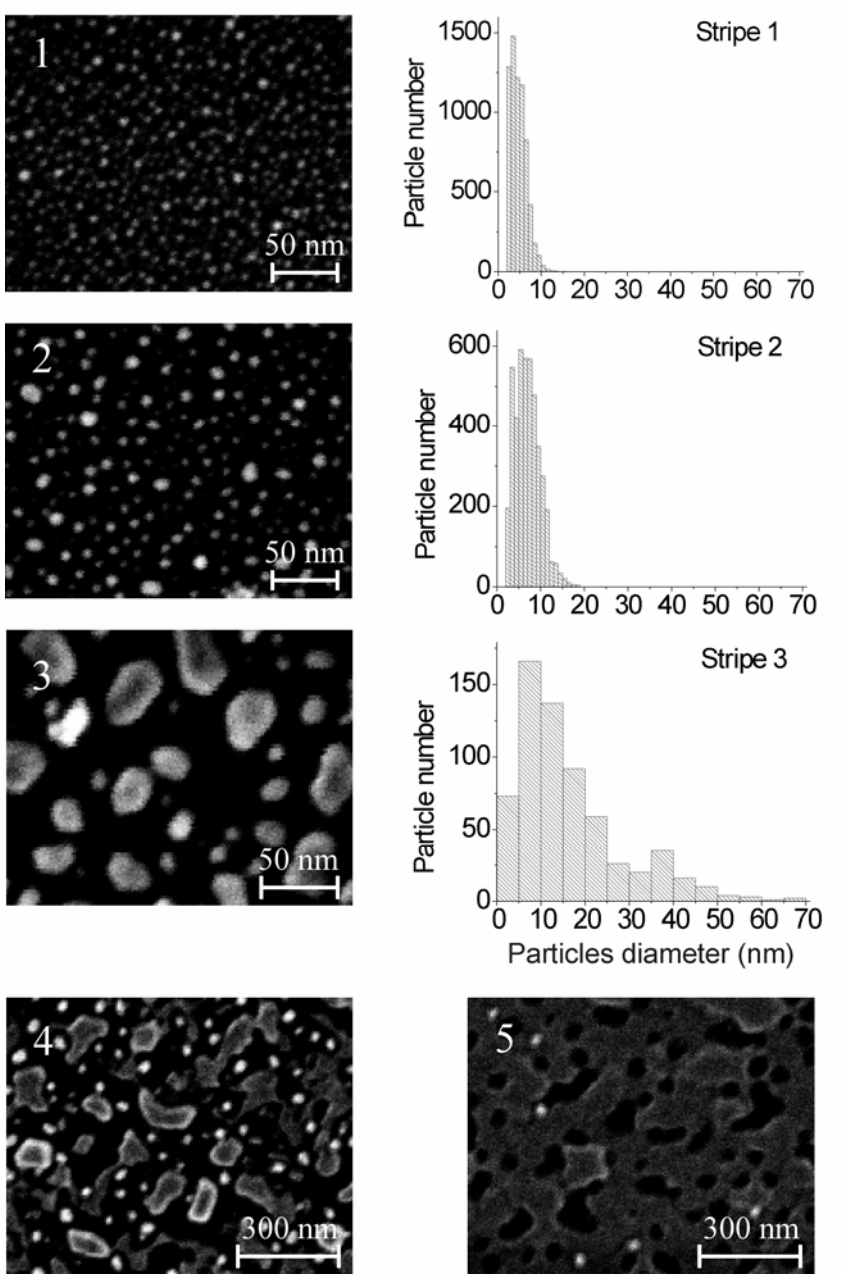

Figure 3.30: SEM images of the stepped silver wedge (stripes 1-5) and cluster size distributions in the silver cluster films. White spots with a size of 30-50 nm in the image of stripes 4 and 5 are substrate defects or Ag clusters oxidized during the transfer of the sample from the PEEM chamber to the SEM.

From the surface area covered by the clusters as estimated from the SEM images the cluster size was determined (see Table 3.1). The histograms in Fig. 3.30 have been determined by evaluating areas of 1.5 μm^2. The clusters were assumed to have a spherical shape. These calculations were verified by comparing the known total amount of deposited material and thus the volume of all clusters. To verify the cluster sizes, we used the following assumptions: (i) the sticking coefficient of Ag on the Si substrate is unity; (ii) all the Ag atoms are in Ag clusters which are visible by the scanning electron microscope. If

the condensation coefficient is smaller than unity, the cluster size will be smaller than the calculated one. Under these assumptions the deviation of the calculated values from the real ones is estimated to be in the range of less than ten percent which is actually the estimated accuracy of coverage determination using the quartz microbalance.

Stripe	Mass thickness, nm	Surface Coverage, %	Average cluster diameter, nm	Cluster size distribution, nm	FWHM of distribution, nm
1	1	13	3-4	2-12	5
2	2	16	6-8	2-19	7.5
3	5	29	8-12 and 35-45	3-70	15
4	10	46	110	50-150	-
5	20	82	Percolated film	-	-
Bulk Silver	100	99	Closed film	-	-

Table 3.1: The parameters of the Ag/Si cluster film sample (stepped wedge) studied by fs-laser excited PEEM.

The resolution limit of the SEM used is 2 nm, therefore we cannot tell anything about clusters with a size 2 nm or smaller because they are all visualized as 2-3 nm clusters. Clusters smaller than 2 nm are present in the stripes 1 and 2 but this size is not dominating, because the maximum of the cluster size distribution in these stripes was estimated to be 3-4 nm and 6-8 nm, respectively. These values are clearly above the resolution limit. There are two subsystems of silver clusters in stripe 3 with the main maximum peaking at 8-12 nm and a less pronounced flat maximum at 35-45 nm. Stripe 4 already consists of silver islands with sizes up to 150 nm. The clusters size was not estimated for stripe 5 because it is beyond the percolation limit.

3.2.2.2 Wavelength dependence of the images.

Fig. 3.31 shows an optical (a) and a UV-PEEM image (b) of the Ag/Si stepped cluster film. The average photoemission intensity from different regions of the stepped Ag wedge under UV excitation ($h\nu \leq 5.2$ eV) is shown in (c). The UV quantum yield shows a monotonous increase of the electron emission with decreasing Ag coverage from region 6 to 2. This can be explained by taking into account that the escape function of a rough surface [Che86] is larger than the corresponding quantity of a smooth surface [Car78]. The electron escape function takes into account that the electrons, before escaping into vacuum, have to travel through the surface barrier. This is possible only if they posses a component k_n of the total momentum k along the surface normal which is greater than the critical value $k_c \propto \sqrt{\varepsilon_F + \phi}$. This results in a higher photoemission yield from rough surfaces [Stu89]. The decrease of the nominal thickness from 100 (Region 6) to 10 nm (Region 4) leads to gap formation in the continuous film that comes along with an increase of its roughness. Stripes 2 and 3 consist of clusters and possess the largest roughness. In addition, the local work function of the particles may decrease due to the decrease of the mirror

charge potential [Woo81] This fact was proven by the microspectroscopy measurements (see below). Finally, the photoemission intensity from stripe 1 drops. This reflects the decreasing coverage of the surface with Ag clusters. Concerning the bare Si surface (Region 0) it is known to appear very dark in UV-PEEM images.

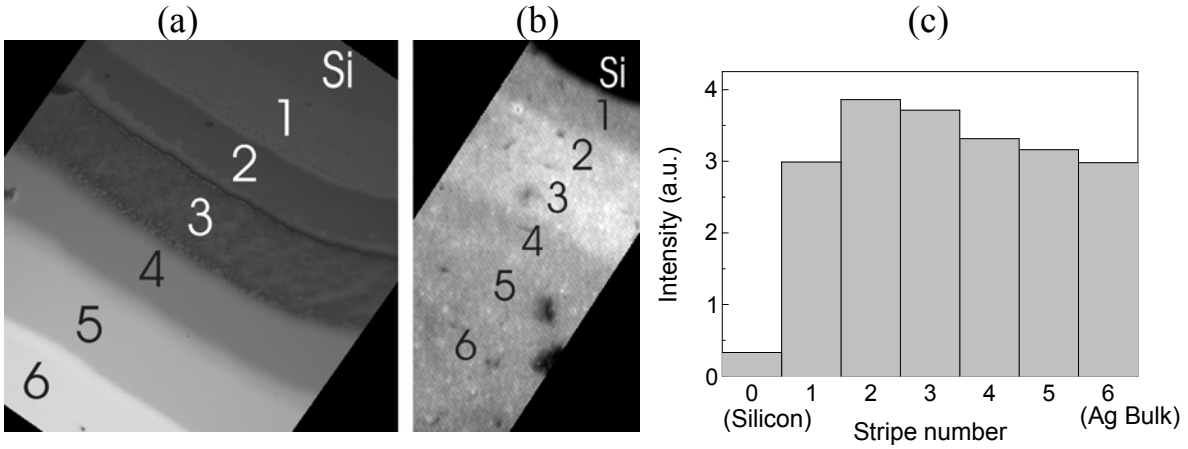

Figure 3.31: (a) Optical image showing the stepped wedge of the Ag/Si sample; (b) PEEM image under UV excitation; (c) UV-PEEM emission intensity from the regions shown in (b).

The Ag nanoparticle film looks essentially different in the electron emission images upon excitation with UV radiation or femtosecond laser pulses. In particular region 6 (the continuous Ag film) appears bright in the UV (Fig. 3.31b) but dark in the laser-excited PEEM images (Fig. 3.32). The cluster films (stripes 1-3) emit stronger under 375-425 nm excitation (Fig. 3.32a-e), while the island films (stripes 4 and 5) emit more effectively under 750-850 nm excitation (Fig. 3.32f-j). Small regions of strongly enhanced electron emission, so called ″hot-spots″ are observed on stripe 4 and a few also on stripe 5. They are excited most strongly with 750nm wavelength. With increasing wavelength (800-850 nm) the ″hot spots″ in stripe 4 disappear and the intensity in stripe 5 increases along with the appearance of a hot-spot-like granular structure (brightest part in (i) and (j)). Note that in this film no ″hot spots″ occur upon excitation with the blue beam. The photoemission intensity shifts to larger wavelengths (i.e. lower frequencies) with decreasing particles size for 375-425 nm excitation (cf. Fig. 3.32a,e). This redshift is opposite to the blueshift that is seen for the 750-800 nm laser excitation. In the latter case the maximum of the electron emission shifts to the stripes with lower Ag coverage when the laser frequency is increased (cf. Fig. 3.32f,j). It is known that metal nanoparticles and nanostructures are able to build up structural resonances of the collective oscillation of the metal's electron plasma, usually called localized surface plasmons (LSP). Due to the confinement of the electrons in the metal structures (dielectric confinement), surface charges cause restoring forces when the plasma is driven by the incident photon field and this leads to resonances.

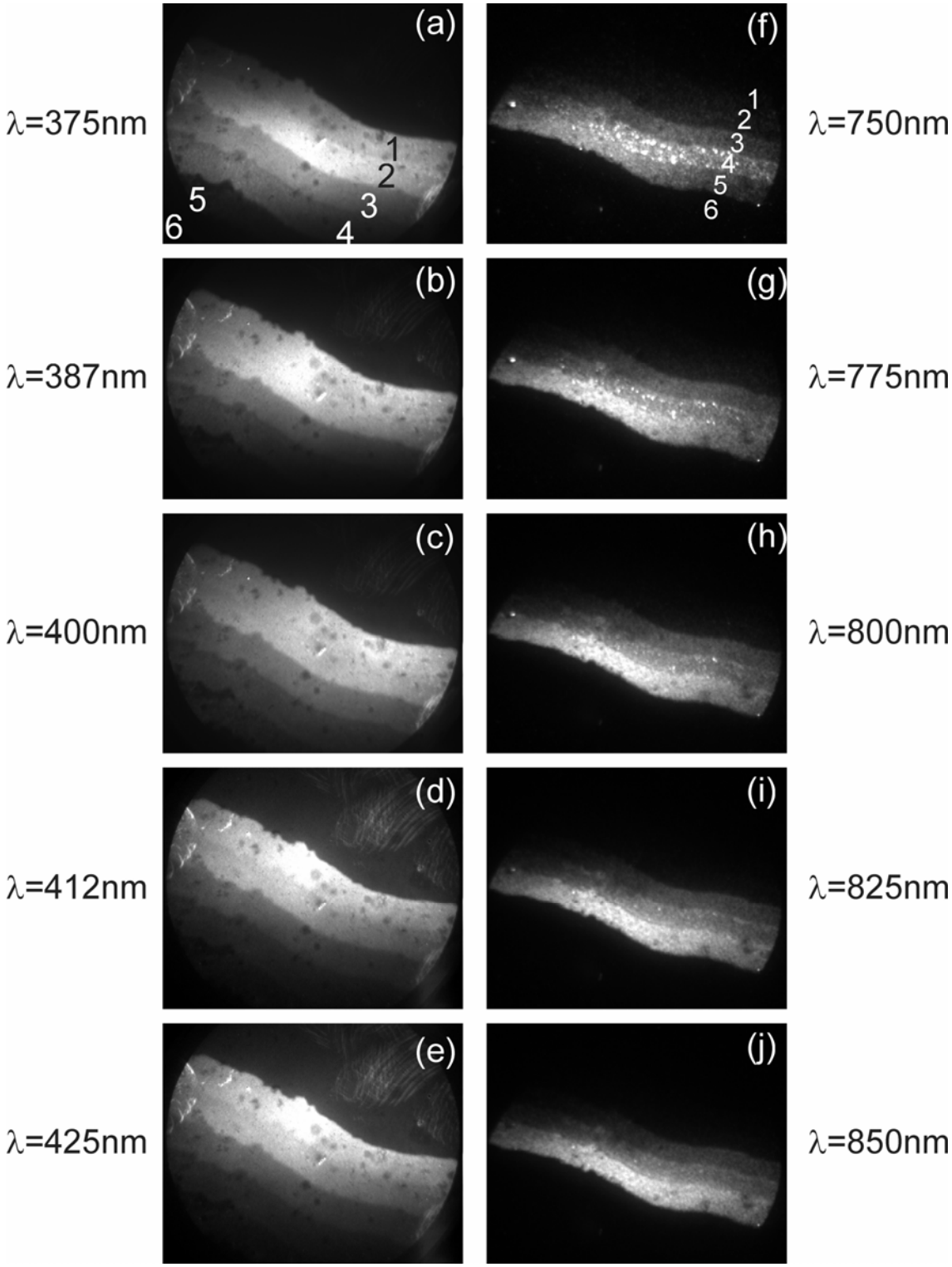

Figure 3.32: Dependence of the fs-laser excited PEEM images on the wavelength. The field of view is slightly different in series (a–e) and (f–j).

The theoretical LSP resonance frequency for silver is $\omega_p / \sqrt{2 + \mathrm{Re}\,\varepsilon_d} \approx 3.5\,\mathrm{eV}/\hbar$ (354 nm) [Lie93]. It is a screened plasma frequency i.e. all possible collective effects, like

screening of the quasi-free electrons by the bound d-electrons, are considered. Of course, this value may shift for many reasons, like size, shape, surrounding media, coupling of neighboring particles, etc. Producing nanoparticles of different sizes and shapes, lying in an array, one can tune the resonance frequency of the LSP in a wide wavelength range of the visible light. For explanation we show two results from literature, the first from Scharte et. al. Here, elliptical nanoparticles 40 nm x 80 nm have been produced by electron-beam-lithography (Fig. 3.33a), which show two different resonances. It is visible in the extinction spectrum (Fig. 3.33b): $\hbar\omega_1$ = 2.1 eV (590 nm) and $\hbar\omega_2$ = 2.9 eV (427 nm). Both peaks have a FWHM of about 0.4 eV (113 nm and 58 nm, respectively).

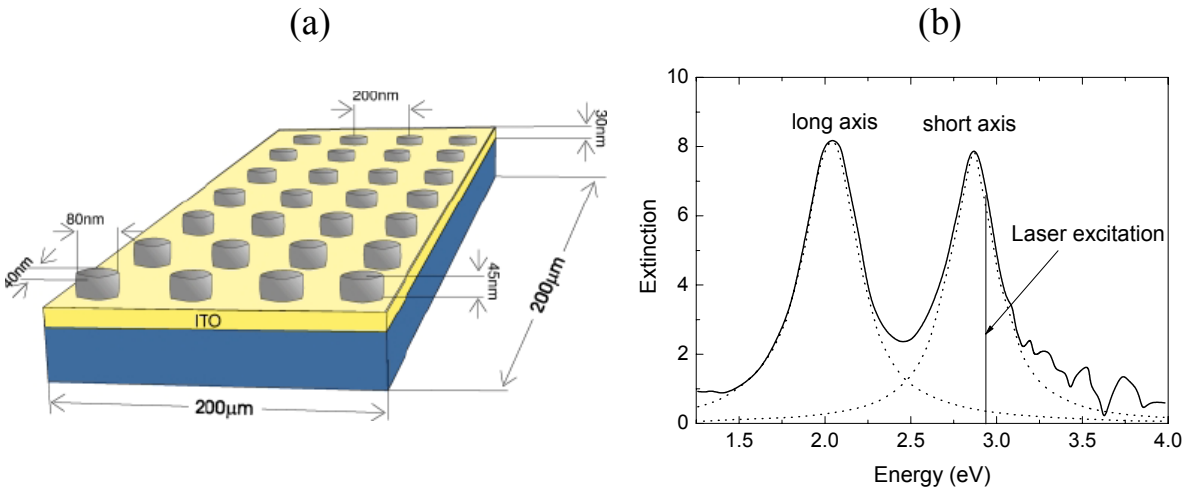

Figure 3.33: (a) Array of Ag nanoparticles deposited on an ITO substrate. (b) Measured extinction spectrum of the nano-particle array. The low- and high-frequency peaks correspond to the localised surface plasmons excited along the long and short axes of the elliptical Ag particles, respectively. (From [Sch01]).

The second literature result (from Gotschy et. al) given in Fig. 3.34a shows that the maximum in the extinction spectrum can lie in the red spectral region. The dependence of the position of the extinction peak on the thickness of the silver film was studied in [Got96]. It was found that the maximum shifts to lower frequencies with increasing film thickness. This perfectly agrees with our results, namely stripe 4 shows the emission maximum at 750 nm, stripe 5 at larger wavelength. The morphology of the films deposited on ITO (Fig. 3.34b) and Si (Fig. 3.30) substrates is quite similar.

Although the size dependence of the plasmon resonance of granular metallic films has been discussed by several authors, it is still not well understood. Numerous theoretical models were proposed and several experiments were carried out to justify the observed peak shift (either blueshift or redshift) and peak broadening with decreasing particles size. Kreibig et al. [Kre85] have summarized the critical dependence of various intrinsic properties of metal particles on size, intercrystalline distance and their integrated effect on the plasma band shape and position. The blueshift with decreasing particle size is attributed to several phenomena via contraction of the lattice induced by surface stress [Cai01], an effect of surface potential [Coc85], changes of optical interband transitions between discrete energy levels, changes of electronic band structure, etc. The redshift is attributed to the spill-

out of the s-electrons in free-electron metals [Hee93], increase in the effective mass of the conduction electrons, etc. Apart from these effects, deviations from perfect spherical shape, and irregular size distribution would profoundly affect the large inhomogeneous broadening [Gan12].

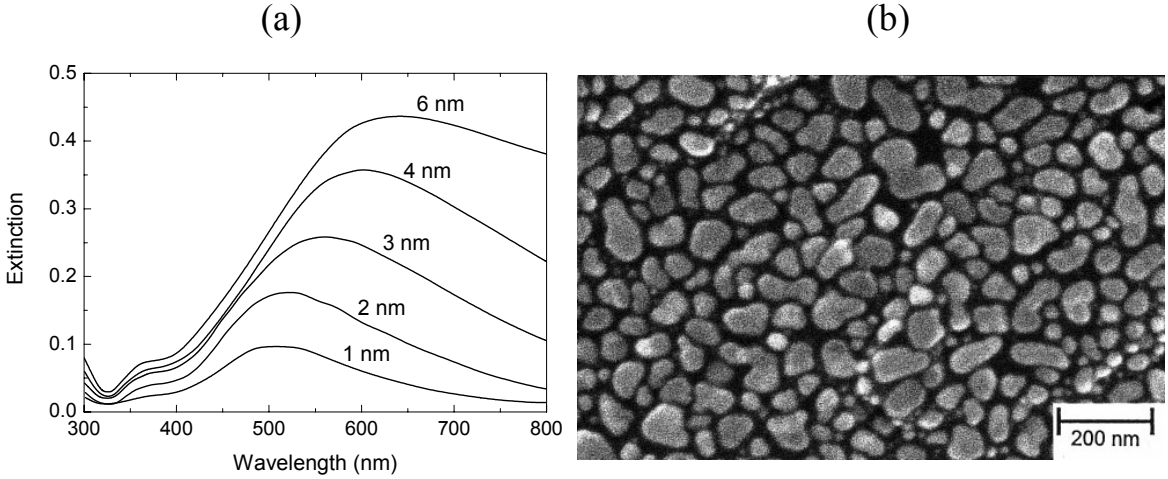

Figure 3.34: (a) Extinction spectra of conventionally grown silver island films on an ITO substrate. Deposited mass thickness as a parameter. (b) SEM picture showing the morphology at a mass thickness of 4 nm. (From [Got96]).

The emission intensity distribution from the thick silver film (100 nm) shows a strong dependence on the wavelength and polarization of the laser. When p-polarized light is used (electric vector has a component perpendicular to the substrate) the emission pattern is rather homogeneous (Fig. 3.35a). This polarization favours the ″normal″ photoemission yield. When the non-favourable s-polarization is used, the image is much darker and very inhomogeneous, i.e. strong ″hot-spots″ occur (b). This polarization behavior was first observed by O. Schmidt [Sch00, Fec02] Under 800 nm excitation (c) the image consists of ″hot spots″ only. Note, that the position of the ″hot spots″ do not coincide in (b) and (c), taken at different wavelengths. This confirms the suggestion [Sha96] that ″hot spots″ are surface inhomogenities like tips, cracks etc. which can be resonantly excited by certain, i.e. individual optical wavelengths.

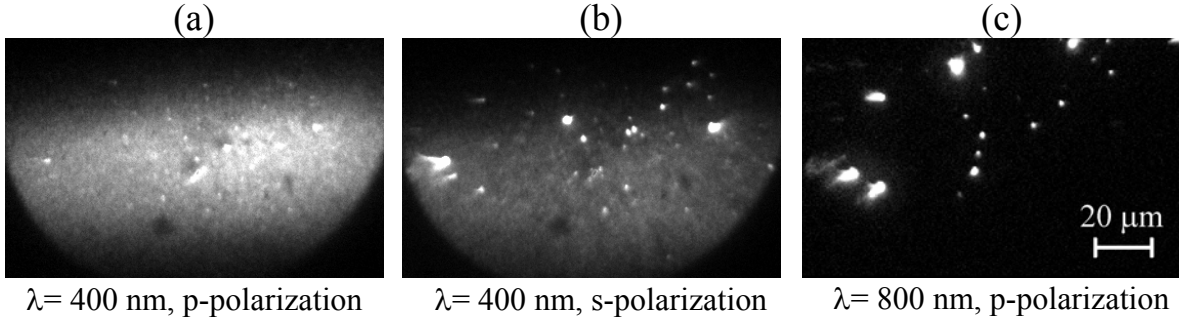

Figure 3.35: PEEM images taken from the same area of bulk silver excited with (a) p- and (b) s- polarized 400 nm and (c) p-polarized 800 nm laser radiation. The magnification and sample position (field of view) are identical.

3.2.2.3 Dependence on laser power

Studies of the photoemission intensity dependence on the power of the laser beam have been performed to shine light into the electron emission mechanisms. Using the 400 nm beam the power range (20-120 mW) was not sufficient to access different emission regimes. The power law for ″hot spots″ and homogeneous areas was the same for both p- and s-polarizations. All measured curves of the power dependence of the photoemission have the same slope close to 2, what was expected for two-photon photoemission at 400 nm laser excitation. Fig. 3.36 shows a typical example.

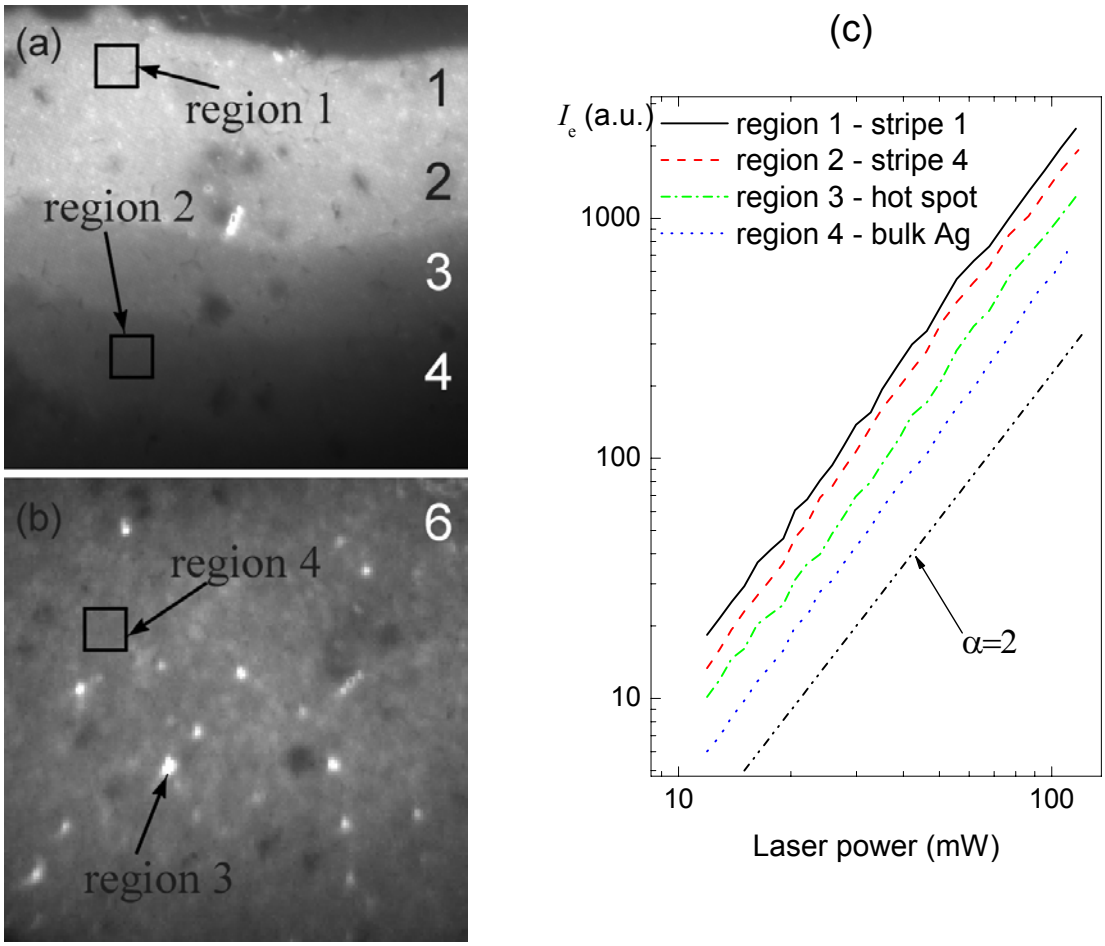

Figure 3.36: (a) PEEM image of the stepped wedge under 400 nm excitation. (b) PEEM image of the bulk silver film under 400 nm excitation. (c) Dependence of the emitted electron current on laser intensity (at 400 nm) from stripe 1 (full line), stripe 4 (dashed line), bulk silver (dotted line) and a ″hot-spot″ on the bulk silver layer (dash-dotted line). A line with a slope α=2 corresponding to exponent of 2 is drawn as a dash-dot-dot line.

The results obtained for excitation by the 800 nm beam look different, see Fig. 3.37. These results have been taken for a 100 nm thick bulk layer of Ag. At intermediate powers (45-80 mW) the slope of the electron emission intensity curve is close to 3 (dotted line). This is the expected result for three-photon photoemission. The total energy of $3h\nu = 4.65\,\mathrm{eV}$ exceeds the work function threshold (cf. thresholds visible as left cut-off in

Figs. 3.39-3.41). In the range 80-250 mW the photoemission intensity rises with a slope of about 3.7 (dashed line) i.e. it does not obey an integer power law. This gives evidence of thermally-assisted multiphoton photoemission (see chapter 1.3.3). Most likely, the ″hot spots″ are originating from very small regions (less than 100 nm) with a high absorption coefficient for 800 nm radiation. The electron subsystem is very hot during the laser pulse that creates more initial states that can contribute to 3PPE. Obviously this mechanism can not be realized in bulk material. Therefore, the emission signal from the smooth silver surface is negligible in comparison with the signal that comes from the ″hot spots″. The deviation from the $I_e \propto I_L^{3.7}$ dependence starts at about 250mW (photon field amplitude E = $9.5 \cdot 10^5$ V/cm) due to the increasing probability of the optical field emission mechanism. The transition interval $\omega\sqrt{2m\phi}/en < E < \omega\sqrt{2m\phi}/e$ between these mechanisms should be expected at about $E \approx 2.8 \cdot 10^7$ V/cm or $J \approx 1000$ GW/cm^2 for bulk silver (ϕ=4.8eV). On rough surfaces the transition can occur at much (few orders of magnitude) lower powers due to the plasmon-mediated field enhancement on them as discussed theoretically [Mes81] and observed recently by us on Ag nanoparticles [Cin04, Cin05].

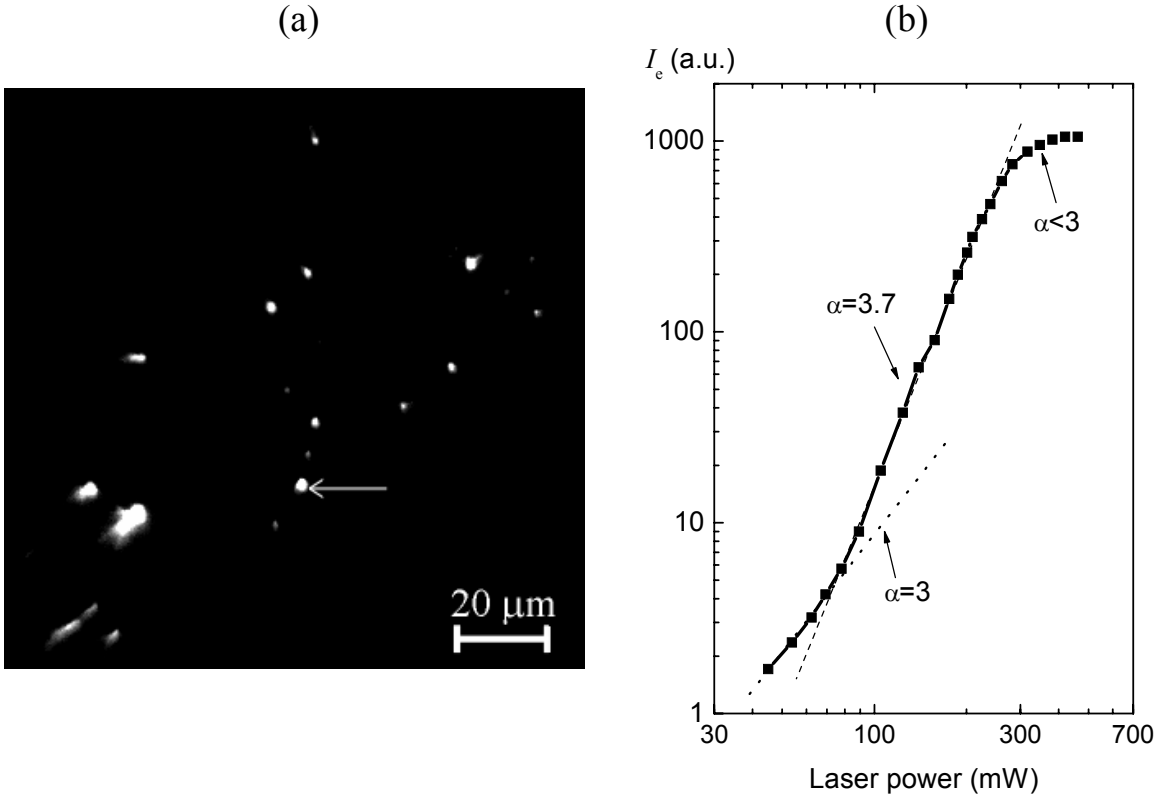

Figure 3.37: (a) PEEM image of a bulk silver film under 800 nm excitation. The arrow shows the ″hot spot″ whose emission dependence on laser power is presented in (b). (b) Dependence of the emitted electron current on laser intensity (at 800 nm) from a ″hot spot″ on the thick silver layer. The full curve connects the experimental points, the dotted and dashed lines denote slopes of α=3.0 and 3.7 respectively.

The same behavior was also observed for silver island films, see Fig. 3.38. Stripe 5 (region 2) exhibits an exponent of $\alpha_2 \approx 2.9$, i.e. close to the expected exponent for 3PPE. The

reason, why exponents can be *smaller* than the integer value expected, is explained below in the context of fig. 3.40. However, the exponent of the ″hot spot″ photocurrent $\alpha_1 \approx 3.2$ is significantly higher than that of stripe 5 due to the more effective heating of the electron subsystem in the ″hot spots″ during the laser pulse. Like in Fig. 3.37 the field emission mechanism becomes apparent at ≥ 300 mW ($E = 10^6$ V/cm) for a ″hot spot″ and at a slightly higher value for the stripe 5. This reflects the more effective absorption of laser power by the ″hot spot″ due to the resonant excitation.

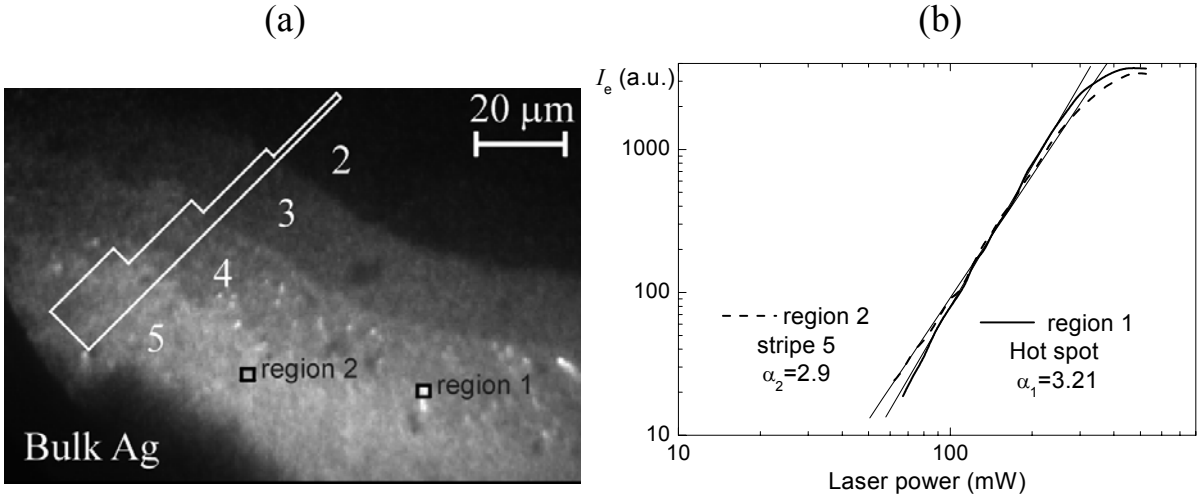

Figure 3.38: (a) PEEM image of a stepped silver wedge under fs-laser excitation at 800nm. (b) Dependence of the photocurrent I_e on the power of the laser beam for two different areas of interest marked in (a).

3.2.2.4 Microspectroscopy of the emitted electrons

In order to investigate the electron energy distribution curves in view of the proposed emission mechanisms, microspectroscopy was performed. Fig. 3.39 shows spectra recorded from stripe 2 under excitation with different wavelengths. The PEEM was operated in combination with the retarding-field imaging energy filter. The spectrum from bulk silver taken at 400 nm excitation (3.1 eV) is plotted for comparison. All spectra were normalized to the maximum intensity value close to the low-energy cut-off. The intensity for stripe 2 was approximately 22 times higher than that for bulk silver. The low-energy cut-off of the cluster spectra is shifted towards lower final energy values as compared to bulk silver, see also [Cin04]. This reflects the fact that the work function of silver clusters is approximately 0.3 eV lower than that of bulk silver. It can be explained by the decrease of the mirror charge potential for a neutral metal sphere with radius r by the value of $\frac{5}{8}\frac{e^2}{r} = \frac{0.90}{r[nm]} eV$ [Woo81]. This work function reduction is considerable in the size range of $2r$=2-15 nm. The mean size of the silver clusters from stripe 2 (see Table. 3.1) lies exactly in this range. For still lower sizes the work function increases again due to quantum-size effects approaching ″molecular″ ionization potentials. The spectrum from bulk silver exhibits a feature at approximately 5.1 eV. This shoulder arises from a direct interband transition within the free-electron like sp-band in the surface normal direction [Paw98]. A

striking result is the absence of this feature in all spectra from silver clusters. This is strong evidence of the fact that the missing long-range order leads to deviations in photoemission dynamics. In small particles the electron confinement and, as we have seen in section 3.2.1.1, the multiple twinning inducing a pattern of grain boundaries, modifies the band states (Bloch states). As a second fact, the broken translational symmetry gives rise to umklapp-processes that are not possible in 3D crystals [Sha96].

The Fermi level onset in the spectra shifts by $2\Delta h\nu$ when the quantum energy is varied. This is in full agreement with the concept of pure 2PPE. The spectra differ in their high-energy part only. This can be seen from the comparison of spectra taken at excitation energies 3.1 and 2.9 eV. They are similar in the range of final state energies up to 5.5 eV. The intensity of the high-energy part (4.5-6.5 eV) of the spectrum recorded at $h\nu$= 3.3 eV appears lower than for the lower quantum energies used. This observation can be explained analyzing the dependence of the spectra on the power of the laser beam (Fig. 3.40). One can see that for both quantum energies an increase of the laser beam power leads to a stronger intensity increase in the high-energy part of the spectrum. Since the maximal power of the laser beam with quantum energy 3.3 eV in Fig. 3.39 was only 19 mW it becomes clear why the ratio $I_{\text{cut-off}}/I_{\text{high-energy}}$ is slightly increased for the 3.3 eV-curve.

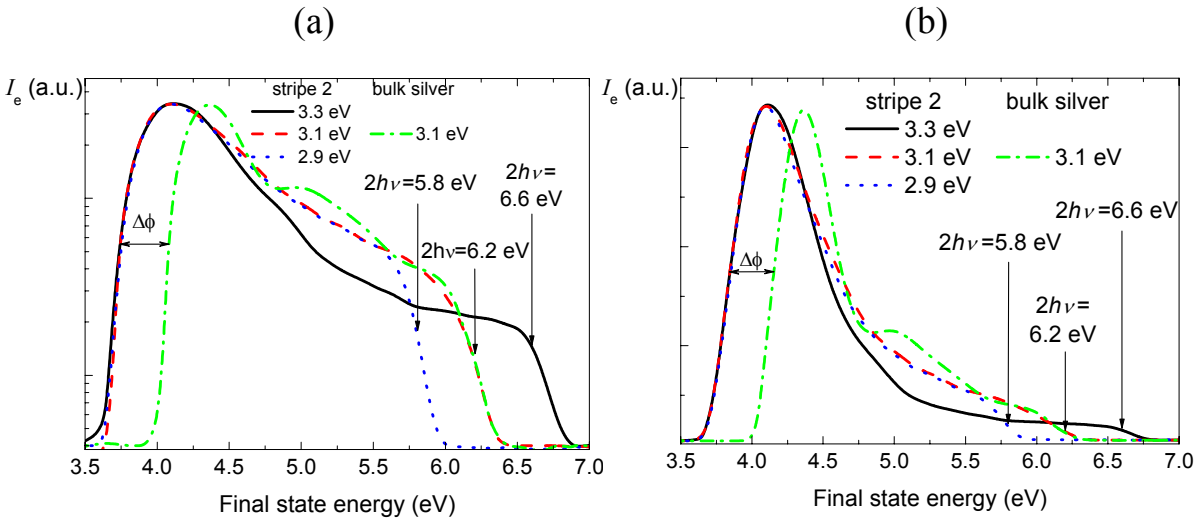

Figure 3.39: (a) Photoelectron spectra (intensity on a log scale) plotted as function of the electron final-state energy for stripe 2 (see Figs. 3.30 and 3.32) taken with femtosecond laser illumination at $h\nu$ = 2.9, 3.1 and 3.3 eV. Laser beam power was 70, 70 and 19 mW, respectively. The spectrum of bulk silver (dash-dotted) illuminated by 3.1 eV photon energy was expanded by a factor of 22. The expected Fermi level onsets at 2hν for 2PPE are marked with arrows. (b) The same plotted on a linear scale.

The result shown in Fig. 3.40 sheds further light on the nature of the emission processes and on the fractional exponents observed for the total emission intensity. The spectra were measured at two laser powers (50 and 10 mW) for two photon energies (2.9 and 3.1 eV for (a) and (c), respectively). The intensities have been normalized at their maximum at 4.1 eV final state energy (the absolute intensities were not exactly known in these spectra). Clearly, the two spectra at different laser power are not identical. The lower curves (b) and (d) show the spectral intensity ratios of the 50 mW and 10 mW spectra. Both ratio curves display maxima at 5.4 eV final state energy. At a photon energy of 3.1 eV the ratio reaches almost

2, i.e. the intensity gain close to the Fermi energy is a factor of two higher than the gain close to the low-energy cut-off. This finding can only be explained by a *coexistence of different emission mechanisms with different spectral characteristics*. It is clear that the region close to ε_F reflects pure 2PPE, characterized by n=2. Obviously, this value drops to about n=1 in the maximum of the spectrum close to the low-energy cut-off. As n=1 corresponds to common 1-photon photoemission, this points to thermally-assisted nPPE from the non-Fermi-Dirac high energy tail of the transient electron distribution between ε_F and ε_{vac}.

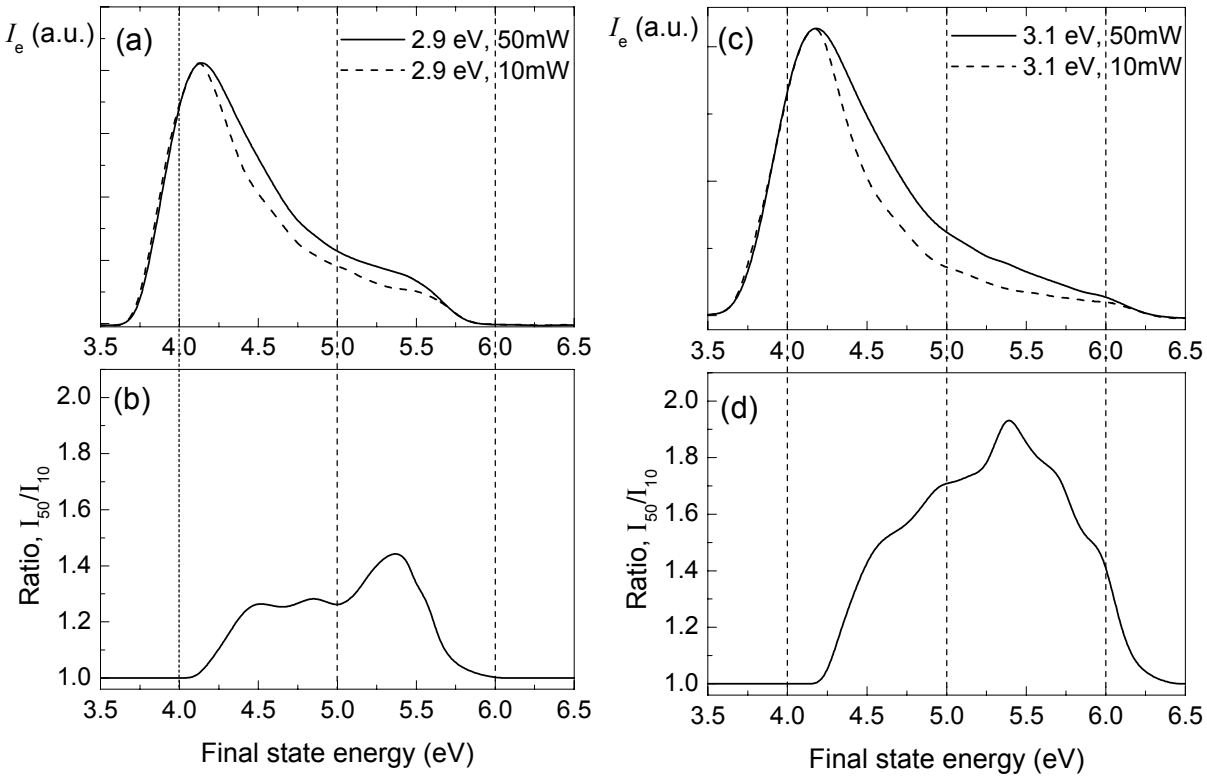

Figure 3.40: Photoelectron spectra taken under different laser beam powers at (a) $h\nu$ = 2.9 eV and (c) 3.1 eV. The ratio of the intensity spectra at 50 mW and 10 mW are shown in (b) and (d), the spectra have been first normalised in the maximum.

Photoemission spectra recorded under excitation at 750-850 nm are shown in Fig. 3.41 for stripe 5, see Fig. 3.32f-j. The total electron yield was a factor of 35-50 smaller than under 375-425 nm laser excitation, referred to the same average power. To explain this disagreement with results described in the previous section we have to recall the dependence of the photoemission intensity on the width of the exciting pulse (Fig. 3.26). The photoemission yield decreases by 2 orders of magnitude when the pulse width of laser system 1 is increased from its minimal value of 18 to 100 fs. Note that the minimal pulse width of laser system 2 used for the PEEM studies is 100 fs (see Table 2.1). Since for ″red″ laser excitation at least 3 photons are necessary to bring an electron above the vacuum level, the photoemission yield is more sensitive to the time delay between subsequent absorption of photons than in the case of ″blue″ laser excitation.

Spectra are broadened apparently only by 2-2.5$\Delta h\nu$ when increasing the 750-850 nm laser frequency what is not fully consistent with a pure 3PPE mechanism. However, the Fermi level onset appears significantly smeared out in spectra taken under ″red″ laser excitation, see right cut-offs in Fig. 3.41b. This may be attributed to additional broadening of the Fermi edge and is most likely a fingerprint of a transient ″hot electron″ gas in the particle. Regarding the 3PPE process as a sequential transition, the third photon finds the ″hot electron″ not in the nascent state after the 2-photon excitation but rather in a partly thermalised state. Using the method described in [Fan92b] it is possible to estimate the transient electron energy distribution and the corresponding transient electron temperature by fitting the Fermi level onset by a Fermi-Dirac function. The maximal value of electron temperature was estimated to be approximately 1870 K for 1.65 eV excitation (full curve). It is important, however, to keep in mind that this is only an approximate value because the 100 fs pulse averages over the non-Fermi-Dirac distribution (see Rethfeld plots in section 1.1) and a Fermi-Dirac-like transient state at the end of the pulse.

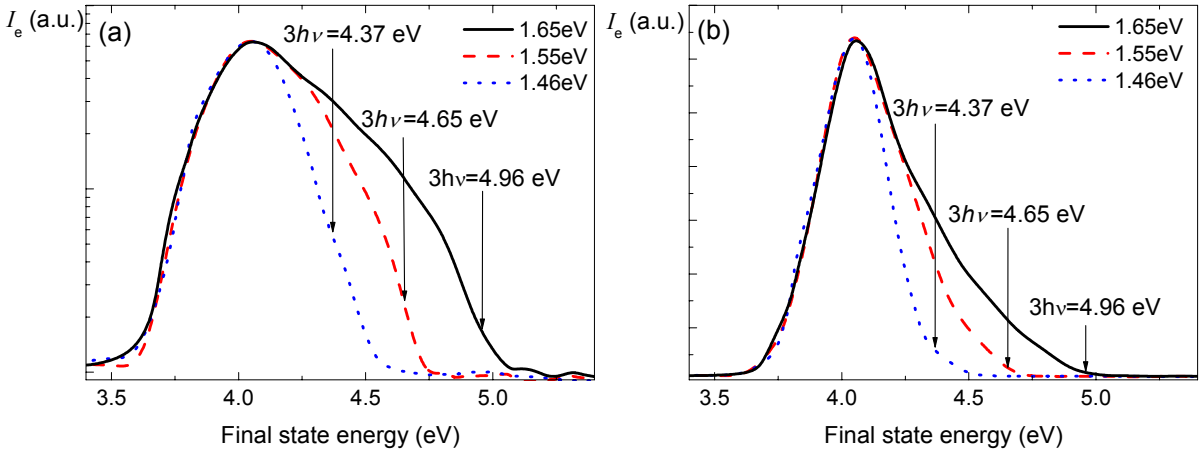

Figure 3.41: (a) Photoelectron spectra plotted on a log scale as function of the electron final-state energy for stripe 5 (see Fig. 3.32) taken with femtosecond laser illumination at $h\nu$ = 1.46, 1.55 and 1.65 eV. Laser beam power was 700 mW for all three quantum energies. The expected Fermi level onsets for 3PPE are marked with arrows. (b) The same plotted on a linear scale.

In this section we have shown by means of microspectroscopy that photoemission patterns and intensity from silver nanoparticle films strongly depend on laser wavelength and polarization. The transient “hot” (non-Fermi-Dirac) electron gas confined in small clusters may cause possible changes in the optical constants, absorption coefficients and parameters in the Richardson-Dushman equation. Plasmon-mediated *n*PPE is special because the localized surface plasmon enhances the brightness in PEEM due to the near-field [Cin05] and “saves” photons for several fs leading to a high concentration of electromagnetic energy in nanometer-sized clusters. Finally, optical field emission may occur at very high laser power (more precisely, local photon flux density).

The cluster films (stripes 1-3) emit more effectively under 400 nm excitation, while the island films (stripes 4 and 5) – under 800 nm excitation. ″Hot spots″ were found on the

closed silver film and the 4th stripe. On the island film they can be resonantly excited with λ=750 nm.

We have confirmed the 2PPE emission mechanism from silver thin films under 400 nm excitation. For excitation at $h\nu$=750-850 nm the local intensity vs laser power curves show different regimes with different non-integer slopes The Fermi level onset is rather sharp (less than 150 meV wide) and shifts by $2h\nu$ when the quantum energy is increased, while it is significantly smeared out under 800 nm excitation. This gives evidence of the existence of a transient ″hot-electron″ gas in the particles.

Spectra taken in the 400 nm region with different average laser powers exhibit clear differences. The region near the Fermi edge is characterized by the n=2 power law of true 2PPE, whereas towards the low-energy cut-off the power dependence is considerably weaker. This is a clear proof of the coexistence of different emission mechanisms in one spectrum and explains works [Fec02, Sch00].

3.3. Size-selective time-of-flight spectromicroscopy of MoS_2 nanotubes

In this section we present results of photoemission microspectroscopy of single MoS_2 nanotubes deposited on a Si surface. The photoelectrons were excited by a frequency doubled fs laser oscillator (Laser 2, Table 2.1) resulting in pure two-photon photoemission at $h\nu$=3.1 eV. A novel spectro-microscopic technique based on imaging time-of-flight detection was used to record the spatially resolved photoelectron spectra. Self consistent electronic structure calculations for MoS_2 slabs using the full potential linear augmented plane wave method (FLAPW) are used to explain the peculiarities of the observed spectra. It turns out that the MoS_2 nanotubes are semiconducting with a band gap of about 1 eV. The two-photon transitions proceed through intermediate states in a region with high density of states; this gives rise to a high photoemission intensity.

Carbon fullerenes and carbon nanotubes (NT) constitute an important class of materials with wide potential applications. In analogy, their inorganic counterparts based on early transition metal chalcogenides were reported and characterized by Tenne et al. since 1992 [Ten92]. As these chalcogenide nanoparticles are chemically inert and stable at temperatures up to 300°C, they have shown promise for practical use, e.g. as solid lubricants. Furthermore, MS_2 (M – transition metal) nanotubes display a number of intriguing and partly size-dependent [Sei00] electronic, optical and magnetic properties [Mih03] that make them promising materials e.g. as probes for scanning probe techniques. Therefore, they are attractive systems to study in the context of "structure-property relationships" in nanomaterials. Although a number of theoretical studies on chalcogenide nanotubes have been performed [Sei00, Iva04, Bol02], experimental results concerning the electronic structure of these materials are scarce [Sch02b, Rem03, Zim04, Coe87]. Only NT-WS_2 and NT-$MoS_{2-x}I_y$ were studied experimentally [Sch02b, Rem03]. $MoS_{2-x}I_y$ showed metallic behavior in scanning tunneling microscopy. For WS_2, an indirect band gap of 1.3 eV was found at room temperature. The band gap increased with increasing tube diameter. Semiconducting behavior was predicted for MoS_2, with a band gap between some meV and 1 eV depending on the size and structure [Sei00]. There is, however, no other experimental evidence available confirming the size of the gap or the semi-conducting behavior nor any other study of an individual chalcogenide nanotube.

3.3.1 Sample preparation and characterization

MoS_2 nanotubes were synthesized using silica nanotubes as template. Diammonium thiomolybdate in dimethyl formamide was heated with the templates under constant stirring, dried, and reduced in a H_2/N_2 gas stream at 450°C. Finally, the template was dissolved in HF. Transmission electron microscopy (TEM) and High-resolution transmission electron Microscopy (HRTEM) images of the MoS_2 NTs are shown in Fig. 3.42. The line scan of the energy-dispersive X-ray spectroscopy (EDX) signal in Fig. 3.42a reveals that the nanotubes are hollow cylinders with 20-30nm wall thickness, an inner diameter of 120 nm and a length of several micrometers.

The study of chemical composition of a separate nanotube was carried out with the help of the energy dispersive X-ray (EDX) detector implemented in the transmission electron microscope. For these measurements, the electron beam was focused on the sample in a region with a lateral size of 1 nm. The region, from which X-ray radiation was analyzed, was somewhat larger (it increases as the sample thickness increases, in the present case as the nanotube wall thickness increases). The EDX analysis reveals the signal from the nanotube constituents Mo and S (Fig. 3.43a). The energy resolution (100 eV) did not allow to distinguish the signal coming from Mo L_α (2.293 keV) and S K_α (2.307 keV) edges. The peak at about 17.5 keV is a signal from the Mo K_α edge (17.479 keV). Fig. 3.43b shows the intensity profile of the EDX signal from the Mo L_α and S K_α (area under the spectrum in the energy range from 2100 to 2500 eV in Fig. 3.43a) along the line AB in Fig. 3.42a. The signal profile verifies that the nanotubes are hollow cylinders, because this profile is characterized by two maxima. The signal increases when the electron beam touches the tube walls and decreases, but not to the zero level, when the electron beam is directed towards the tube axis.

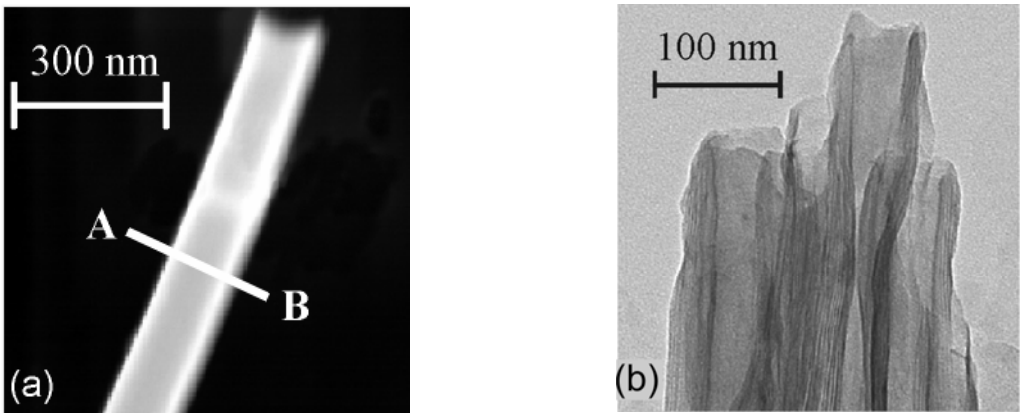

Figure 3.42: TEM (a) and HRTEM image (b) of MoS_2 nanotubes

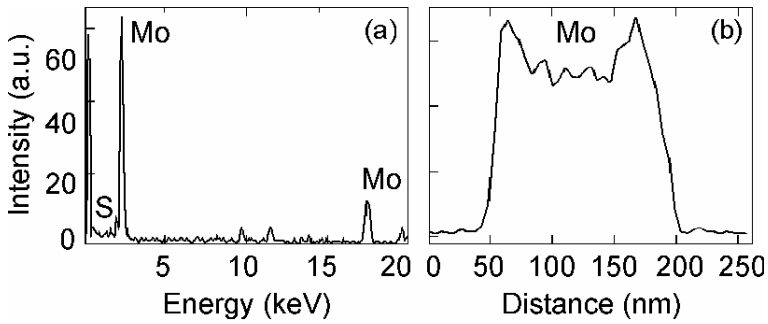

Figure 3.43: (a) Energy dispersive X-ray spectrum of an area of about 1 nm on a nanotube. (b) Intensity line scan of the Mo L_α (2.293 keV) and S K_α (2.307 eV) signal in (a) along the line AB denoted in the Fig.3.42a.

For the PEEM studies, the MoS_2 nanotubes were dissolved in ethanol and deposited on the clean and smooth surface of a Si-wafer covered by native oxide (SiO_x surface). The coverage was chosen to be low enough that individual nanotubes could be identified and localized in the PEEM images. To minimize the influence of the impurity traces on the spectral features the samples were cleaned by non-destructive mild sputtering (Ar+, 700 eV, 5 min) directly before the measurements.

3.3.2 Results

The PEEM operated in the TOF-mode (see section 2.2.1) was used to visualize single NTs. An initial attempt to study individual, size-selected NTs using vacuum UV (VUV) excitation (He I, photon energy 21.2 eV) failed, because individual NTs were indiscernible on the background signal from the Si substrate. The images indicated that the NTs appeared dark on the background. This made it impossible to obtain a clear photoemission signal from the NTs. In particular, the question about the size of the gap could not be addressed using VUV excitation. This failure led us to the use of near-threshold excitation using a femtosecond laser source and a 2PPE transition.

The NTs appear very bright on a dark background if excited with 3.1 eV fs-laser radiation (Fig. 3.44). The high intensity contrast between nanotubes and Si substrate was a very positive result and was not anticipated after the failure with VUV excitation. It is explained by the nature of the two-photon transition induced by the fs-laser. The work function of the deposited NTs is higher than the photon energy. Hence, single-photon photoemission is energetically impossible. An important factor for the high intensity is most likely the high density of states in the intermediate state of the two-photon transition, revealed by electronic structure calculations, see below. This, in turn, leads to an enhancement of the matrix element of two-photon transitions. The signal forming the image in Fig. 3.44 thus results from two-photon transitions characterized by a total energy transfer of $2h\nu = 6.2$ eV.

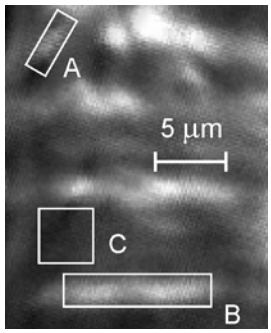

Figure 3.44: PEEM image of a group of MoS_2 nanotubes on SiO_x excited by fs-laser radiation with 3.1 eV photon energy.

Fig. 3.45a-c show spectra extracted from different regions (region A: small NT, B: large NT, C: substrate) of the sample as marked in Fig. 3.44. The time-of-flight spectra have been translated into energy spectra using Eq. (2.1). The energy scale of the spectra is referenced to

the top of the valence band becoming visible at an energy of about 6.2 eV (i.e. 2*hv)*. The local work function of the micro areas results in different low-energy cut-offs of the spectra. The work function of the substrate is determined to be 4.2 eV (spectrum (c), open circle), whereas the value of the NTs (spectra (a) and (b), full circles) is lower by $\Delta\phi = 0.3$ eV.

The NT spectra show a width of 2.3 eV, thus allowing to study the topmost region of the valence states. The Si-spectrum (c) (weighted by an empirical scaling factor) was subtracted from the NT spectrum (b) to account for the background emerging from the Si substrate. The result is shown as spectrum (d).

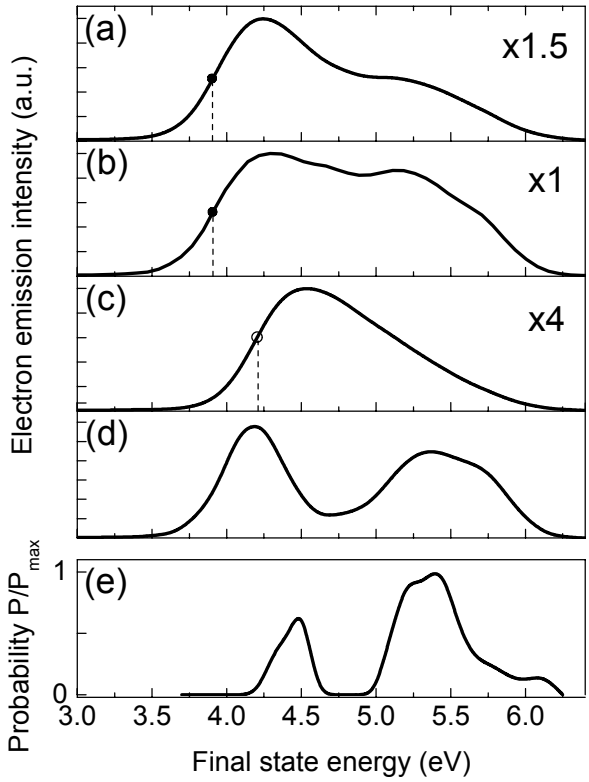

Figure 3.45: Local spectra of selected nanotubes ((a) and (b) corresponding to regions A and B in Fig. 3.44) and the Si substrate (c, region C). Spectrum (b) after background correction is shown in (d). The probability for direct transitions (e) at the excitation with 3.1eV photons was derived from the calculated density of states.

3.3.3 DOS calculations

Electronic structure calculations were performed in order to explain peculiarities of the spectra. The limiting case of a NT with infinite diameter is a single slab, therefore slab calculations were used to estimate the electronic structure of the NT. This assumption is supported by calculations for TiS_2 by Ivanovskaya and Seifert [Iva04] showing that the density of states (DOS) in various NTs is very similar to that of the slab. Bulk MoS_2 exhibits already a layer type structure and it showed up that the difference in the DOS between slabs and bulk material is also not very pronounced. The full potential Wien2k code [Bla01] was used to perform the slab calculations. The generalized gradient approximation was used for the parameterization of the exchange-correlation potential. This accounts better for correlations compared to pure LDA-potentials, in particular if dealing with semiconducting materials. The

calculations were performed for $P\bar{3}m1$ symmetry and the separation between the slabs was set to 4 nm. It was tested carefully by varying the separation that the slabs are electronically decoupled from each other. 650 irreducible k-points (out of 7200) in the Brillouin zone were used for the final k-space integration.

The results of the calculation are shown in Fig. 3.46. The band structure for a MoS_2 slab agrees with the one obtained by Coehorn et al. for bulk material [Coe87]. The calculation reveals the slabs to be semi-conducting with a band gap of about 1 eV, being comparable to bulk material. The band structure may not be directly comparable to a NT as this has 1-dimensional symmetry whereas the slab has 2-dimensional symmetry. In the limit of large diameter tubes, however, the DOS should be comparable [Iva04]. Our tubes have a relatively large outer diameter of 150 nm. The DOS may also be better for comparison with the observed spectra, as it is already an integrated quantity. One possible two-photon transition is indicated in Fig. 3.46b by arrows. The DOS exhibits a pronounced maximum at about 1 eV below the valence band maximum (ε_{VB-max}). The maximum in the unoccupied DOS at about 2 eV will serve as a very effective intermediate state for the two-photon process such that a coherent excitation is possible. This leads to much higher intensities compared to two-photon transitions through virtual intermediate states as often observed in metals with a very low DOS in the unoccupied part of their band structures (e.g. Cu or Ag).

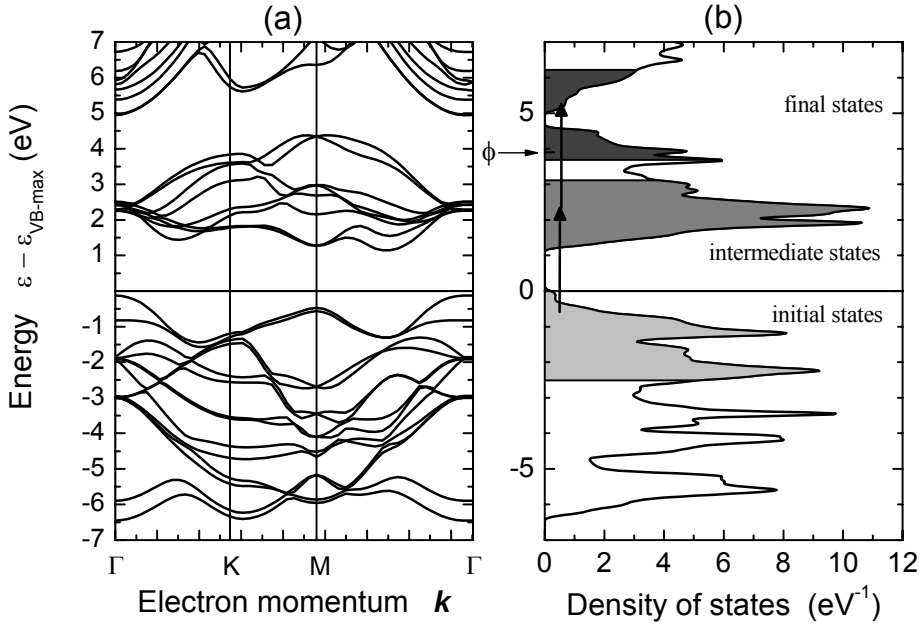

Figure 3.46: Calculated band structure (a) and density of states (b) of a MoS_2 slab. The arrows denote one possible two-photon transition induced by femtosecond laser radiation of 3.1 eV. The shaded areas assign the ranges that are energetically allowed to take part in the two-photon excitation. ϕ denotes the work function threshold. (Courtesy G.H. Fecher for running the program).

3.3.4 Discussion and conclusions

According to the calculation, there are certain regions where no direct 2PPE transitions can occur. Due to the gap in the intermediate state DOS, there are no direct transitions possible into states below 4.2 eV final state energy. The gap in the final state DOS prevents direct transitions into states between 4.7 eV and 5.2 eV. The probability for direct transitions

may be estimated from a convolution of the DOS in the initial, intermediate, and final states as illustrated in Fig. 3.47a. For simplicity we have not included the transition matrix elements. From the probability in Fig. 3.47b, it is seen that high intensities are expected at final state energies of 4.5 eV and in the range of 5.2 eV to 5.4 eV. The high density in the intermediate state DOS (1.8 eV to 2.3 eV above ε_{VB-max}) may also serve very effectively as base for highly intense indirect transitions at 5.4eV.

The *dipole selection rules*, in particular $\Delta l = \pm 1$, will give an additional weighting factor for the expected intensities as is seen from Fig. 3.47c. The high probability for transitions at about 4 eV is governed by a $p \rightarrow d \rightarrow p$ transition. In the energy range from 5 eV to 5.5 eV the excitation of *p* and *d* valence electrons has nearly equal probability. It should be mentioned, however, that the non-linear excitation may not be described completely by the dipole selection rules. Moreover, the nanotubes are in the region at the surface where the vector potential changes rapidly. Thus one has $\nabla A \neq 0$ allowing for $\Delta l = 0$ transitions, in contrast to the assumptions made usually for pure dipole transitions. Therefore, the intensities from direct transitions are expected to be in between the two cases (b) and (c) shown in Fig. 3.47. In addition, the reduced symmetry of the nanotube will alter the DOS and in particular may give rise to umklapp-processes comparable to the transitions in the metallic nanoparticles. Finally, transitions through virtual intermediate states and into virtual final states can be expected. In particular, these will lead to a finite intensity in the gap around 4.8 eV final state energy, where the experiment shows a minimum with non-zero intensity.

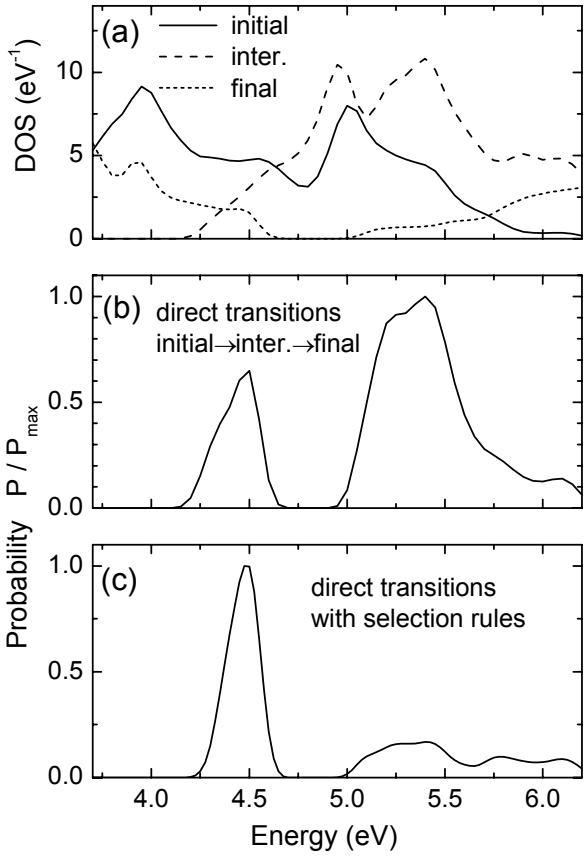

Figure 3.47: (a) The DOS-parts being relevant for direct photo-excitation on an energy scale being shifted by $2h\nu$ and $1h\nu$ for the initial and intermediate DOS, respectively; (b), (c) the

corresponding probability of the transitions without and with application of the dipole selection rules, respectively. The left-hand cut-off is defined by the gap in the intermediate DOS.

The calculated probability of the direct transitions reproduces the measured spectra reasonably well. In particular the position of the gap in the final states is reproduced almost quantitatively (cf. Fig. 3.45d, e). The energetic positions of the maxima at 5.25 eV and 5.75 eV are slightly shifted towards the high energy cut-off, what may arise from the underlying indirect transitions or the influence of the substrate on the NT, compared to a free single NT. The substrate spectrum exhibits no structures at these energies (Fig. 3.45c), thus the observed features clearly originate from the NTs. The NTs in regions A and B of Fig. 3.44 have different sizes and their spectra, in particular the heights of the low-energy peak are different. This peak contains the contribution of secondary electrons as well as the transitions to the low-energy peak (around 4.5 eV) of the probability for direct transitions.

In conclusion, single MoS_2 nanotubes deposited on a Si substrate were investigated by two-photon photoemission microspectroscopy. The nanotube spectra reveal an unexpected, high intensity as compared to the background of the SiO_x surface, whereas they were invisible upon VUV excitation at a photon energy of 21.2 eV. An ab-initio calculation for a MoS_2 slab explains the high intensity in terms of a high density of unoccupied states in the intermediate states of the two-photon photo-transition at $h\nu$ = 3.1 eV. The topmost region of the calculated DOS agrees reasonably well with the measured spectroscopic features. In particular, the convolution of initial, intermediate, and final state DOS shows good agreement with the experiment. A gap in the convoluted DOS at a final state energy of about 4.8 eV above ε_F shows up clearly in the measured spectra, although not with zero intensity. This indicates the significance of the band states in the two-photon photoemission process.

The presented results for MoS_2 NTs demonstrate that the novel time-of-flight based spectro-microscopic method has a high potential for the study of nanoscale materials. A particular challenge will be the study of transient electronic states in pump-probe experiments. A full-field imaging pump-probe experiment without energy filtering has previously been successfully performed [Sch02c].

Conclusions and outlook

In the present work the electron emission from nanoparticles on surfaces has been studied. In particular, metallic nanoclusters generated as self-organized ensembles on silicon or glass substrates as well as a prototype metal-chalcogenide nanotube (MoS_2) deposited on silicon have been investigated. The major part of the performed investigations was focused on the interaction of laser radiation with metallic nanoparticles. As the energy of the electromagnetic radiation is absorbed by the electron subsystem it was interesting to use a femtosecond laser source. Its pulsewidth is comparable with the electron-electron interaction time and much shorter than the electron-phonon interaction time. The energy of the laser quanta was lower than the work function of the studied samples thus excluding common one-photon photoemission. At the beginning of the work it was known from the literature that in this excitation regime the multiphoton photoemission mechanism is responsible for the electron emission from metals. Our investigations showed that going from a continuous metal film to a cluster film another emission mechanism appears competing with multiphoton photoemission and dominates for small metallic nanoparticles.

The nature of the new emission mechanism was investigated by various experiments. The suggestion is made that it is connected with a contribution of the "hot electron" gas to the electron emission. Many important characteristics like dependences of the electron emission intensity on the laser power, wavelength, pulsewidth and time delay between pulses were studied.

In addition, investigations of the electron emission properties under laser excitation were compared with another type of excitation, namely the passage of a tunnelling current through a metal cluster film close to the percolation threshold. This might be interesting for the creation of new efficient nano-scale electron emitters. The obtained results can also be used for the creation of metallic coatings with adjustable emission properties.

The essential experimental and theoretical results are summarized as follows:

1. The *electrical and emission properties of current-carrying silver cluster films* prepared in a small gap (5-25 μm wide) between silver contacts on an insulator was carried out for the first time in an emission electron microscope (EEM). The conduction current-voltage curve is initially linear, but it rises stronger than linear above a certain onset voltage. The electron emission starts in the non-Ohmic region of the conduction current-voltage characteristic of the cluster films. The potential distribution along the metal cluster film was determined from the image distortion in the emission microscope. The voltage drop is higher in the region near the contacts than in the central part of the cluster film. The electron emission is very local, i.e. originates from distinct emission centers. They are formed at certain individual voltage thresholds in the region of the largest electrical field in the cluster film. The apparent sizes of the emission centers were initially about 0.8 μm and increased to several μm upon further increase of the applied voltage. We studied selected, single emission centers in the EEM. It turned out that the emission centers in a current-carrying silver cluster film are point sources of electrons that can provide quite high emission current densities (up to more than 10^2 A/cm^2). The energy spread of the electrons from a single emission center was estimated to be 0.5-0.6 eV. As emission mechanism the thermionic emission from the steady-state "hot electron" gas in the current-carrying metal particles was

proposed. The energy is fed into the emitting nanoparticles by the tunnelling current associated with the voltage drop between adjacent particles.

2. *Integral and spatially resolved studies of electron emission under illumination with fs-laser radiation* were carried out for nanoparticle Ag and Au films grown on glass and silicon substrates. It has been demonstrated that the dependence of the photoemission current on the mass thickness of the Ag film is non-monotonous. The transition from a continuous film to a nanoparticle film is accompanied by an increase in photoemission current by more than an order of magnitude. One can thus determine ranges of the mass thickness where a decrease of the amount of metal leads to an increase of the electron emission intensity. The photoemission intensity grows with decreasing temporal width of the laser pulses (at fixed power), but this dependence becomes less steep as the particles become smaller. Pump-and-probe experiments have shown that with decreasing particle size the electron emission yield decreases more slowly if the time delay between pump and probe pulses is increased.

Experimental results were interpreted in terms of different electron emission mechanisms, i.e. multiphoton photoemission (*n*PPE), thermionic emission or thermally-assisted *n*PPE as well as optical field emission by the high amplitude of the electric vector of the laser beam. The first mechanism prevails for continuous films and particles with sizes above several ten nanometers, the second and third one for films of nanoparticles with sizes of a few nanometers. To excite different emission mechanisms the laser pulse has to be very short (less than 100 fs) and sufficiently intense (average power >700 mW focused into a spot of 100 μm^2). The microspectroscopy measurements have confirmed the 2PPE emission mechanism from thin Ag films under ″blue″ laser excitation (λ=375-425 nm). The Fermi level onset is rather sharp (less than 150 meV wide) and shifts by $2h\nu$ when the quantum energy is increased, while it is smeared out under ″red″ laser excitation (λ=750-850 nm). This is a clear evidence of the contribution of a thermally-assisted electron emission mechanism to the total emission current. It was found that with increasing laser power the yield of low-energy electrons increases weaker with smaller effective exponent than the yield of high-energy electrons. This is a clear proof of the coexistence of different emission mechanisms in one spectrum and explains the puzzling result of non-integer power laws discussed in previous papers in the literature [Fec02, Sch00]. The transient “hot” (non-Fermi-Dirac) electron gas confined in small clusters may cause possible changes in the optical constants, absorption coefficients and parameters in the Richardson-Dushman equation. The optical field emission mechanism becomes apparent on metal cluster films at high laser powers (≥ 300mW) and long wavelengths (750-850 nm).

3. In order to understand theoretically the *size dependence of the emission signals* a statistical approach to the light absorption by small metal particles was derived and discussed. It should be used when the average number of photons absorbed by a particle per pulse is of the order of tenths to several tens. We performed calculations of the absorbed energy distribution over an ensemble of metal nanoparticles and make on this ground a conclusion about the critical particle size where the emission mechanism changes from *n*PPE to thermionic and/or thermally-assisted *n*PPE. According to our estimations the switching point is between $2r = 2$–4 nm, depending on the absorption coefficient and its spectral dependence. This result perfectly agrees with experimental observations.

4. Size-selected single MoS_2 *nanotubes* deposited on a Si substrate were investigated by the time-of-flight based two-photon photoemission spectromicroscopic method upon

fs-laser excitation. The nanotube spectra reveal an unexpected high intensity as compared to the background of the SiO_x-substrate surface, whereas they were invisible upon VUV excitation at $h\nu$ = 21.2 eV. An ab-initio calculation for a MoS_2 slab explains the high intensity in terms of a high density of unoccupied levels in the intermediate state of the two-photon photo-transition at $h\nu$ = 3.1 eV. The topmost region of the calculated DOS agrees reasonably well with the measured spectroscopic features. In particular, the convolution of initial DOS with intermediate and final DOS shows good agreement with the experiment.

Whereas the nanotube spectra and bulk-metal spectra can be perfectly understood in terms of pure two-photon photoemission, the spectra of metal nanoparticles and rough surfaces (showing ″hot-spots″) give clear evidence of thermally-assisted emission mediated by the transient ″hot-electron″ gas during the first few hundred femtoseconds after the onset of the laser pulse, i.e. before thermodynamic equilibration of electron and phonon system. The electron emission then originates from a sequential process in which early-arriving photons deposit their energy in the electron gas partly via plasmon excitation and decay. The electron distribution in the cluster is significantly driven out of its Fermi-Dirac equilibrium as described by the Rethfeld model [Ret02]. Lately-arriving photons interact with this transient non-Fermi-Dirac electron gas thus leading to thermally-assisted multi- (or single-) photon photoemission. Unlike true *n*PPE, the thermally-assisted emission is not governed by a power law because the ″heating step″ is a statistical process involving a variable number of photons as described in section 1.4. In contrast to this result, all pure 2PPE-transitions were characterised by an n=2 power law.

The present work gives various suggestions for further experiments. It has been found out that the electron-phonon coupling is weaker in nanoparticles than in the bulk. In the future one can do two-color pump-probe experiments probing the wide energy window of the initial, intermediate and final states. Such an experiment will shed more light on the mechanism of the reduction of the electron-phonon coupling constant in nanoparticles with decreasing size.

The sum of all experiments made it obvious that the mechanisms of the electron emission from small particles are strongly dependent on their size. It is very promising for future research to manufacture isolated, size-selective nanoparticles and also nanotubes and make a systematic study of their emission properties. In this work, it was not yet possible to produce single crystal nanoparticles. However, this is possible through their epitaxial growth on single crystal substrates, e.g. sapphire. The surface of such nanoparticles should be ideally smooth and free of inhomogenities. The emission pattern from single crystal nanoparticles should not contain ″hot spots″ what will be helpful for a detailed understanding of the nature of the ″hot spots″.

Finally, for further experiments it is proposed to study the interaction in ferromagnetic nanoclusters or in ferromagnetic layers grown on the nanoparticles. This latter experiment is very promising for understanding the magnetic properties of low-dimensional systems and the spin-lattice relaxation mechanism.

Zusammenfassung und Ausblick

In dieser Arbeit wurde die Elektronenemission von Nanopartikeln an Oberflächen untersucht. Speziell wurden metallische Nanocluster untersucht, als selbstorganisierte Ensembles auf Silizium oder Glassubstraten, sowie als Metall-Chalcogenid (MoS_2) Nanoröhren-Prototyp auf Silizium. Der Hauptteil der erfolgten Untersuchungen war auf die Wechselwirkung zwischen Laserstrahlung und metallischen Nanopartikeln konzentriert. Da die Energie der elektromagnetischen Strahlung vom Elektronensystem absorbiert wird, war es interessant, einen Femtosekundenlaser zu verwenden. Seine Pulsbreite ist mit der Elektron-Elektron-Wechselwirkungszeit vergleichbar und deutlich kleiner als die Elektron-Phonon-Wechselwirkungsdauer. Die Energie der Lichtquanten war kleiner als die Austrittsarbeit der untersuchten Proben, so dass Ein-Photonen-Photoemission ausgeschlossen werden konnte. Aus der Literatur ist bekannt, dass in diesem Anregungsbereich Multiphotonen-Anregungen für die Photoemission von Metallen verantwortlich sind. Unsere Untersuchungen zeigten, dass ausgehend von einem kontinuierlichen Metallfilm bis hin zu Clusterfilmen ein anderer Emissionsmechanismus konkurrierend zur Multiphotonen-Photoemission auftritt und für kleine Cluster zu dominieren beginnt.

Die Natur dieses neuen Mechanismus` wurde durch verschiedenartige Experimente untersucht. Ein Vorschlag basiert auf dem Beitrag des „heißen Elektronengases“ zur Elektronenemission. Viele wichtige Charakteristika, wie die Abhängigkeit der Elektronenemissionsintensität von der Laserleistung, Wellenlänge, Pulsbreite und dem zeitlichen Unterschied zwischen den Pulsen wurden untersucht.

Die Elektronenemissionseigenschaften bei Laseranregung wurden in zusätzlichen Untersuchungen mit einer anderen Anregungsart verglichen, der Passage eines Tunnelstroms durch einen Metall-Clusterfilm nahe der Tunnelschwelle (Perkolationsschwelle). Dies kann für die Erfindung neuer effizienter Nano-Elektronenemitter von Interesse sein. Die erhaltenen Resultate können auch zur Erzeugung metallischer Schichten mit abstimmbarer Emissionseigenschaft verwendet werden.

Die essentiellen experimentellen sowie theoretischen Resultate können wie folgt zusammengefasst werden:

1. Die *elektrischen und Emissionseigenschaften von stromtragenden Silberclusterfilmen*, welche in einer schmalen Lücke (5-25 µm Breite) zwischen Silberkontakten auf einem Isolator hergestellt wurden, wurden zum ersten Mal mit einem Emissions-Elektronenmikroskop (EEM) untersucht. Die Leitungsstrom-Spannungskurve ist zuerst linear, steigt dann aber stärker als linear oberhalb einer bestimmten Spannungsschwelle. Die Elektronenemission beginnt im nicht-Omschen Bereich der Leitungsstrom-Spannungskurve des Clusterfilms. Die Potentialverteilung entlang des Metallfilms wurde durch Bildverzerrung im Emissionsmikroskop bestimmt. Der Spannungsabfall ist höher in der Region der Kontakte als im zentralen Bereich des Clusterfilms. Die Elektronenemission ist sehr lokal und stammt von ausgezeichneten Emissionszentren. Sie werden bei bestimmten individuellen Schwellenspannungen erzeugt, in der Region der höchsten elektrischen Feldstärke innerhalb des Clusterfilms. Die scheinbare Größe des Emissionszentrums war anfänglich ungefähr 0.8 µm und wuchs auf einige µm nach weiterer Steigerung der Spannung. Wir untersuchten das Verhalten eines einzigen Emissionszentrums im EEM. Es zeigte sich, dass die Emissionszentren in einem stromleitenden Silberclusterfilm Punktquellen für Elektronen sind, welche relativ hohe Emissions-Stromdichten (mehr als

10^2 A/cm^2) tragen können. Die Energieverteilung der Elektronen von einem einzelnen Emissionszentrum wurde auf etwa 0.5-0.6 eV abgeschätzt. Als Emissionsmechanismus wird die thermionische Emission von dem „steady-state“ heißen Elektronengas in stromdurchflossenen metallischen Partikeln vorgeschlagen. Die Energie wird dabei dem emittierenden Nanopartikel über einen Tunnelstrom zugeführt, welcher von einem Spannungsabfall zwischen benachbarten Teilchen herrührt.

2. *Integrale und ortsaufgelöste Studien der Elektronenemission unter Bestrahlung mit Femtosekunden-Laserstrahlung* wurden für Ag und Au-Nanopartikelfilme untersucht, welche auf Glas- und Siliziumsubstraten aufgewachsen wurden. Es wurde gezeigt, dass der Elektronenemissionsstrom von der Massendicke des Ag-Films auf nicht-monotone Weise abhängt. Der Übergang von einem kontinuierlichen zu einem Nanopartikelfilm ist begleitet von einer Zunahme des Emissions-Stroms von mehr als eine Größenordnung. Man kann somit Bereiche von Massendicken bestimmen, in welchen eine Abnahme an deponiertem Material zu einer Zunahme der Elektronenemission führt. Die Photoemissions-Intensität wächst mit abnehmender zeitlicher Breite des Laserpulses (bei fest eingestellter Leistung), aber diese Abhängigkeit wird weniger steil mit sinkender Partikelgröße. Pump-probe-Experimente zeigten, dass mit abnehmender Teilchengröße die Elektronenemission langsamer sinkt, wenn der zeitliche Unterschied zwischen Pump- und Probe-Puls wächst.

Die experimentellen Resultate wurden durch verschiedene Elektronenemissions-Mechanismen erklärt, z.B. Multiphotonen-Photoemission (*n*PPE), thermionische Emission und thermisch unterstützte *n*PPE sowie optische Feldemission durch die hohe elektrische Feldstärke im Laserstrahl. Der erste Mechanismus überwiegt für kontinuierliche Filme und Partikel mit Größen oberhalb von mehreren zehn Nanometern, der zweite und dritte für Filme von Nanopartikeln von einer Größe von wenigen Nanometern. Um verschiedene Emissionspfade anzuregen muss der Laserpuls sehr kurz sein (unter 100 fs) sowie genügend intensiv (Durchschnittsleistung > 700mW in einem Fokus von 100 μm^2). Die mikrospektroskopischen Messungen bestätigten den 2PPE-Emissionsmechanismus von dünnen Silberfilmen bei „blauer“ Laseranregung ($h\nu$=375-425nm). Das Einsetzen des Ferminiveaus ist relativ scharf (weniger als 150 meV breit) und verschiebt sich um $2h\nu$, wenn die Quantenenergie erhöht wird, wogegen es bei „roter“ Laseranregung ($h\nu$=750-850nm) deutlich verbreitert ist. Dies ist ein klarer Hinweis auf einen thermisch basierten Elektronenemissions-Beitrag zum gesamten Emissionsstrom. Es zeigte sich, dass mit zunehmender Laserleistung die Ausbeute von niederenergetischen Elektronen schwächer zunimmt als die Ausbeute von höherenergetischen Elektronen nahe der Fermikante in einem Spektrum. Das ist ein klarer Hinweis auf eine Koexistenz verschiedener Emissionsmechanismen in einen Spektrum. Diese Messung erklärt ferner das verwirrende Resultat von nicht-ganzzahligen Potenzgesetzen in der Leistungsabhängigkeit, gemessen von anderen Autoren [Fec02, Sch00]. Der optische Feldemissionsmechanismus wird an einem Metallcluster-Film bei hohen Laserleistungen (>300 mW) und großen Wellenlängen sichtbar (750-850 nm).

3. Um die *Größenabhängigkeit des Emissionsverhaltens* theoretisch zu verstehen, wurde ein statistischer Zugang zur Lichtabsorption kleiner Metallpartikel abgeleitet und diskutiert. Er sollte verwendet werden, wenn die durchschnittliche Zahl der von einem Partikel absorbierten Photonen pro Puls in der Größenordung von einigen Zehntel bis einigen Zehn liegt. Wir führten Rechnungen zur absorbierten Energieverteilung über ein Ensemble von Metallpartikeln durch und zogen Folgerungen für die kritische Teilchengröße, ab welcher der Emissionsmechanismus von *n*PPE zu thermionischer und/oder thermisch-unterstützter *n*PPE wechselt. Nach unseren Abschätzungen liegt der Übergangspunkt zwischen

$2r$=2-4 nm, abhängig vom Absorptionskoeffizienten und seiner spektralen Abhängigkeit. Dieses Resultat stimmt sehr gut mit den experimentellen Beobachtungen überein.

4. Größenselektierte, einzelne auf Si-Substraten deponierte *MoS_2-Nanoröhren* wurden mit einer Flugzeit-basierten Zweiphotonen-Photoemissions-Spektromikroskopie untersucht. Die Nanoröhren-Spektren wiesen bei fs-Laser Anregung eine erstaunlich hohe Emissionsintensität auf, deutlich höher als die SiO_x-Substratoberfläche. Dagegen waren sie unsichtbar bei VUV-Anregung bei $h\nu$=21.2 eV. Eine ab-initio-Rechnung für eine MoS_2-Platte (Slab) erklärt die hohe Intensität durch eine hohe Dichte freier intermediärer Zustände beim Zweiphotonen-Übergang bei $h\nu$=3.1 eV. Die oberste Region der berechneten freien DOS stimmt zufriedenstellend mit den gemessenen spektralen Eigenschaften überein. Insbesondere zeigt sich bei Faltung des Grundzustands mit dem Zwischenzustand und Endzustand eine gute Überinstimmung mit dem Experiment.

Während die Nanoröhren-Spektren und die Volumen-Metallspektren perfekt durch reine Zweiphotonen-Photoemission verstanden werden können, zeigen die Spektren von Metall-Nanopartikeln und rauhen Oberflächen (mit „hot spots“) klare Evidenz für thermisch-unterstützte Emission. Diese wird durch das transiente Gas „heißer Elektronen“ nach den ersten hundert Femtosekunden nach der Laseranregung vermittelt, d.h., vor der Equilibrierung des Elektronen- und des Phononensystems. Die Elektronenemission stammt dann von einem sequenziellen Prozess, in welchem früh ankommende Photonen ihre Energie im Elektronengas deponieren, welches sich anfänglich weit weg vom Fermi-Dirac-Gleichgewicht befindet (wie beschrieben im „Rethfeld-Modell“ [Ret02]). Spät ankommende Photonen wechselwirken mit diesem transienten „Nicht-Fermi-Dirac-Elektronengas“ und führen so zur thermisch-unterstützten Multi- oder Einphotonen-Photoemission. Anders als nPPE ist thermisch-unterstützte Emission nicht durch ein ganzzahliges Potenzgesetz dominiert, weil der „Heizschritt“ ein statistischer Schritt ist, welcher unterschiedliche Photonenzahlen involvieren kann (wie in Abschnitt 1.4. beschrieben). Im Gegensatz dazu wurde für reine 2PPE-Übergänge immer ein Potenzgesetz mit n=2 gefunden.

Die verliegende Arbeit wirft mehrere Fragen und Vorschlage für weiterführende Experimente auf. Es wurde herausgefunden, dass die Elektron-Phononkopplung in Nanopartikeln schwächer als im Volumenmaterial ist. Man kann ein 2-Farben Pump-Probe Experiment machen, bei dem man das große Energiefenster von Grund-, Intermediär- und Endzuständen abdeckt. Dieses Experiment wird den Reduktionsmechanismus der Elektron-Phononrelaxation in Nanopartikeln mit abnehmender Größe erhellen.

Die Summe der gezeigten Experimente macht es offensichtlich, daß der Elektronenemissionsmechanismus stark von der Partikelgröße abhängt. Für zukünftige Forschung ist es vielversprechend, isolierte, größenselektierte Nanopartikel und auch Nanoröhrchen zu präparieren und eine systematische Untersuchung ihrer Emissionseigenschaften durchzuführen. In dieser Arbeit war es bis jetzt noch nicht möglich, einkristalline Nanopartikel durch epitaktisches Wachstum auf einem Einkristallsubstrat (z.B. Saphir) zu produzieren. Die Oberfläche solcher Nanopartikel sollte ideal glatt und frei von Inhomogenitäten sein. Die Emissionsbilder von einkristallinen Nanopartikeln sollten dann keine „hot spots“ enthalten. Dies wäre hilfreich, um die Natur der „hot spots“ näher zu verstehen.

Für weitere Experimente wird ferner eine Untersuchung der Wechselwirkung in ferromagnetischen Nanoclustern oder von ferromagnetischen Schichten, die auf Nanopartikeln gewachsen sind vorgeschlagen. Dies Experiment ist sehr vielversprechend, um die magnetischen Eigenschaften und den Spin-Gitter-Relaxationsmechanismus von niederdimensionalen Systemen zu verstehen.

List of used abbreviations

AFM	Atomic Force Microscopy
BBO	Beta Barium Borate
BS	Beam Splitter
CCD	Charge-coupled Device
DOS	Density of States
EDX	Energy-dispersive X-ray Spectroscopy
EEM	Emission- Elektronenmikroskopie
FLAPW	Full Potential Linear Augmented Plane Wave
FWHM	Full Width at Half Maximum
HRTEM	High-resolution Transmission Electron Microscopy
IEF	Imaging Energy Filter
LEED	Low-energy Electron Diffraction
LSP	Localized Surface Plasmon
MCP	Multichannelplate
*n*PPE	*n*-Photon Photoemission
NT	Nanotube
PEEM	Photoemission Electron Microscopy
PES	Photoemission spectroscopy
SEM	Scanning Electron Microscopy
TEM	Transmission Electron Microscopy
TOF	Time-of-Flight
UHV	Ultra High Vacuum
UPS	Ultraviolet Photoemission Spectroscopy
UV	Ultra-Violet (light)
VUV	Vacuum Ultra-Violet (light)

Bibliography

[Aes95] M. Aeschlimann, S. Pawlik and M. Bauer, Ber. Bunsenges. Phys. Chem. **99** (1995) 1504.
[Agr80] B.B. Agrant, A.A. Benditskii and G.M. Gandelman, Sov. Phys. JETP **52** (1980) 27.
[Agu98] M. Aguilar, A.I. Oliva and P. Quintana, Surf. Sci. **409** (1998) 501.
[Ale87] B.V. Alekseenko, R.D. Fedorovich and P.M. Tomchuk, Material Sci. **13** (1987) 161.
[Ale88] B.V. Alekseenko, P.M. Tomchuk and R.D. Fedorovich, Poverhnost Fiz. Khim. Mekh. **10** (1988) 42.
[All87] P. Allen, Phys. Rev. Lett. **59** (1987) 1460.
[And84] L.I. Andreeva, A.A. Benditskii, L.V. Viduta, A.B. Granovskii, Yu.A. Kulyupin, M.A. Makedontsev, G.I. Rukman, B.M. Stepanov, R.D. Fedorovich, M.A. Shoitov and A.I. Yuzhin, Sov. Phys. Solid State **26** (1984) 923.
[Ani70] S.I. Anisimov, Y.A. Imas, G.S. Romanov and Y.V. Chodyko, *The Effect of High Power Radiation on Metals*, Nauka, Moscow (1970).
[Ani77] S.I Anisimov, V.A Benderskii and D. Farkash, Sov. Phys. Usp. **20** (1977) 467.
[Arb03] A. Arbouet, C. Voisin, D. Christofilos, P. Langot, N. Del Fatti, F. Valle, J. Lermé, G. Celep, E. Cottancin, M. Gaudry, M. Pellarin, M. Broyer, M. Maillard, M. P. Pileni and M. Treguer, Phys. Rev. Lett. **90** (2003) 177401.
[Ash00] Neil W. Ashcroft and N.D. Mermin, *Solid State Physics*, ITPS Thomson Learning (2000).
[Bau02] M. Bauer and M. Aeschlimann, J. Electron Spectrosc. Relat. Phenom. 124 (2002) 225.
[Bau72] E. Bauer and H. Poppa, Thin Solid Films **12** (1972) 167.
[Bec73] J.H. Bechtel, Ph.D. thesis, University of Michigan (1973).
[Bej97] D. Bejan and G. Raseev, Phys. Rev. B **55** (1997) 4250.
[Bel90] E.D. Belotskii and P.M. Tomchuk, Surf. Sci. **239** (1990) 143.
[Bel92] E.D. Belotskii, S.P. Luk'yanets and P.M. Tomchuk, Sov. Phys. JETP **74** (1992) 88.
[Ben86] A.A. Benditskii, L.V. Viduta, Yu.A. Kulyupin, A.P. Ostranitsa, P.M. Tomchuk, R.D. Fedorovich and V.A. Yakovlev, Bull. Acad. Sci. USSR, Phys. Ser. **50** (1986) 170.
[Ben88] A.A. Benditskii, L.V. Viduta, B.I. Konov, S.M. Pimenov, A.M. Prokhorov, P.M. Tomchuk, R.D. Fedorovich, N.I. Chapliev and V.A. Yakovlev, Poverkhnost. Fiz. Khim. Mekh. **10** (1988) 48.
[Ble81] R. Blessing, H. Pagnia and N. Sotnik Thin Solid Films, **85** (1981) 119.
[Boe54] H. Boersch, Z. Phys. **139** (1954) 115.
[Boh83] C.F. Bohren and D.R. Huffman, *Absorption and Scattering of Light by Small Particles*, Wiley Science Paperback Series (1983).
[Bol02] M.V. Bollinger, J.V. Lauritsen, K.W. Jacobsen, J.K. Norskov, S. Helveg and F. Besenbacher, Phys. Rev. Lett. **87** (2002) 196803.
[Bor65] P.G. Borzjak, O.G. Sarbei and R.D. Fedorowitsch, Phys. Stat. Solidi **8** (1965) 55.
[Bor76] P. Borziak, V. Dyukov, A. Kostenko and S. Nepijko, Thin Solid Films **36** (1976) 21.
[Bun65] F.V. Bunkin and M. Fedorov, Sov. Phys. JETP **21** (1965) 896.
[Cah03] D. Cahen and A. Kahn, Adv. Matter. **15** (2003) 271.
[Car78] M. Cardona and L. Ley, *Photoemission in Solids 1*, vol. 26 of *Topics in Applied*

Physics, Springer-Verlag Berlin (1978).
[Cai01] W. Cai, H. Hofmeister and M. Dubiel, Eur. Phys. J. D **13 (**2001) 245.
[Che86] Q.Y. Chen and C.W.J. Bates, Phys. Rev. Lett. **57** (1986) 2737.
[Cin04] M. Cinchetti, D.A. Valdaitsev, A. Gloskovskii, A. Oelsner, S.A. Nepijko and G. Schönhense, J. Electron Spectrosc. Relat. Phenom. **137-140** (2004) 249.
[Cin05] M. Cinchetti, A. Gloskovskii, S. A. Nepjiko, G. Schönhense, H. Rochholz and M. Kreiter, Phys. Rev. Lett. **95** (2005) 047601.
[Coc85] F. Cocchini and F. Bassani, Surf. Sci. **156 (**1985) 851.
[Coe87] R. Coehoorn, C. Haas, J. Dijkstra, C.J.F. Flipse, R.A. de Groot and A. Wold, Phys. Rev. B **35** (1987) 6195.
[Dit72] G. Dittmer, Thin Solid Films **9** (1972) 317.
[Dre05] M.Drescher and F. Krausz, J. Phys. B: At. Mol. Opt. Phys. **38** (2005) L727.
[Dub32] L.A. DuBridge, Phys. Rev. **43** (1932) 727.
[Dwe73] A.W. Dweydari and C.H.B. Mee, Phys. Stat. Sol. A **17** (1973) 247.
[Dwe75] A.W. Dweydari and C.H.B. Mee, Phys. Stat. Sol A **27** (1975) 223.
[Els87] H.E. Elsayed–Ali, T.B. Norris, M.A. Pessot and G. A. Mourou, Phys. Rev. Lett. **58** (1987) 1212.
[Fan92a] W.S. Fann, R. Storz, H.K. Tom and J. Bokor, Phys. Rev. B, **46** (1992) 13592.
[Fan92b] W.S. Fann, R. Storz, H.K. Tom and J. Bokor, Phys. Rev. Lett. **68** (1992) 2834.
[Fat98] N. Del Fatti, R. Bouffanais, F. Vallée, C. Flytzanis, Phys. Rev. Lett. **81** (1998) 922.
[Fec02] G.H. Fecher, O. Schmidt , Y. Hwu and G. Schönhense, J. Electron Spectrosc. Relat. Phenom. **126** (2002) 77.
[Fed00] R.D. Fedorovich, A.G. Naumovets and P.M. Tomchuk, Phys. Rep. **328** (2000) 73.
[Fed93] R.D. Fedorovich, A.G. Naumovets and P.M. Tomchuk, Prog. Surf. Sci. **42 (**1993) 189.
[Fom75] V.S. Fomenko and I.A. Podchernyaeva, *Emission and Adsorptive Properties of Substances and Materials*, Atomizdat, Moscow (1975).
[Fow31] R.H. Fowler, Phys. Rev. **38** (1931) 45.
[Fuj84] J.G. Fujimoto, J.M. Liu, E.P. Ippen and N. Bloembergen, Phys. Rev. Lett. **53** (1984) 1837.
[Gan12] R. Gans, Ann. Physik **37** (1912) 881.
[Gin55] V.L. Ginzburg and V.P. Shabanskii, Dokl. Akad. Nauk SSSR **100** (1955) 445.
[Got96] W. Gotschy, K. Vonmetz, A. Leitner, F. R. Aussenegg, Appl. Phys. B **63** (1996) 381.
[Gro95] R.H.M. Groeneveld, R. Sprik, A. Lagendijk, Phys. Rev. B **51** (1995) 11433.
[Had98] L. Haderbache, R. Garrigos, R. Kofman, E. Sondergard, P. Cheyssac, Surf. Sci. **411** (1998) L748.
[Hee93] W.A. de Heer Rev. Mod. Phys. **65** (1993) 611.
[Heu78] F.M. d'Heurle, P.S. Ho, in: J.M. Poate, K.N. Tu, J.W. Mayer (Eds.) *Thin Films Interdiffusion and Reactions*, Wiley, New York, (1978) 243.
[Hip83] R. Hippler, H.-J. Humpert, H. Schwier, S. Jetzke and H.O. Lutz, J. Phys. B: At. Mol. Opt. Phys. **16** (1983) L713.
[Hod00] J.H. Hodak, A. Henglein and G.V. Hartland, J. Chem. Phys. **112** (2000) 5942.
[Hub05] F. Hubenthal, M. Alschinger, M. Bauer, D. Blazquez Sanchez, N. Borg, M. Brezeanu, R. Frese, C. Hendrich, B. Krohn, M. Aeschliman and F. Trager, Proceedings of the SPIE, **5838** (2005) 224.
[Iva04] V.V. Ivanovskaya and G. Seifert, Solid State Commun. **130** (2004) 175.
[Kag57] M.I. Kaganov, I.M. Lifshitz, L.V. Tanatarov, Sov. Phys. JETP **4** (1957) 173.

[Kat61] G.A. Katrich and O.G. Sarbei, Sov. Phys. Solid State **3** (1961) 1181.
[Kat87] G.A. Katrich and A.G. Naumovetz, in: J. Koukal (Ed.) *Physics of Solid Surface*, Elsevier, Amsterdam-Oxford-New-York-Tokio (1987).
[Kel64] L.V. Keldysh, Sov. Phys. JETP **20** (1964) 1307.
[Kin23] K.H. Kingdon and I. Langmuir, Phys. Rev. **21** (1923) 380.
[Kit05] Ch. Kittel, *Introduction to solid state physics,* Wiley, New York (2005)
[Kno98] E. Knoesel, A. Hotzel and M. Wolf, Phys. Rev. B **57** (1998) 12812.
[Kra75] M.L. Krasnov, *Integral equations*, Nauka, Moscow (1975).
[Kre85] U. Kreibig and L. Genzel, Surf. Sci. **156** (1985) 678.
[Kre93] U. Kreibig and M. Vollmer, *Optical Properties of Metal Clusters*, Springer Series in Materials Science (1993).
[Lan62] L.D. Landau and E. M. Lifschitz, *The Classical Theory of Fields*, Pergamon Press, Oxford (1962)
[Lan68] L.D. Landau, E.M. Lifshitz, *Statistical physics*, Pergamon Press, Oxford (1968).
[Lan71] N.D. Lang, Phys. Rev. B **4** (1971) 4234.
[Lan77] L.D. Landau and E.M. Lifshitz, *Quantum Mechanics*, Pergamon Press, Oxford (1977).
[Leh00] J. Lehmann, M. Merschdorf, W. Pfeiffer, A. Thon, S. Voll and G. Gerber, Phys. Rev. Lett. **85** (2000) 2921.
[Lie93] A.Liebsch, Phys. Rev. B **48** (1993) 11317.
[Log67] E.M. Logothetis and P.L. Hartman, Phys. Rev. Lett. **18** (1967) 581.
[Lug94] A.V. Lugovskoy, T. Usmanov and A. V Zinoviev, J. Phys. D: Appl. Phys. **27** (1994) 623.
[Lug98] A.V. Lugovskoy, T. Usmanov and A.V Zinoviev, J. Opt. Soc. Am. B **15** (1998) 53.
[Lug99] A.V Lugovskoy and I. Bray, Phys. Rev. B **60** (1999) 3279.
[Luk36] V.S. Lukoshkov, J. Tekhn. Fiz. **6** (1936) 26.
[Mes81] B.J. Messinger, K.U. von Raben, R.K. Chang and P.W. Barber, Phys. Rev. B **24** (1981) 649.
[Mih03] D. Mihailovic, Z. Jaglicic, D. Arcon, A. Mrzel, A. Zorko, M. Remskar, V.V. Kabanov, R. Dominko, M. Gaberscek, C.J. Gomez-Garcia, J.M. Martínez-Agudo and E. Coronado, Phys. Rev. Lett. **90** (2003) 146401.
[Mül56] E.W. Müller, in: W.G. Berl (Ed.) *Physical Methods in Chemical Analysis*, Academic Press, New York (1956) 135.
[Nei58] J.R. Neighbours and G.A. Alers, Phys. Rev. **111** (1958) 707.
[Nep02] S.A. Nepijko, N.N. Sedov, G. Schönhense and M. Escher, J. Microsc. **206** (2002) 132.
[Nep03] S.A. Nepijko, A. Gloskovskii, N.N. Sedov and G. Schönhense, J. Microsc. **211** (2003) 89.
[Nep05] S.A. Nepijko, N.N. Sedov and G. Schönhense, in P. Hawkes (Ed.) *Advances in imaging and electron physics,* **136** (2005) 227.
[Nol04] E.L. Nolle and M. Ya. Schelev, Tech. Phys. Lett. **30** (2004) 304.
[Pal91] E.P. Palik (Ed.) *Handbook of Optical Constant of Solids*, Academic Press, New York (1991).
[Paw98] S. Pawlik, R. Burgermeister, M. Bauer and M. Aeschlimann, Surf. Sci. **402–404** (1998) 556.
[Pet97] H. Petek and S. Ogawa, Prog. Surf. Sci. **56** (1997) 239.
[Pfe04] W. Pfeiffer, C. Kennerknecht and M. Merschdorf, Appl. Phys. A **78** (2004) 1011.
[Rem03] M. Remskar, A. Mrzel, R. Sanjines, H. Cohen and F. Levy, Adv. Mater. **15** (2003)

237.
[Ret02] B. Rethfeld, A. Kaiser, M. Vicanek and G. Simon, Phys. Rev. B **65** (2000) 214303.
[Sab90] F. Sabary and J. C. Dudek, Vacuum **41** (1990) 476.
[Sch00] O. Schmidt, Ph.D. thesis, Johannes Gutenberg-Universität Mainz (2000).
[Sch01] M. Scharte, R. Porath, T. Ohms, M. Aeschlimann, J.R. Krenn, H. Ditlbacher, F.R. Aussenegg and A. Liebsch, Appl. Phys. B **73** (2001) 305.
[Sch02a] C.M. Schneider and G. Schönhense, Rep. Prog. Phys. **65** (2002) R1785.
[Sch02b] L. Scheffer, R. Rosentzveig, A. Margolin, R. Popovitz-Biro, G. Seifert, S. R. Cohen and R. Tenne, Phys. Chem. Chem. Phys. **4** (2002) 2095.
[Sch02c] O. Schmidt, M. Bauer, C. Wiemann, R. Porath, M. Scharte, O. Andreyev, G. Schoenhense and M. Aeschlimann, Appl. Phys. B **74** (2002) 223.
[Sei00] G. Seifert, H. Terrones, M. Terrones, G. Jungnickel and T. Frauenheim, Phys. Rev. Lett. **85** (2000) 146.
[Sha85] T.K. Sham , Phys. Rev. B **31** (1985) 1888.
[Sha96] V.M. Shalaev, C. Douketis, T. Haslett, T. Stuckless and M. Moskovits, Phys. Rev. B **53** (1996) 11193.
[Sha00] V. M. Shalaev, *Nonlinear Optics of Random Media*, vol. 158 of *Springer Tracts in Modern Physics*, Springer-Verlag, New York (2000).
[Sil70] A.P. Silin, Sov. Phys. Solid State **12** (1970) 3553.
[Stu89] J.T. Stuckless and M. Moskovits, Phys. Rev. B, **40**, (1989) 9997.
[Sze64] S. M. Sze, J. L. Moll and T. Sugano, Solid-State Electron. **7** (1964) 509.
[Ten92] R. Tenne, L. Margulis, M. Genut and G. Hodes, Nature **360** (1992) 444.
[Tom66] P.M. Tomchuk and R.D. Fedorovich, Sov. Phys. Solid State **8** (1966) 226.
[Tom97] P.M. Tomchuk and B.P. Tomchuk, Sov. Phys. JETP **85** (1997) 360.
[Woo81] D.M. Wood. Phys. Rev. Lett. **46** (1981) 749.
[Yas92] H. Yasunaga and A. Natori, Surf. Sci. Rep. **15** (1992) 205.
[Zim04] A. Zimina, S. Eisebitt, M. Freiwald, S. Cramm, W. Eberhardt, A. Mrzel and D. Mihailovic, Nano Lett. **4** (2004) 1749.